Electronics at Optical Frequencies

Dissertation
zur Erlangung des Doktorgrades
an der Fakultät für Mathematik, Informatik und Naturwissenschaften
Fachbereich Physik
der Universität Hamburg

vorgelegt von

Felix Ritzkowsky

Hamburg

2023

Gutachter der Dissertation:	Prof. Dr. Franz X. Kärtner Prof. Dr. Jochen Küpper
Zusammensetzung der Prüfungskommission:	Prof. Dr. Franz X. Kärtner Prof. Dr. Jochen Küpper PhD Phillip D. Keathley Prof. Dr. Francesca Calegari Prof. Dr. Daniela Pfannkuche
Vorsitzende/r der Prüfungskommission:	Prof. Dr. Daniela Pfannkuche
Datum der Disputation:	28.07.2023
Vorsitzender Fach-Promotionsausschusses PHYSIK:	Prof. Dr. Günter H. W. Sigl
Leiter des Fachbereichs PHYSIK:	Prof. Dr. Wolfgang Parak
Dekan der Fakultät MIN:	Prof. Dr.-Ing. Norbert Ritter

Abstract

With the advent of ultrafast optics and controllable waveforms consisting of only a few oscillations of the electric field, the idea of controlling electrons at the frequency of light was born [1–4]. This established the potential of using a controlled optical waveform to switch electronic circuit elements at the frequency of an optical wave, typically on the order of 0.1 to 1 petahertz (10^{15} Hz). This exceeds the frequency of the fastest electronic devices by two to three orders of magnitude [5] and the clock rates of modern computers by up to six orders of magnitude. To this end, many pioneering experiments have shown that optical waveforms can be used to drive attosecond electron currents at metal-vacuum interfaces [6–11], in dielectric large bandgap materials [12–15] or in air [16–19]. This thesis shows how integrated metallic nanoantennas are utilized to enhance the electric field of optical few-cycle pulses in nanometer-sized hotspots, generating sub-cycle field emission with only picojoule-level pulse energies. Exploiting the attosecond-fast currents on the nanoscale, petahertz bandwidth field sampling with 5 femtojoule sensitivity is experimentally demonstrated [20]. The influence of antenna symmetry and device design on the sampling frequency response is investigated theoretically to guide application specific design strategies [21]. To further test the integrated nanoantenna platform, we have developed a passively CEP-stable sub-2-cycle laser source that produces 16 fs duration pulses at a central wavelength of 2.7 µm with $>$ 84 nJ energy at a repetition rate of 50 kHz. The system is based on adiabatic difference generation [22], and significantly simplifies previous implementations by relying solely on material-based compression. Furthermore, the CEP stability of adiabatic difference generation is measured for the first time and shows excellent passive stability of 190 mrad rms. We show that by using the newly developed mid-infrared sub-2-cycle source, the CEP dependent yield of a single nanoantenna is significantly improved by a factor of 30 from a previous 0.1 electrons per laser shot to $>$ 3 electrons [10, 23]. Thanks to this significant improvement, and by illuminating up to 1000 antennas, we produce fully carrier-envelope phase (CEP) dependent currents of up to 3000 electrons per shot, improving previous results by three orders of magnitude [23]. The results of this work will open many interesting avenues for the exploration of optical frequency electronics based on integrated nanoantennas, such as ultra-broadband time spectroscopy in the infrared continuously covering the terahertz to visible spectrum, or petahertz bandwidth logic circuits [24, 25].

Zusammenfassung

Mit den Fortschritten der Ultrakurzzeitoptik und der Erzeugung von passiven phasenstarren optischen Wellenformen, die nur aus wenigen Schwingungen des elektromagnetischen Feldes bestehen, entstand die Idee, Elektronen auf der Frequenzskala des Lichts zu steuern [1–4]. Damit wurde das Potenzial erkannt, eine kontrollierte optische Wellenform zum Schalten elektronischer Schaltelemente mit der Frequenz einer optischen Welle zu verwenden, die typischerweise in der Größenordnung von 0.1 bis 1 Petahertz (10^{15} Hz) liegt. Dies übertrifft die Frequenz der schnellsten elektronischen Bauteile um zwei bis drei Größenordnungen [5] und die Taktraten moderner Computer um bis zu sechs Größenordnungen. Viele bahnbrechende Experimente haben gezeigt, dass optische Wellenformen genutzt werden können, um Attosekunden schnelle Elektronenströme an Metall-Vakuum-Grenzflächen zu erzeugen [6–11], oder in dielektrischen Materialien mit großer Bandlücke [12–15] oder in Luft [16–19]. In dieser Arbeit wird gezeigt, wie durch Ausnutzung der Plasmonischen Feldüberhöhung in integrierte metallische Nanoantennen ultrakurze optische Pulse im Picojoule-Bereich attosekundenschnelle Feldemission erzeugen kann. Unter Ausnutzung der Attosekunden-Ströme auf der Nanoskala wird eine Zeitdomänen Feldabtastung mit Petahertz-Bandbreite und einer Empfindlichkeit von 5 Femtojoule experimentell demonstriert [20]. Der Einfluss der Antennensymmetrie und des Bauelementdesigns auf den Frequenzgang der Abtastung wird theoretisch untersucht, um anwendungsspezifische Designstrategien zu entwickeln [21]. Um die integrierte Nanoantennenplattform weiter zu testen, haben wir eine passiv Träger-Einhüllenden Phasen (CEP) stabile Sub-2-Zyklus-Laserquelle entwickelt, die Pulse mit einer Dauer von 16 fs bei einer zentralen Wellenlänge von 2.7 µm mit $>$ 84 nJ Energie bei einer Repetitionsrate von 50 kHz erzeugt. Das System basiert auf der adiabatischen Differenzfrequenzerzeugung [22] und vereinfacht bisherige Implementierungen erheblich, da es ausschließlich auf materialbasierter Kompression beruht. Darüber hinaus wird zum ersten Mal die CEP-Stabilität der adiabatischen Differenzfrequenzerzeugung gemessen, die eine hervorragende passive Stabilität von 190 mrad rms aufzeigt. Ich zeige, dass sich die CEP-abhängige Ladungsausbeute einer einzelnen Nanoantenne durch den Einsatz der neu entwickelten Sub-2-Zyklen-Quelle im mittleren Infrarot von bisher 0.1 Elektronen pro Laserschuss auf $>$ 3 Elektronen [10, 23], also um den Faktor 30 verbessern lässt. Durch diese signifikante Verbesserung und die gleichzeitige Beleuchtung von bis zu 1000 Antennen erzeugen wir CEP-abhängige Ströme von bis zu 3000 Elektronen pro Schuss und konnten damit frühere Ergebnisse um drei Größenordnungen verbessern [23]. Die Ergebnisse dieser Arbeit werden viele interessante Wege für die Erforschung von Elektronik mit optischen Frequenzen auf der Basis integrierter Nanoantennen eröffnen, wie unter anderem Logikschaltungen mit Petahertz-Bandbreite [24, 25], oder als Anwendung für ultra-breitbandige Zeitbereichs spektroskopie im Infrarot, die kontinuierlich das Terahertz- bis sichtbare Spektrum abdeckt.

Acknowledgement

My doctorate journey spanned almost exactly 5 years, just three days shy. It was often exhausting, but more than anything, it was a remarkable and enlightening experience. The work showcased in this thesis feels like a culmination not just of these past years but of countless moments, hard work, and cherished personal connections. It's through friendships and collaborations with colleagues that I've learned all I know today. I want to sincerely acknowledge all these wonderful individuals who have been an integral part of my transformation into the person i am today.

First and foremost, I want to extend my deepest gratitude to my supervisor, Franz X. Kärtner. He not only welcomed me into his group but also granted me the freedom to delve deeply into the research presented in this thesis. Franz's enthusiasm and enthusiasm for his work are both infectious and deeply motivating. While we may not have resolved the initial problem we set out to tackle, I remain hopeful that someday I will.

Secondly, I must express my profound gratitude to Phillip "Donnie" Keathley. His invitation to join the QNN group at MIT in 2019 was pivotal on a scientific and also personal level. I believe that without his influence, this thesis would have taken a markedly different direction. Through Donnie, I truly grasped the power of collaboration and realized how continuous dialogue can push ideas forward. Our time together was marked by the pure joy of finding things out. I am looking forward to our future scientific adventures together.

I'd also like to convey my gratitude to my co-supervisor, Jochen Küpper. His support and pragmatic approach were invaluable in guiding the trajectory of my doctorate. Without his influence, I suspect my journey would have extended closer to the six-year mark.

The UFOX group under Franz at CFEL deserves special recognition in my journey. It's a melting pot of wonderful people, each bringing their unique essence to the team. A special nod of appreciation to Huseyin Cankaya for his invaluable assistance with the construction of my treasured MIR laser. My gratitude extends to Giulio M. Rossi, who adeptly introduced me to the Italian approach to OPAs. A shoutout to Roland for the countless cups of coffee and engaging political dialogues. Certainly Engjell Bebeti deserves my gratitude as well, who joined the petahertz electronics team in a critical time and was the perfect complementary addition.

My thanks go out to the entire Synthesizer team: Miguel Silva Toleda, Fabian Scheiba, Maximilian Kubullek, Nicolai Klemke, John Messerschmidt, and Yujiao Jiang. An additional note of appreciation for Hong Ye, whose guidance proved crucial during my inaugural year in the group.

Furthermore, I want to express my gratitude to the AXSIS team, foremost Nicholas Matlis, who also had an important role into giving me a great start into the UFOX group. Additionally i want

to thank Dongfang Zhang, Mikhail Pergament, Timm Rohwer and Tobias Kroh. Many thanks also to our engineering support team, Andrej Berg and Thomas Tilp.

A distinct note of appreciation is reserved for Uta Freydank. Her guidance and expertise in navigating the sometimes intricate DESY administration were invaluable. A sentiment we consistently shared was the belief that if you find yourself still irked by an issue, it signifies that you remain invested and care deeply.

I also want to express my gratitude to the UMP group with Tobias Herr, Thibault Wildi and Thibault Voumard.

From my time at MIT I want to thank Karl Berggren and Dorothy Fleischer for warmly welcoming me to the QNN group. Additionally I want to thank Mina Bionta, John Simonaitis, Navid Abedzadeh, Marco Colangelo, William "Billy" Putnam and Marco Turchetti for such a fun time in- and outside the lab. In particular I want to thank Matthew Yeung for all his support during the last year of my degree.

I also want to thank the whole Sesame Street from Max-Planck which joined me in the recent past on my journey. Foremost Toru Matsuyama-sensei, Thomas Gebert, Matthias Budden and Guido Meier.

Reflecting on my time before DESY, I must convey profound gratitude to Markus Ludwig. The hours we shared in the Konstanz lab were invaluable, and I learned immensely under his guidance. I'm equally indebted to Tobias Rybka for planting the initial seed for my passion for ultrafast optics. Additionally, heartfelt thanks go to Alfred Leitenstorfer and Daniele Brida for providing me with an outstanding education in Konstanz.

Without the support of my friends from Konstanz I would have never been able to walk this path. Thanks to Yannic Behovits, Jana Ochs, Milan Jubitz, Richard Lohse, Felix Förschner, Vivien Enenkel, Sophia Backhaus, Tani Lautenschläger, Svenja Bauer, Josianne Kollmann, Kim Stadler, Daniela Fuchs, Esther Emhart, Katrina Wahl and Oliver Thomaschewski.

I want to thank my friends who i knew since essentially forever, Florian Otte, Josi Wolf, Jan-Henning Steeneck, Sebastian Peise, Bennett Possin, Jonas Kalinka, Sarina Kalinka-Fröhling.

I must extend my deepest gratitude to my parents and my brother. Their unwavering support and boundless love throughout my life paved the way for me to embark on this journey.

Finally I want to my express deepest gratitude and love to my girlfriend Laura who kindly and patiently supported me so well the last years. I love you and I am looking forward towards a wonderful future together.

Contents

Acronyms

ADFG	Adiabatic Difference Frequency Generation
CEP	Carrier-Envelope Phase
CEO	Carrier-Envelope Offset
DFG	Difference-Frequency Generation
FROG	Frequency-Resolved Optical Gating
SHG	Second-Harmonic Generation
SFG	Sum-Frequency Generation
NOPA	Noncollinear Optical-Parametric Amplification
OPA	Optical-Parametric Amplification
SPIDER	Spectral-Phase Interferometry for Direct Electric-Field Reconstruction
THG	Third-Harmonic Generation
2DSI	Two-Dimensional Spectral Shearing Interferometry

1 Introduction

With the advent of ultrafast optics and controllable optical waveforms consisting of only a few oscillations of the electric field, the idea of controlling electrons at the frequency of light was born [1]. With this idea laid out, the potential for using a controlled optical waveform to switch electronic circuit elements at the frequency of an optical wave, which is typically on the order of one petahertz (10^{15} Hz), was recognized [4]. This frequency exceeds that of the fastest semiconductor devices by two to three orders of magnitude [5], and the clock rates of modern computers by up to six orders of magnitude. True optical frequency electronics would not only be able to significantly improve modern electronics but, more importantly, would provide the ability to control the flow of electronic signals at the frequency of light. The impact of realizing this technology would affect every aspect of modern electronics from providing up to three orders of magnitude improvement of clock rates, to augmenting digital and quantum computing with petahertz bandwidth logic circuits. With recent advances in integrated photonic circuits, one could also imagine seamless interconnects between a photonic circuit and its electronic counterpart, enabling new technologies for optical telecommunication.

Of course, such optical frequency electronic devices do not exist yet, and the operating frequency of high frequency electronics has plateaued at hundreds of gigahertz for many reasons [26, 27]. However, in the last decade, it was shown that nanometer-sized metallic antennas integrated into a microscopic electronic circuit for electronic readout, can be driven at optical frequencies generating petahertz bandwidth current pulses and [8, 9]. While these are not yet practical electronic devices, they demonstrate the possibility of rectifying optical fields at unprecedented frequencies.

To put the rectification at optical frequencies into context, it is helpful to look at the early beginnings of electronics. The first documented case of electric rectification was found by a young scientist at the University of Würzburg in 1874, named Karl Ferdinand Braun [28]. What he observed was the unilateral flow of current in a contact between a sharp metal wire and a lead sulfide crystal, defying the Ohms law as he knew it [29]. This effect is today well understood and known as the Schottky effect. Although this was treated as a peculiarity at that time and was not pursued further, it had major significance later in time. The second

observation of rectification paved the way for electronics as we know it. In collaboration with Thomas A. Edison, William Preece investigated light bulbs produced by Edison and found that a current can be measured from the filament of an incandescent lightbulb towards an anode, but not in reverse [30]. This effect is now known as the Edison effect, which is the thermal emission of electrons from the filament of a lightbulb that is accelerated towards the anode but not in reverse. Building on this effect, John A. Fleming published in 1905 a work showing that this devices can be used to rectify weak but high-frequency wireless signals and measure the rectified signals with a slow galvanometer [31]. This device, now called the Fleming valve, was the first practical implementation of a diode and is considered to have laid the foundations for modern electronics and immediately led, through the improvements made by Lee de Forest, to oscillators, amplifiers, and sensitive detectors [32]. Based on this development, the field of vacuum electronics was born and was a cornerstone of analog and digital electronics until it was eventually succeeded half a century later by semiconductors [33, 34]. In addition, the invention of the Braun tube, named after Karl F. Braun, which is based on the Edison effect, allowed the creation of the oscilloscope that allows the detection of high-frequency signals in the time domain and has been a staple in physics and engineering laboratories since the beginning of the last century [35].

The journey to optical frequency electronics started with the invention of the laser in 1960 by Maiman [36], and it was seen that new phenomena can be explored that utilize much higher light intensities that can only be achieved with coherent light of a laser [37]. In the 1960s it was recognized that the cat's whisker diode, also called a crystal detector, a point contact between a metal tip and a semiconductor or another metal, which was essentially discovered by K. F. Braun in 1874 and later perfected by J. C. Bose [38], can be used at much higher frequencies than radio waves and allowed to reunite the frequency domain of lasers with the microwave domain [39]. Similarly to the work of Fleming, the cat's whisker diode rectifies optical frequencies into detectable DC currents, and by heterodyne mixing this allows referencing of optical frequencies against known microwave frequency standards, which was demonstrated for 88 THz [40]. The main problem with these techniques is that it was not possible at that time to create phase-locked frequency chains coherently linking the optical with the microwave domain. Only with sophisticated frequency chains and very stable microwave oscillators was the optical domain coherently locked for the first time in the 1980s [41–43]. The necessary complexity was immediately reduced with the invention of the self-referenced optical frequency comb, which allowed one to directly link the optical domain coherently to the microwave domain [44, 45]. Self-referencing through feedback from $f-2f$ interferometry stabilized the carrier-envelope offset frequency of an optical frequency comb, which enabled the generation of carrier-envelope phase (CEP) stabilized and controlled optical waveforms. By generating CEP stabilized few- to single-cycle optical waveforms, it was possible for the first time to precisely steer electrons on an attosecond time scale and use this control to generate attosecond XUV pulses through

high-harmonic generation [1–3]. With the mechanism established, the field emission of electrons from nanometer-sharp tungsten tips was explored, showing attosecond current generation with few-cycle optical pulses, achievable with pulse energies as low as few nanojoules [6, 7, 11]. These experiments essentially laid the groundwork for demonstrating the rectification at a petahertz bandwidth. Although this research enabled great scientific insight into the emission mechanisms of electrons on the attosecond time scale, the integration of these tips into actual circuit systems is difficult and impossible to scale up in numbers because of the mesoscopic size and the requirement of necessary bulky vacuum equipment.

Electron-beam lithography patterned plasmonic nanoantennas, which are nanometer-sized metallic optical antennas, create strong localization of optical fields in nanometer volumes [46, 47]. These antennas were fully integrated into microcircuits and demonstrated the rectification of optical frequencies producing single-electron currents while using only picojoule-level optical few-cycle pulses [8, 9]. The mechanism behind the rectification is the field emission of electrons at the metal-vacuum boundary. Because of the strong localization of the electric field, the emission point is spatially well-defined, and an anode or another antenna can be placed in close proximity with only a few tens of nanometers of distance. This has many advantages: (i) reduced energy requirements due to the resonant antenna; (ii) the close distances allow the transport of electrons essentially through a vacuum; (iii) the lithographic approach allows flexible antenna design and lends itself to large-scale integration and multiplexing; (iv) electron transport from the antenna to the anode can happen on a sub-cycle timescale with less than one femtosecond [10]. With the nanoantenna platform showing a promising approach for scalable and highly integrated optical frequency electronics, a few key technological milestones need to be demonstrated. The first is a time domain technique that gives insight into petahertz bandwidth dynamics so it becomes possible to observe the intricate dynamics of the electronic processes *in-situ*. The other is the demonstration of true scalability, showing that not only are a few nanoantennas producing single electron currents feasible [23], but that currents of thousands of electrons can be generated with thousands of antennas. With these demonstrated, the field of optical frequency electronics is significantly advanced towards its goal of achieving petahertz bandwidth electronics.

The next significant technological step will be the study of implementing petahertz bandwidth logic circuits [24, 25]. On a more scientific level the study of the dynamics of current generation from the emission itself to the transport in the vacuum gaps significantly benefits from the improved signal levels. Furthermore, having a sensitive attosecond resolution field sampling device has many exciting properties in spectroscopy, as it allows one to measure amplitude and phase information simultaneously [48]. The ability to use a single device for time-domain sampling that covers the entire electromagnetic spectrum from petahertz to gigahertz is particularly attractive. This capability is of particular interest for the study of highly non-linear phenomena in solids, as it can measure the full nonlinear electromagnetic field response in time [49, 50].

Another interesting technical application is to exploit the strong carrier-envelope phase (CEP) sensitivity of these devices to make fully integrated CEP detectors that enable single-shot read-out while only using tens of nanojoules of pulse energy [18, 51].

This thesis elaborates on how it is possible to use attosecond-fast electron emission in plasmonic nanoantennas to measure femtojoule-level optical waveforms with a petahertz bandwidth [20]. The demonstrated sensitivity is approximately six orders of magnitude better than comparable techniques [13, 52]. In addition, the frequency response of the nanoantenna-based sampling device is theoretically studied with regards to how the symmetry properties of the devices influence and reshape the petahertz sampling bandwidth [21]. For further investigation of the nanoantenna devices, a custom laser source was developed with the goal of improving the electron emission yield of individual nanoantennas while also providing enough energy to use up to a thousand nanoantennas simultaneously. The developed laser source is based on adiabatic difference frequency generation and delivers 16 fs duration pulses with a center frequency of $\sim$111 THz ($\lambda = 2.7\,\mu$m), that are passively carrier-envelope phase stable. The system is able to deliver > 4 mW of average power at a repetition rate of 50 kHz corresponding to > 84 nJ of energy. Furthermore, the implemented pulse compression scheme is based solely on material-based dispersion management, which increases the robustness of the system and significantly reduces the complexity of the setup compared to previous implementations [53]. For the first time, the CEP stability of adiabatic difference frequency conversion was characterized by a remarkable stability of < 190 mrad rms. Using the custom laser source single-shot measurement of CEP changes using hundreds of nanoantennas simultaneously is demonstrated. Up to 3000 e per individual shot were measured, improving the state of the art by three orders of magnitude [23]. Furthermore, the scaling of the charge yield per shot as a function of the peak electric field is investigated, showing scaling from tunnel emission into the nonadiabatic tunneling regime. The results demonstrated in this thesis enable many interesting experiments in the field of optical frequency electronics, including sensitive attosecond resolution field sampling devices or integrated low-energy CEP detectors.

This thesis is structured into six chapters. Chapter 2 introduces ultrafast few-cycle pulses and their physical and mathematical treatment, while also discussing nonlinear optics and the important mechanisms relevant to this thesis. In addition, a brief introduction to photoinduced electron emission is provided. Chapter 3 presents the published work on optical field sampling with attosecond resolution [20]. Chapter 4 discusses the theoretical role of device symmetry in the accessible frequency response presented at the conference Ultrafast Phenomena [21]. Chapter 5 presents the published work on the laser source development [54], and gives further additional technical details on the system, including alignment strategies. In addition, a detailed section on the developed mid-infrared spectral phase characterization techniques is also included. Chapter 6 presents the work on single-shot CEP change detection and the demonstration of large-scale

integration of optical frequency electronic devices (currently under submission). Chapter 7 summarizes the work presented in this thesis and places the achieved results in a larger scientific context. The outlook will present a roadmap for future necessary developments for optical frequency electronics.

2 Fundamentals

2.1 Ultrafast Optics

Ultrafast optics is a rich topic of modern physics and has enabled many insights into physics, such as tracking the movement of electrons at their natural timescale, understanding photoinduced changes in states of matter, and chemical reactions, which usually occur on a timescale below one picosecond down to 1 femtosecond [3, 55]. More generally speaking, ultrafast optics uses the fact that one can generate flashes of light that are so short that femtosecond timescale movement is effectively frozen in time like a photographic camera is able to make a still image of an actual moving object. Furthermore, modern ultrafast optics is not only able to generate femtosecond short optical pulses but also to precisely control the electromagnetic waveform in its carrier-envelope phase, which is essential for controlling electrons with attosecond precision.

This thesis explores how one can use optical pulses to control electrons or, more generally, electronic devices. The fundamental mechanism applied is the force F the electric field E imposing on all charged particles q, $F = qE$. An AC electric field of a lightwave $E(t) = \sin(2\pi f_0 t)$ with frequency f_0 is capable of driving the motion of electrons on the time scale of a single period $T = 1/f_0$ of the wave, with acceleration $a(t) = (q/m_e)\sin(2\pi f_0 t)$. Thus, controlling the lightwave means directly controlling the motion of electrons at the frequency of the lightwave. To gain an understanding of how to actually control the lightwave in the first place, the following sections give a very brief introduction on how to mathematically describe ultrafast optical pulses and how nonlinear optical interactions allow one to generate, amplify, and control optical pulses as experimentally done in this thesis.

2.1.1 Description of Optical Pulses

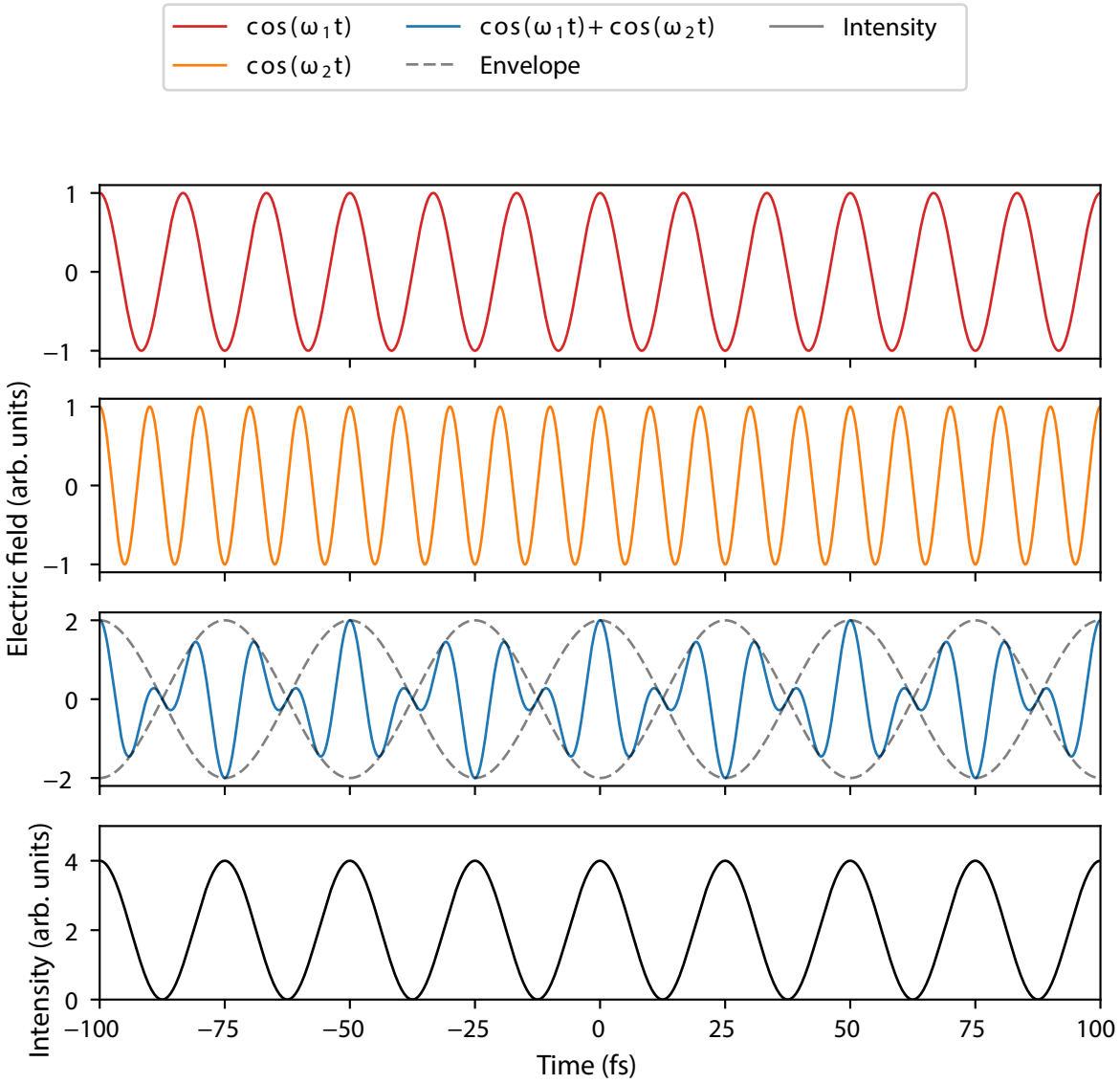

Figure 2.1: **Interference of Two Optical Waves:** Example case of two pure CW waves with frequencies of 100 THz and 60 THz interfering to form a train of optical pulses. The bottom row shows the intensity of the interfering waves.

An optical pulse is a superposition of multiple monochromatic plane waves that interfere to form a localized intensity peak in time. So, the electric field of a pulse $E(t, z=0)$ at an arbitrary position can be described by the sum of plane waves with frequency ω_n, phase ϕ_n and amplitude a_n,

$$E(t) = \mathrm{Re}\{\sum_{n=0,1,2,\ldots,j} a_n e^{i(\omega_n \cdot t + \phi_n)}\}. \tag{2.1}$$

To explain this concept one can use a thought experiment of two sine waves interfering to form an optical pulse train. Fig. 2.1 shows two pure cosine waves with frequencies $\omega_1 = 2\pi \cdot 60\,\mathrm{THz}$, $\omega_2 = 2\pi \cdot 100\,\mathrm{THz}$ and a constant phase relationship $\phi_1 = \phi_2 + c$, interfering in time

to form a train of optical pulses, the bottom row shows the intensity distribution $I(t) = |E(t)|^2$. The frequency domain representation is shown in Fig. 2.2. The pulse train is spaced with $1/25$ fs $= 40$THz, referred to as the repetition rate $f_{\text{Rep.}}$. Individual pulse envelopes contain only a single cycle of the optical wave within the full width at half maximum (FWHM) of the intensity envelope and are called single-cycle pulses. Furthermore, the phase of the electric field with respect to the envelope changes with every repetition of the pulse by π. This phase is called the carrier-envelope phase (CEP) and in this case, it repeats itself with a frequency of 20 THz, which is called the carrier-envelope offset frequency f_{CEO}. This frequency f_{CEO} is the

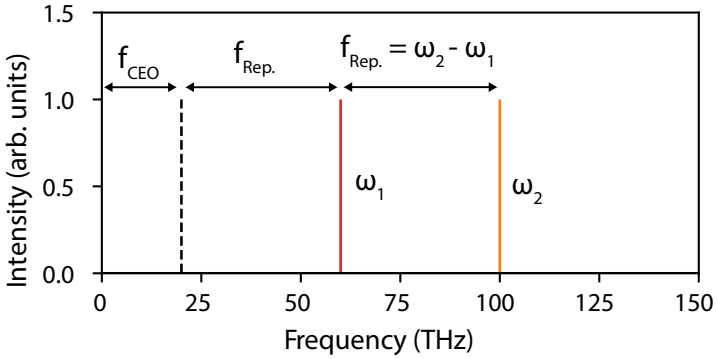

Figure 2.2: **Frequency Domain Representation of a Pulse Train Formed by Two Waves:** Frequency domain of two pure continuous waves (CW) waves with frequencies of 100 THz and 60 THz interfering to form a pulse train. In addition, the associated repetition rate $f_{\text{Rep.}}$ and the carrier-envelope offset frequency f_{CEO} of the frequency comb are shown.

difference between the fundamental lines ω_n of the pulse train and multiples of the repetition rate $nf_{\text{Rep.}}$ with $n = 1,2,3,\ldots$, $f_{\text{CEO}} = \omega_1 - 1f_{\text{Rep.}}$. Only for the case of $f_{\text{CEO}} = 0$, the pulse train will have a stable waveform, with the same CEP every pulse. Of course, this pulse train is a thought experiment since for most practical pulse sources, the temporal spacing between pulses is on the order of milliseconds to nanoseconds. This generates a much higher line density in the frequency domain, with kilohertz to gigahertz spacing, which is also why this is referred to as a frequency comb, with many individual CW lines contributing to a broadband optical pulse. Pulses, as experimentally generated in Chapter 5, are therefore usually written as a continuum of monochromatic waves with an amplitude distribution $A(\omega)$ centered at ω_0,

$$E(t) = \text{Re}\{\int_{-1/(2f_{\text{Rep.}})}^{1/(2f_{\text{Rep.}})} A(\omega)\cdot e^{i(\omega\cdot t+\phi(\omega))}dt\} = \text{Re}\{A(t)\cdot e^{i(\omega_0\cdot t+\phi(t))}\}. \tag{2.2}$$

Fig. 2.3 shows an optical pulse very similar to the one presented Chapter 5, it has a 16 fs FWHM duration and a center wavelength of 2.7 µm. The solid line shows a cosine pulse with $\phi_{CEP} = 0$, which has the peak of the optical wave centered on the peak of the envelope. The dashed line shows an optical pulse with $\phi_{CEP} = \pi/2$. The CEP change is an essential control mechanism for the motion of electrons accelerated by the electric field of an optical pulse. In

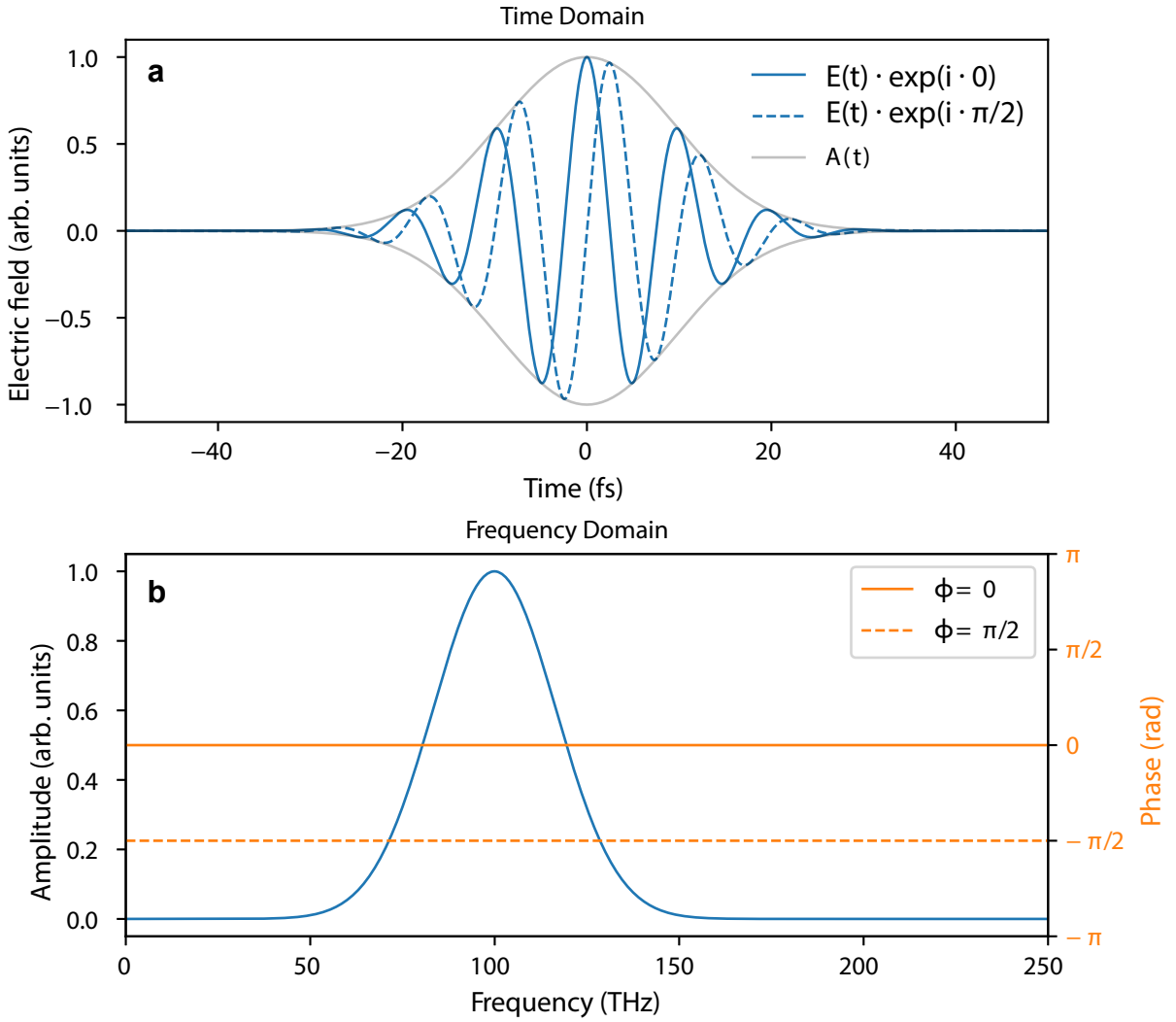

Figure 2.3: **Time and Frequency Domain of an Optical Pulse:** (**a**), the electric field of a 16 fs pulse with a center frequency of 100 THz and the carrier envelope phases of $\phi_{CEP} = 0$ and $\phi_{CEP} = \pi/2$. (**b**), Frequency domain of the two optical pulses shown on the left.

the frequency domain, a time-domain phase change of the carrier wave is a constant phase offset for all frequency components. Of course, this description of an optical pulse is not complete yet and does not consider spatial propagation. When extending the picture developed here, one can consider the full solution to the Helmholtz equation that describes a plane wave propagating in the z coordinate in a dielectric medium without free charges [56],

$$E(t,z) = \mathrm{Re}\{\int_{-\infty}^{\infty} A(\omega)\cdot e^{i(\omega\cdot t + k(\omega)\cdot z)}dt\}. \tag{2.3}$$

In particular, the term $k(\omega)\cdot z = \phi(\omega)$ gives the frequency-dependent spectral phase $\phi(\omega)$ that describes the phase delay of individual waves propagating a distance z through a material. $k(\omega)$ is related to the frequency with $k = n(\omega)\omega/c$, where $n(\omega)$ is the refractive index dependent on material and frequency and c the vacuum speed of light.

As we have seen, a constant phase offset is associated with the CEP of the pulse, and a linear phase slope is a shift in time of the pulse. However, all higher-order components of the phase, such as quadratic, cubic, etc., change the shape and relative frequency distribution of the optical pulse. Fig. 2.4 illustrates that concept by applying a quadratic phase, also called a chirp, to the pulse discussed above. The dispersed pulse changes its duration and the peak amplitude is

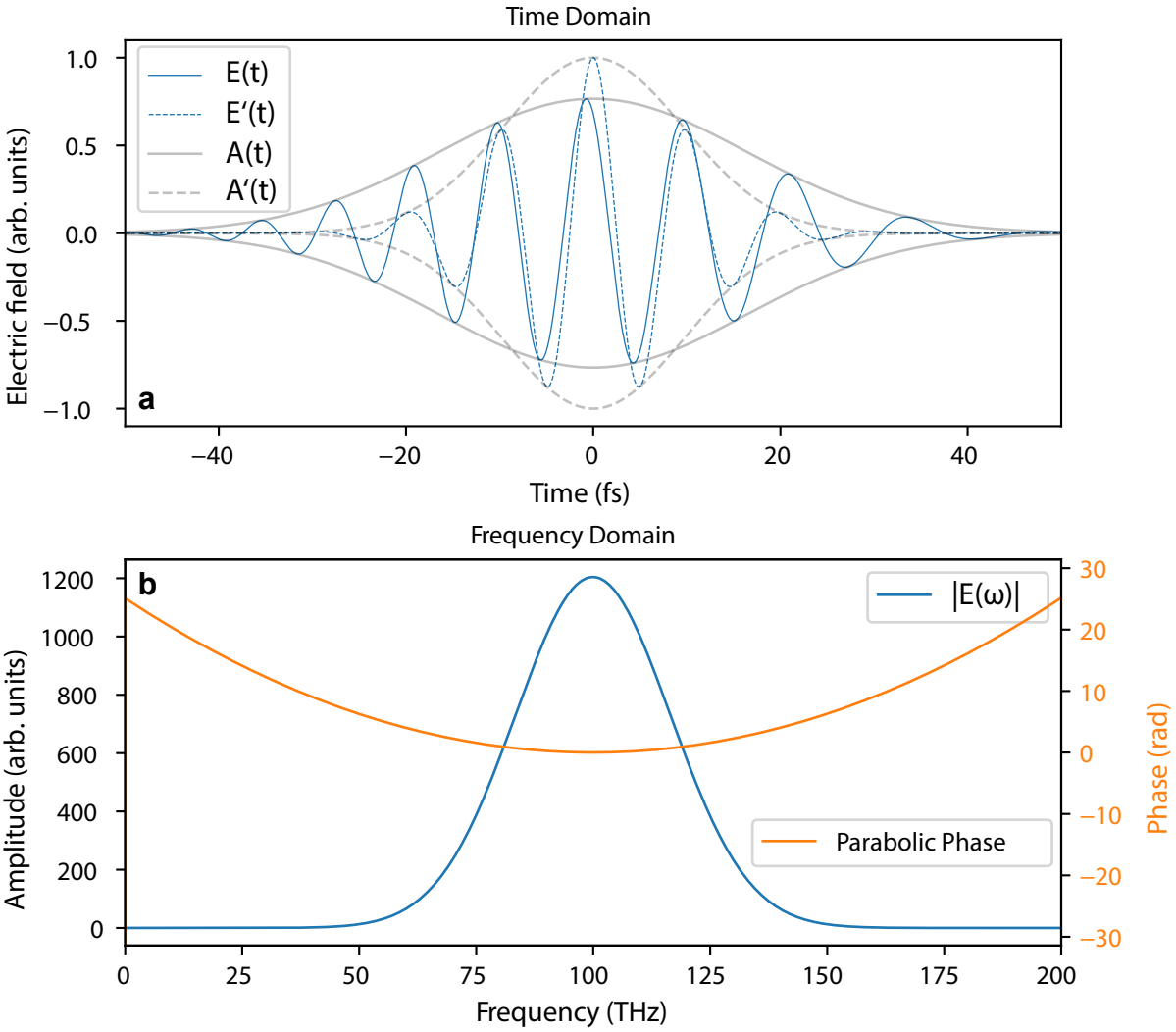

Figure 2.4: **Time and Frequency Domain of a Chirped Optical Pulse:** Dispersion of the optical pulse through a quadratic spectral phase in the time (**a**) and frequency domain (**b**). Solid lines show the dispersed pulse $E'(t), A(t)$ and dashed lines the original $E(t), A(t)$ pulse.

reduced. Furthermore, it can be seen for this particular case of negative dispersion that higher frequencies arrive first, while slower frequencies arrive later. This means that the spectral phase is an important property in the description of optical pulses, as it directly influences the temporal shape of the pulse. It is common to consider the Taylor expansion of the spectral phase to

understand the different types of dispersion that influence the pulse shape.

$$\phi(\omega) = \phi(\omega_0) + \underbrace{\left(\frac{\partial}{\partial\omega}\phi(\omega_0)\right)}_{\tau_g(\omega_0)} \cdot (\omega - \omega_0) + \underbrace{\left(\frac{1}{2}\frac{\partial^2}{\partial\omega^2}\phi(\omega_0)\right)}_{D_2(\omega_0)} \cdot (\omega - \omega_0)^2 + \dots \,. \tag{2.4}$$

The first order term is called the group delay $\tau_g(\omega_0)$ and the second order is called the group delay dispersion $D_2(\omega_0)$. However, as considering the first two orders of the Taylor-series evaluated at ω_0 is a good approximation for relatively narrowband pulses, it is not sufficient anymore for pulses where the spectral bandwidth approaches or exceeds one octave. When describing such pulses it is better to consider the full frequency-dependent group delay $\tau_g(\omega)$ considering all higher orders and not just as a truncated Taylor-series. Thus, the spectral phase is written as

$$\phi(\omega) = \underbrace{\left(\frac{\partial}{\partial\omega}\phi(\omega)\right)}_{\tau_g(\omega)} \cdot \omega = \left(\frac{\partial}{\partial\omega}k(\omega)\right) \cdot z \cdot \omega. \tag{2.5}$$

The expression $\left(\frac{\partial}{\partial\omega}k(\omega)\right)$ is particularly useful as it describes the the group delay acquired per unit of distance of propagation in a specific medium. By using the Sellmeier equation for the respective material, one can compute the dispersion of broadband pulses without approximation.

2.1.2 Nonlinear Optics

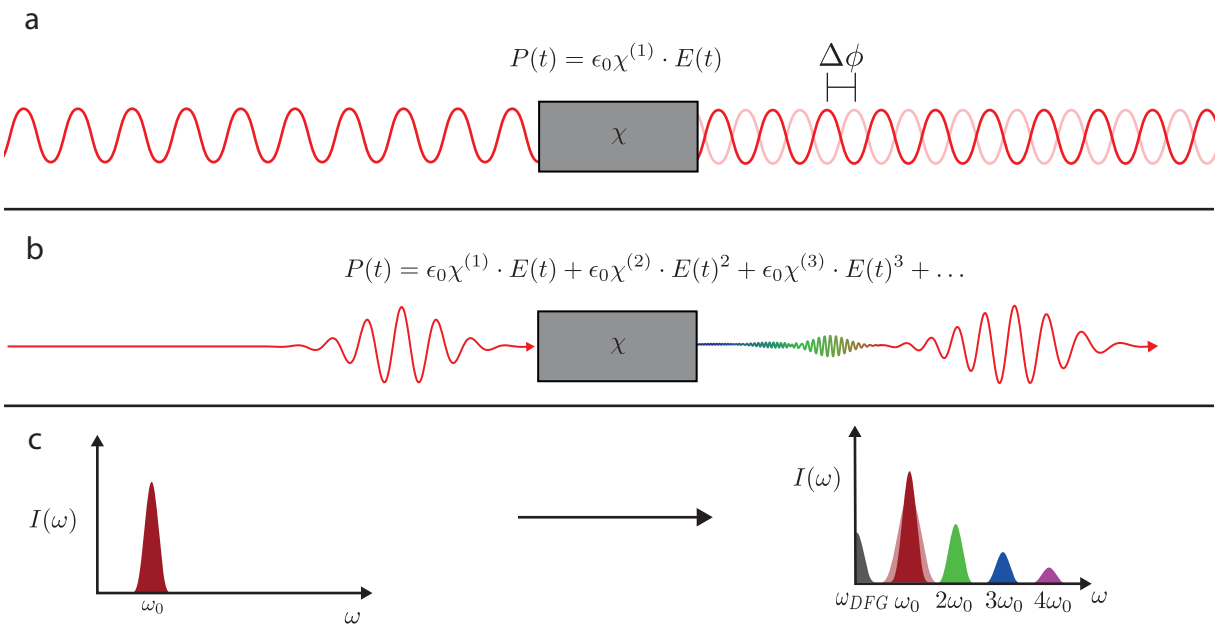

Figure 2.5: **Linear and Nonlinear Polarization Response of Matter:** Overview of how light interacts with matter comparing linear to nonlinear interaction. **a**, linear polarization response of matter to a CW lightwave. **b**, nonlinear polarization response of matter to a broadband optical pulse. **c**, spectral representation of nonlinear interaction process.

Nonlinear optics describes how strong electromagnetic waves drive the polarization of matter and are able to cause a nonlinear response. Such a nonlinear interaction gives rise to many interesting phenomena, such as the mixing of different frequencies, the creation of higher harmonics of the fundamental frequency or spectral broadening of frequency components. In the context of this thesis, nonlinear optics plays an essential role in the generation of ultrashort few-cycle pulses, as it allows one to modify the frequency content of optical pulses or amplify them with broad bandwidth. Many textbooks give an excellent description of such processes, in particular, "Nonlinear Optics" by Robert Boyd [57], which is loosely followed in this section.

As described in the previous section, optical pulses experience a frequency-dependent phase delay in dielectric media, physically caused by the linear polarization response of the medium having a frequency-dependent transfer function of the phase to the driving wave (see Fig. 2.5 a), identical to the case of a damped driven harmonic oscillator. This mechanism is described by the wave equation where the nonlinear polarization $P(t)$ acts as a source term [57],

$$\nabla^2 E(t) - \frac{n^2}{c^2}\frac{\partial^2}{\partial^2} E(t) = \frac{1}{\varepsilon_0 c^2}\frac{\partial^2}{\partial^2} P(t). \tag{2.6}$$

For clarity, this equation intentionally simplifies the actual case, and does not consider damping. In this case the electric field and the polarization are always in phase. Considering electrical

fields that are sufficiently strong, the polarization becomes anharmonic and new frequency overtones are generated, as depicted in Fig. 2.5 b for a few-cycle pulse. In such a case, the complex polarization response $P(t)$ can be expressed as a power series,

$$P(t) = \varepsilon_0 \left(\chi^{(1)} E(t) + \chi^{(2)} E^2(t) + \chi^{(3)} E^3(t) + \dots \right), \tag{2.7}$$

using the susceptibilities $\chi^{(n)}$ and the driving electric field $E(t)$. The susceptibilities $\chi^{(2)}$ and $\chi^{(3)}$ describe the generation of second and third harmonics and also many wave mixing processes utilized in this thesis. It is instructive to consider the second-order term to understand how the nonlinearity gives rise to new frequency components. With the driving field written as $E(t) = E_1 e^{-i\omega_1 t} + E_2 e^{-i\omega_2 t} + c.c.$, consisting of two CW waves of frequency ω_1, ω_2, the nonlinear polarization response is written as [57],

$$\begin{aligned} P^{(2)}(t) =& \varepsilon_0 \chi^{(2)} E^2(t) = \varepsilon_0 \chi^{(2)} (\\ & E_1^2 e^{-2i\omega_1 t} + E_2^2 e^{-2i\omega_2 t} : \text{Second Harmonic Generation (SHG)} \\ & + 2E_1 E_2 e^{-i(\omega_1+\omega_2)t} : \text{Sum Frequency Generation (SFG)} \\ & + 2E_1 E_2^* e^{-i(\omega_1-\omega_2)t} : \text{Difference Frequency Generation (DFG)} \\ & + \text{c.c.} \\ & + 2\left[E_1 E_1^* + E_2^* E_2\right]) . : \text{Optical Rectification} \end{aligned} \tag{2.8}$$

As can be seen, even a simple interaction of two waves in a nonlinear medium can give rise to a plethora of new waves with new frequency components. The ones relevant to this work are the second harmonic generation (SHG), which is frequency doubling in case of $\omega_1 = \omega_2$, and the difference frequency generation (DFG) process, which is used to produce CEP stable optical pulses and for optical parametric amplification (OPA).

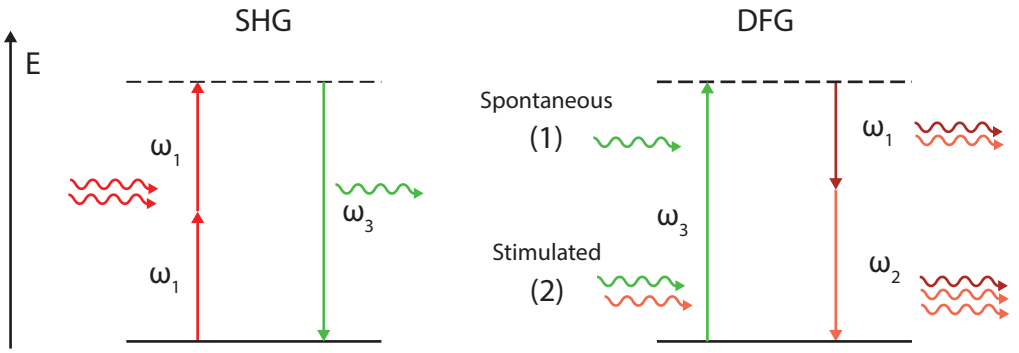

Figure 2.6: **Virtual Energy Level Diagram of SHG and DFG:** Diagram to explain the energy budget in an SHG and a DFG process, based on the use of a two-level virtual system. (1) marks a spontaneous downconversion process and (2) the stimulated case where a photon ω_2 seeds the downconversion process.

SHG describes the process of doubling the frequency of an incoming wave to twice the frequency. The virtual state diagram in Fig.2.6 shows in the photon picture how the energy of the two identical photons ω_1 is exciting the virtual state that instantly relaxes into the new third photon $\omega_3 = 2\omega_1$. This process is considered lossless, as the energy balance is fulfilled completely by the photon energies. A more detailed description is given by the two waves of amplitudes A_1, A_2, frequencies ω_1, ω_2 and wavevectors k_1, k_2 co-propagating inside the nonlinear medium along the z direction and experiencing coupling and exchange of energy,

$$\frac{dA_1}{dz} = \frac{i\omega_1^2\chi^{(2)}}{k_1c^2}A_2A_1^*e^{-i\Delta kz} \tag{2.9}$$

$$\frac{dA_2}{dz} = \frac{i\omega_2^2\chi^{(2)}}{k_2c^2}A_1^2e^{i\Delta kz}. \tag{2.10}$$

$$\Delta k = 2k_1 - k_2 \tag{2.11}$$

The energy gain of the frequency-doubled wave is quadratically dependent on the amplitude of the first wave, and if A_1 is constant and $\Delta k = 0$, the gain of A_2 is linear with the propagation in z. However, in most practical systems, this is not the case, A_1 can be depleted, and one typically is dealing with multiple frequencies, meaning that $\Delta k = 0$ is not satisfied for all frequencies. Practically, phase-matching is achieved either through the use of birefringent materials or quasi-phase-matching schemes. For an in-depth discussion of these cases, refer to the discussion in reference [57].

The case of DFG considers an incoming wave of amplitude A_3 that transfers energy to two lower frequency waves A_1, A_2, while maintaining energy conservation $\omega_3 = \omega_1 + \omega_2$. As the choice of generated frequency ω_1, ω_2 is in principle arbitrary, it is experimentally limited by phase-matching conditions. To write down the coupled wave equations, we treat the incoming wave ω_3 as constant again,

$$\frac{dA_1}{dz} = \frac{i\omega_1^2\chi^{(2)}}{k_1c^2}A_3A_2^*e^{i\Delta kz} \tag{2.12}$$

$$\frac{dA_2}{dz} = \frac{i\omega_2^2\chi^{(2)}}{k_2c^2}A_3A_1^*e^{i\Delta kz} \tag{2.13}$$

$$\Delta k = k_3 - 2k_1 - k_2. \tag{2.14}$$

Remarkably, it becomes obvious from these equations that neither wave A_1 nor A_2 can grow without one or the other wave being present. However, practically, downconversion still occurs even spontaneously without ω_1 and ω_2 and is used, for example, in the generation of entangled photon pairs in the case of quantum optics. This effect is explained by A_1 and A_2 never actually having an amplitude equal to zero, since the ground state of the electric field always has some amplitude, which is known as quantum vacuum fluctuations [58]. Furthermore, a DFG process can be efficiently used for the amplification of signals, which is known as optical parametric

amplification (OPA). In OPA A_3 is usually noted as the wave with the highest amplitude and frequency, and is referred to as the pump. The pump provides gain to an incoming wave with amplitude A_1 (signal), by transferring energy from A_3 to A_1 and an auxiliary third wave A_2, known as the idler. The whole process is attractive for the generation of broadband pulses with microjoule level energy (or more), as extremely broadband phase matching can be achieved with birefringent crystals and noncollinear propagation of the signal and pump. This process is then called non-collinear OPA (NOPA). An in depth discussion and design strategies for practical implementations are found in [59]. In addition, OPAs have another interesting advantage for high-energy pulses, as the whole process has no losses as a result of effectively no absorption in the material. Therefore, they are able to sustain very high average power without suffering from thermal effects. An experimental implementation of a broadband NOPA is described in Chapter 5.

Another very important attribute of DFG and OPA is that they can be used to generate CEP-stable pulses. In the previous chapter, for the sake of clarity, it was neglected that optical pulses can change the CEP from pulse to pulse, which is known as the carrier-envelope offset frequency f_{CEO} and $f_{\mathrm{CEO}} \neq 0$ for any practical laser oscillator or pump laser, if not specifically stated otherwise. A way to get rid of this CEP slip from pulse to pulse is to use a DFG-based process as the idler phase is the relative phase difference between pump and seed. This can be understood when considering two waves $E_1(t) = e^{i(\omega_1 t+\phi_1} + \text{c.c.}$ (signal) and $E_2(t) = e^{i(\omega_3 t+\phi_3} + \text{c.c.}$ (pump) and the results of Eq. 2.8. The DFG term is written as

$$P^{(\mathrm{DFG})}(t) = 2E_1E_2e^{-i((\omega_3-\omega_1)t+\phi_3-\phi_1)} + \text{c.c.}\,. \tag{2.15}$$

With this, the resulting idler phase now only depends on the relative phase difference $\Delta\phi = \phi_3 - \phi_1$. When $\phi_{3,1} := \phi_{\text{Phase Slip}}$, share the same phase slip $\phi_{\text{Phase Slip}}$, the resulting idler CEP would depend only on the interferometric stability between the signal and the pump. Experimentally, this is realized by deriving the pump and signal from the same laser source, without frequency doubling/tripling any of the two. Furthermore, the relative phase between the signal and the pump can also be used to directly control the idler CEP, by simply delaying one or the other over the length of an optical cycle. This shows how DFG is an useful process for generating CEP-stable optical pulses and is an important cornerstone of this thesis.

2.2 Electron Emission

Photoinduced electron emission is one of the classic research objects in optics, first observed more than 120 years ago in the form of the photoelectric effect by P. Lenard [60], and later explained by A. Einstein [61]. They discovered that a current can be measured between a metal surface and a biased anode, when a photon of sufficiently high energy hits the metal surface. Today, with the advent of ultra-short and higher-order-energy laser pulses, photoemission in the nonlinear regime and on the attosecond timescale is extensively studied and has enabled important research, such as the generation of XUV attosecond pulses via high-harmonic generation or femtosecond angle-resolved photoemission spectroscopy unveiling the dynamics of matter[3, 11, 62]. Historically, cold field emission [63], which is tunnel emission induced by strong DC electric fields, was a critical tool in the development of electron emitters. Naturally, this was adapted for AC fields and in particular for optical frequencies by illuminating sharp metal tips with few-cycle laser pulses. This allowed the generation of attosecond electron pulses with very accessible laser systems, such as Ti:Sapphire oscillators [7]. In comparison to electron emission from gas-phase atoms, the emission from the solid state brings the benefit of a reduced work function ϕ, making the emission much more accessible to lower pulse energy and less complex laser systems. With integrated nanophotonics, as studied in this thesis, it is possible to create tunnel emission induced by optical pulses with only picojoules of energy. This chapter gives a brief introduction to electron emission from metal surfaces and more specifically a description of the scaling laws and the sub-cycle dynamics of electron emission. A detailed discussion of this topic is also found in [64, 65].

2.2.1 Scaling Laws and Sub-Cycle Dynamics

There are three predominant emission pathways for photoinduced electron emission from a metal, the photoelectric effect, multiphoton photoemission, and tunnel emission; see Fig. 2.7. In a metal, electrons occupy a continuum of states up to the Fermi level E_F, following the Fermi-Dirac distribution. For electron emission, the dominant emission contribution is from electrons close to the Fermi level. The simplest pathway, the photoelectric effect, is explained by the photon energy $\hbar\omega$ that exceeds the work function of the metal W_F and raises an electron from a bound state close to the Fermi level to an unbound state, with the residual kinetic energy of the now free electron $E_{\text{Kin.}} = \hbar\omega - W_F$. The emission rate of the photoelectric effect scales linearly with the intensity of the lightwave $|E|^2$ and the measured current is described with $\Gamma(E) \propto |E|^2$. However, it was found that not only linear photoemission, but also multiphoton and tunnel emission can occur under sufficiently strong electric fields. For the case of multiphoton emission, an electron is excited by multiple photons ($n \geq 2$) into the continuum, and the number of photons necessary is dictated by the work function with $W_F < n\hbar\omega$ with $n = 2, 3, \ldots$. In analogy to the case of a single photon, the residual kinetic energy is $E_{\text{Kin.}} = n\hbar\omega - W_F$. The other pathway

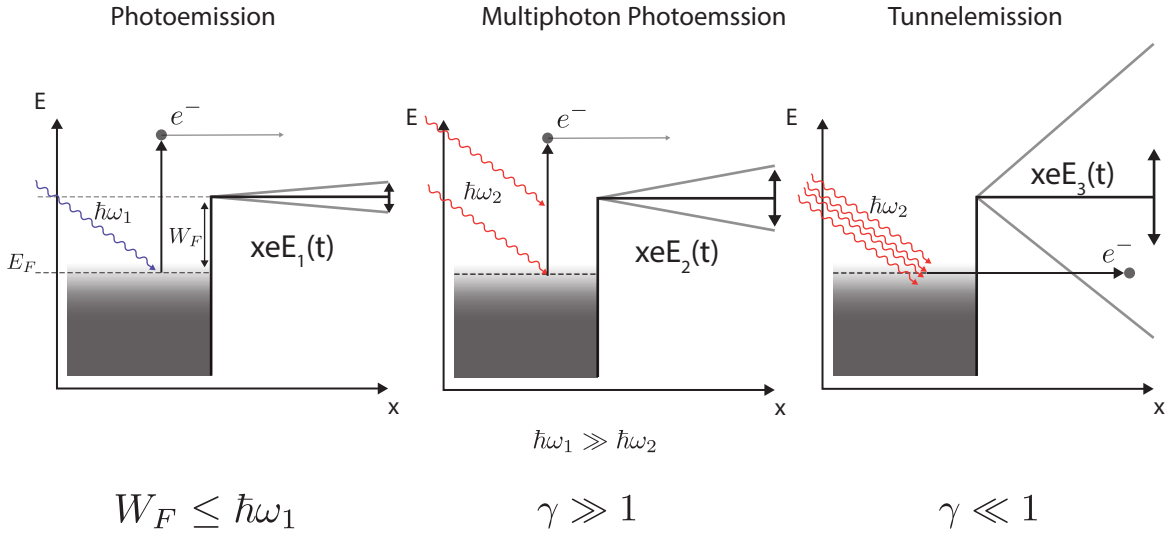

Figure 2.7: **Photoemission Pathways:** Energy diagramms of three different photoemission pathways. Showing photoemission, multiphoton photoemission, and tunnel emission. With γ noting the Keldysh parameter, E_F the Fermi energy level, and W_F the work function. $xeE_i(t)$ denotes the different slopes of the potential barrier with the applied electric field $E_i(t)$.

for an electron to escape from a metal is direct tunneling, which can occur only in the case of a finite barrier width. Considering a strong electric field, the potential landscape is so heavily distorted by the electric field that the barrier becomes finite; see Fig. 2.7. The scaling laws of these two processes were theoretically discussed by L.V. Keldysh for the ionization of atoms and later adapted by Bunkin and Fedorov for the emission from metal surfaces [66, 67]. They derived the cycle-averaged ionization rates scaling from the multiphoton to the tunnel emission regime. A main result of their work is known as the Keldysh parameter $\gamma = \omega\frac{\sqrt{2m_eW_F}}{eE}$, which describes when which pathway is dominant; m_e notes the electron mass, e the elementary charge, E the electric field amplitude of the AC exciting field, and ω the frequency of the AC field. When $\gamma \ll 1$, then tunnel emission is the dominant pathway when $\gamma \gg 1$ multiphoton photoemission is dominant. More intuitively, this is rewritten as $\gamma = \sqrt{\frac{W_F}{2U_P}}$, with a ponderomotive energy $U_p = \frac{q^2E_0^2}{4m\omega^2}$. This means that whenever the ponderomotive energy surpasses the work function, tunnel emission will be dominant, and vice versa for small ponderomotive energy. The ionization rates $\Gamma(E)$ for the atomic ionization case and high and low γ, can be approximated, with exponential precision, with a single analytical model that also describes the transition regime $\gamma \approx 1$ [64],

$$\Gamma(\gamma) \propto \exp\left(-\frac{2\phi}{\hbar\omega}\left(\left(1+\frac{1}{2\gamma^2}\right)\operatorname{arcsinh}(\gamma) - \frac{\sqrt{1+\gamma^2}}{2\gamma}\right)\right). \tag{2.16}$$

The limit cases of small and large gamma will yield the known formulas for multiphoton and tunneling emission rates with exponential precision,

$$\Gamma(E) \propto E^{\frac{2W_F}{\hbar\omega}}, \qquad \text{for } \gamma \gg 1 \tag{2.17}$$

$$\Gamma(E) \propto \exp\left\{\left(-\frac{4\sqrt{2m_e}W_F^{3/2}}{3e\hbar E}\right)\right\}, \qquad \text{for } \gamma \ll 1. \tag{2.18}$$

The rates are plotted in Fig. 2.8, for the case of $\omega = 2\pi$ 100 THz and $W_F = 5.1$ eV (Au), corresponding to the case discussed in chapter 6. As stated above these rates are stated only

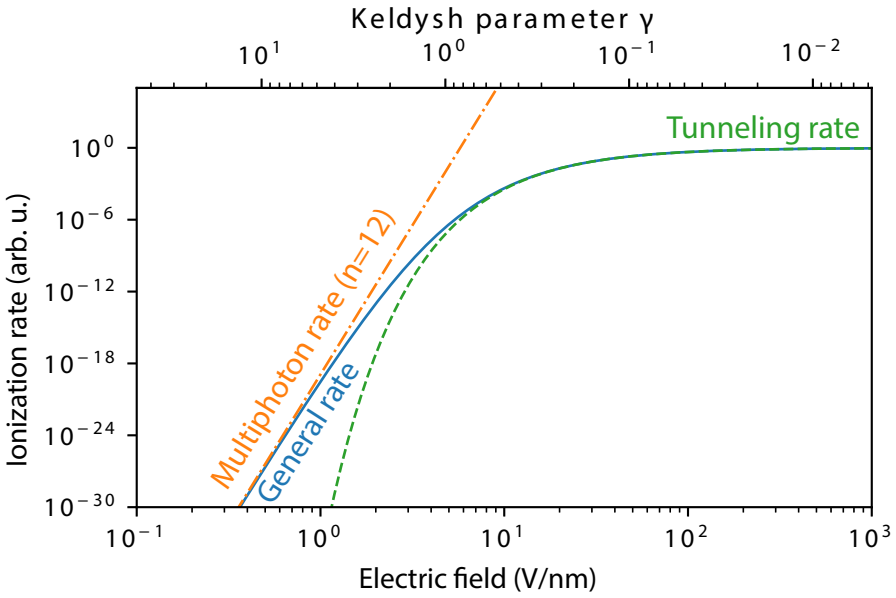

Figure 2.8: **Ionization Rates:** Ionization rates with exponential precision as a function of electric field for the general case and for limit cases of multiphoton and tunnel emission.

with exponential precision and for ionization rates from atoms. For the case discussed in this thesis, we will now limit our case to values of $\gamma \leq 1$ and emission from a metal surface into vacuum. In the case of nanophotonics dealing with near-infrared (NIR) few-cycle laser and field strength in excess of 10 V nm^{-1}, it was experimentally found that the approximation of quasi-static tunneling emission, corresponding to $\gamma \ll 1$, describes the experimental data sufficiently well [8–10, 20, 23, 68].

The quasi-static tunneling rates as described for a DC field by Fowler and Nordheim and for AC fields by Bunkin and Fedorov [63, 67], give not only a good description of the cycle-averaged rates, but allow us to calculate the sub-cycle dynamics as well. The current density as a function of electric field strength E,

$$\Gamma(E) = \frac{e^3}{16\pi^2\hbar W_F}E^2 \exp\left(-\frac{4}{3}\frac{\sqrt{2m_e}W_F^{3/2}}{\hbar eE}\right), \tag{2.19}$$

is comparable to the approximation above, except for a quadratic field component as a prefactor. With this equation, we have an ionization rate that instantaneously follows the electric field and is used to approximate the electron emission within a half-cycle of the electric field. Assuming an optical pulse as discussed in the previous section, we can see in Fig. 2.9, how the highly nonlinear tunneling rate, forms an electron pulse that is much shorter than a half-cycle. With the instantaneous current following the electric field, it becomes clear that the electric field is fully defining the temporal shape of the electron emission.

Of course, there are limits to the quasi-static approximation, when $\gamma > 0.5$, the emission regime is considered to be non-adiabatic and multiphoton processes start to slowly dominate, smearing out the sub-cycle nature of the current [65]. This transition regime is extensively discussed by Yudin and Ivanov [69] and becomes exceedingly more complicated than the simple models presented previously. Also, numerical integration of the time-dependent Schrödinger equation can be used to describe the sub-cycle dynamics more accurately, as shown by Yalunin et al. [65].

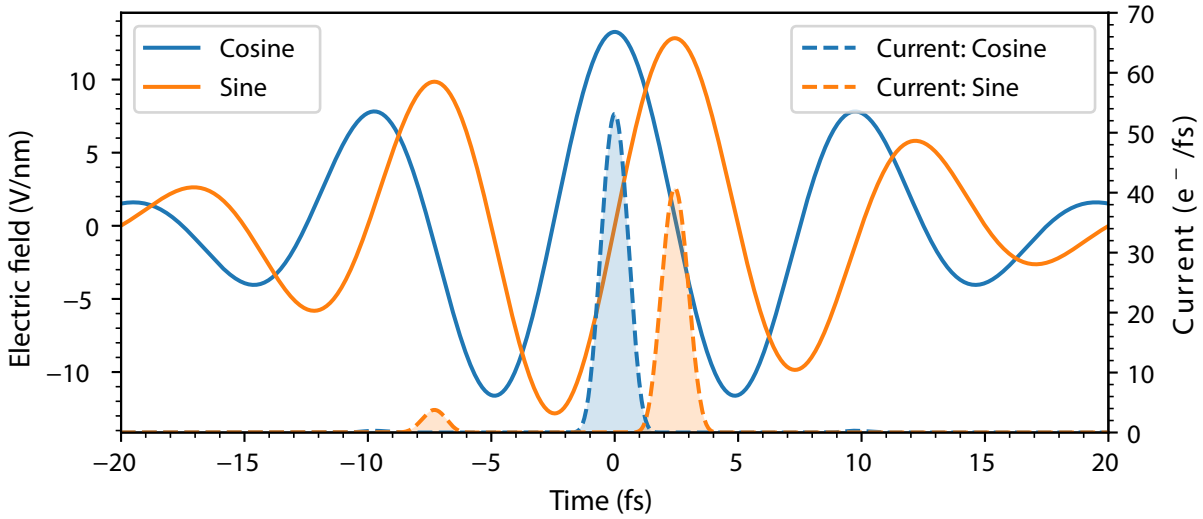

Figure 2.9: **Instantaneous Current Rates:** Instantaneous current driven by a few-cycle MIR pulse with a cosine and a sine shape. Rates are adapted from [23] for a 300 nm^2 gold surface.

3 On-Chip Sampling of Optical-Fields with Attosecond Resolution

[1]Time-domain sampling of arbitrary electric fields with sub-cycle resolution enables complementary time-frequency analyses of a system's electromagnetic response. Such time-frequency analyses provide dynamic information that is not furnished by absorption spectra alone. Accordingly, sub-cycle, time-domain sampling has proven critical to the understanding and design of electronic systems, and has revolutionized spectroscopy in the terahertz spectral region [70, 71]. Commercial THz time-domain spectroscopy systems are now readily available and often used for industrial applications such as chemical and material analysis. Sub-cycle field sampling in the THz regime has also been instrumental to many fundamental scientific investigations, including the tracing of electron wavepacket dynamics in quantum wells [72], the investigation of dynamic Bloch oscillations in semiconductor systems [73], the observation and characterization of quantum vacuum fluctuations [58], and other nonlinear phenomena [49].

If readily available, sub-cycle optical-field sampling in the visible to near-infrared (near-IR) spectral regions would likewise provide great benefit to both science and industry. For example, attosecond streaking spectroscopy has been used to study the role of optical-field-controlled coherent electron dynamics in the control of chemical reaction pathways [74] and to investigate petahertz-level electrical currents in solid-state systems [12, 13, 15]. It was also recently shown that sub-cycle field sampling of the free-induction decays of biological systems can provide an order of magnitude reduction in the limits of detection and improved molecular sensitivity compared to traditional frequency-domain spectroscopic methods [48]. Despite these compelling results, scaling such techniques into the near-IR and visible spectral regions has remained challenging. While the manipulation of attosecond electron wave packet emission [15–17], electro-optic sampling [52], and attosecond streaking in the visible to near-IR spectral regions [3, 75, 76] have proven to be viable paths towards direct optical-field sampling in the time-domain, these techniques are seldom accessible, requiring large driving pulse energies, and accordingly, large laser amplifier systems, bulky apparatuses, and in some cases vacuum environments [4, 15, 16, 48]. Currently, there is no compact and integratable sub-cycle optical field sampling technology with the bandwidth and field sensitivity required for real-world applications of interest in the visible to near-IR spectral regions.

To address this lack of compact and integratable tools for optical-field sampling in the visible to near-IR, we have developed and demonstrated an on-chip, sub-optical-cycle sampling technique for measuring arbitrary electric fields of few-fJ near-IR optical pulses in ambient conditions. To our knowledge, this represents an improvement of roughly six orders of magnitude in energy sensitivity relative to the current state of the art in this spectral range. Our work leverages the sub-cycle optical-field emission from plasmonic nanoantennas [77–81] to achieve petahertz-level sampling bandwidths using only picojoules of energy [7, 9, 10, 68]. Further-

[1]This chapter is based on the work published in Nature Photonics; see Ref. [20]. The author of this thesis is a shared first author, among Mina Bionta and Marco Turchetti, of the published work and was involved the design of the experiment, conduction of the experiment, analysis of the presented data, development of the theoretical sampling description and in the writing of the manuscript.

more, by electrically connecting the nanoantenna arrays via nanoscale wires, the field samplers we demonstrate here are amenable to large-scale electronic integration [23]. Beyond demonstrating the feasibility of sub-cycle field sampling of petahertz-scale frequencies, our results also reveal *in situ* dynamical properties of the interaction of the driving optical-field waveform with the plasmonic nanoantennas. This work will enable the development of new tools for optical metrology that will complement traditional spectroscopic methods and unravel linear and nonlinear light-matter interactions as they occur at their natural time and length scales.

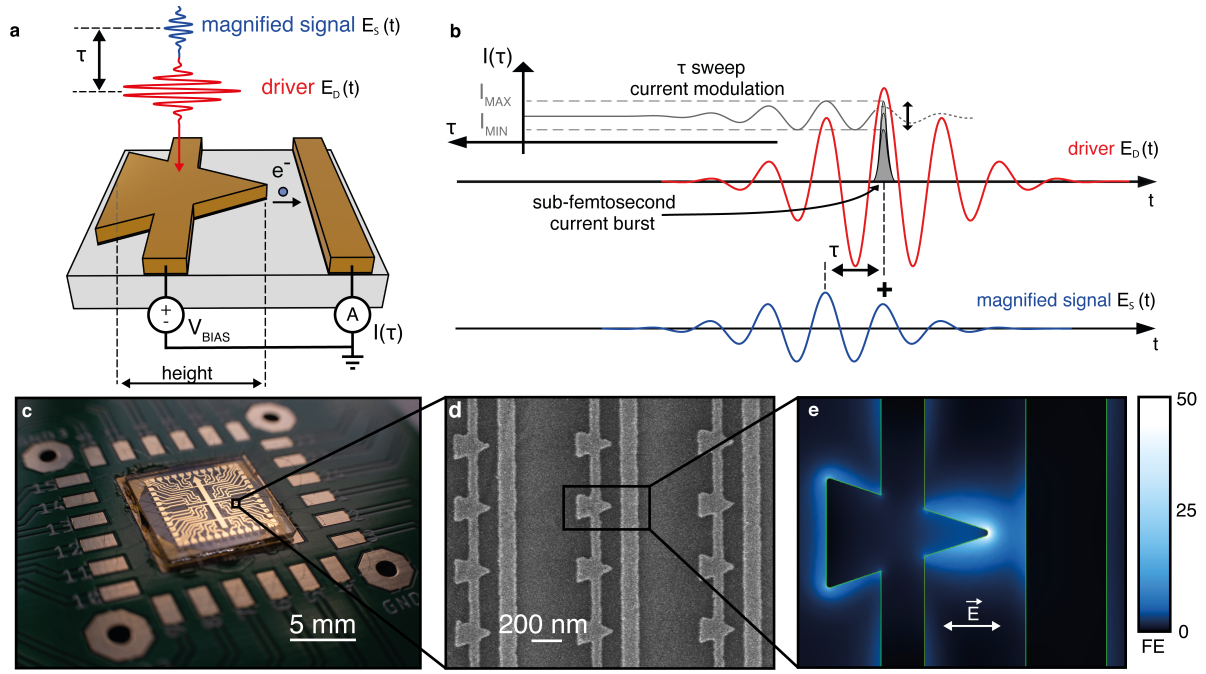

Figure 3.1: **Device overview.** **a,** Schematic of the device. **b,** Depiction of the optical-field sampling process. Attosecond electron bursts are driven from an electrically-connected gold nanoantenna (see **a**) by a strong optical waveform driver ($E_{\mathrm{D}}(t)$, red), collected by an adjacent gold wire, then measured using an external current detector (see Methods). The weak signal waveform ($E_{\mathrm{S}}(t)$, blue), with a peak intensity of 1×10^{-4} that of the driver pulses, modulates the average photocurrent generated by the driver pulse, $I(\tau)$, as a function of delay, τ (grey). The amplitude of the signal waveform is artificially magnified in **a** and **b** for visibility. **c,** Photograph of the nanocircuit embedded on printed circuit board. **d,** Scanning electron micrograph of the device. **e,** Simulated electric field enhancement around a nanoantenna. The maximum field enhancement is ∼35 (on resonance). FE: field enhancement factor. E: polarization direction of the incident electric field.

Our device is depicted in Fig. 3.1a. It consists of an electrically-connected plasmonic gold nanoantenna that functions as the electron source (cathode), a gold nanowire as an anode separated by a 50 nm air gap, and an external current detector. A photograph of the nanocircuit integrated onto a printed circuit board is shown in Fig. 3.1c. Devices were connected in parallel via nanowires and simultaneously excited to improve signal strength. A scanning electron micrograph (SEM) of the fabricated devices is shown in Fig. 3.1d.

When a strong driving pulse $E_{\mathrm{D}}(t)$ illuminates the nanoantenna/wire junction, a large local electric field $E_D^{(\mathrm{L})}(t)$ is generated at the nanoantenna tip. This incident electric field $E_{\mathrm{D}}(t)$ is related to $E_D^{(\mathrm{L})}(t)$ by the transfer function of the nanoantenna $\tilde{H}_{\mathrm{Pl.}}(\omega)$ given by the relationship $E_{\mathrm{D}}^{(\mathrm{L})}(t) = \mathscr{F}^{-1}\left(\tilde{H}_{\mathrm{Pl.}}(\omega)\cdot\tilde{E}_{\mathrm{D}}(\omega)\right)$, where $\mathscr{F}^{-1}$ is the inverse Fourier transform, and tildes indicate the frequency domain. The spectral field enhancement, which corresponds to $|\tilde{H}_{\mathrm{Pl.}}(\omega)|$, is shown in Fig. 3.1e near resonance (approximately 260 THz for the device shown in Fig. 3.1d). The peak on-resonant field enhancement near the emitter tip was calculated to be ~ 35. Due to the combined effect of the localized surface plasmon polariton [81] in the antenna and the geometric field enhancement resulting from the sharp radius of curvature [82], the locally-enhanced field can exceed the incident electric field of the driver pulse by more than one order of magnitude depending on the spectral overlap with the plasmonic resonance. If sufficiently strong, $E_{\mathrm{D}}^{(\mathrm{L})}(t)$ significantly bends the surface potential resulting in optical-field-controlled emission of electrons at the metal-vacuum interface [9, 10, 23, 65, 68, 69].

Due to the strong nonlinearity of the emission process, the electron bursts generated in the device are deeply sub-cycle and on the order of several hundred attoseconds for the case of near-IR fields [10, 83]. The weak incident signal field $E_{\mathrm{S}}(t)$ is similarly modified to create a weak local signal field $E_{\mathrm{S}}^{(\mathrm{L})}(t)$, but remains too weak to drive photoemission.

As demonstrated by Cho *et al.* [17], a short optical driving pulse in combination with a highly-nonlinear, sub-cycle emission process allows for field-resolved sampling of the signal pulse. For calculating the impact of $E_{\mathrm{S}}(t)$, on the total emission, a linearized small-signal model can be used. Consider the addition of $E_{\mathrm{S}}^{(\mathrm{L})}(t)$ as a function of delay τ relative to the strong driving field $E_{\mathrm{D}}^{(\mathrm{L})}(t-\tau)$ as shown in Fig. 3.1b. In our case, the detected current as a function of delay $I(\tau)$ is the time-average of the nonlinear emission rate Γ [63, 67] driven by the sum of the driver field $E_{\mathrm{D}}^{(\mathrm{L})}(t)$ and the small-amplitude signal field $E_{\mathrm{S}}^{(\mathrm{L})}(t-\tau)$,

$$I(\tau) \propto \int_{-\frac{T_{\mathrm{Rep.}}}{2}}^{\frac{T_{\mathrm{Rep.}}}{2}} \Gamma\left(E_{\mathrm{D}}^{(\mathrm{L})}(t-\tau) + E_{\mathrm{S}}^{(\mathrm{L})}(t)\right) dt, \tag{3.1}$$

where $T_{\mathrm{Rep.}}$ is the time between consecutive optical pulses. Given that $E_{\mathrm{S}}^{(\mathrm{L})}(t)$ is sufficiently small, we can Taylor-expand Γ around the local driver field $E_{\mathrm{D}}^{(\mathrm{L})}(t-\tau)$ to the first order. This enables the linearization of the measured emission $I(\tau)$ with respect to the signal $E_{\mathrm{S}}^{(\mathrm{L})}(t)$:

$$I(\tau) \propto \int_{-\frac{T_{\mathrm{Rep.}}}{2}}^{\frac{T_{\mathrm{Rep.}}}{2}} \left(\Gamma\left(E_{\mathrm{D}}^{(\mathrm{L})}(t-\tau)\right) + \left.\frac{\mathrm{d}\Gamma}{\mathrm{d}E}\right|_{E_{\mathrm{D}}^{(\mathrm{L})}(t-\tau)} \cdot E_{\mathrm{S}}^{(\mathrm{L})}(t)\right) dt. \tag{3.2}$$

The second term in equation (3.2) is a cross-correlation between $\left.\frac{\mathrm{d}\Gamma}{\mathrm{d}E}\right|_{E_{\mathrm{D}}^{(\mathrm{L})}(t-\tau)}$ and $E_{\mathrm{S}}^{(\mathrm{L})}(t)$, and denoted as $I_{\mathrm{CC}}(\tau)$. Due to the nonlinearity and sub-cycle nature of the emission process, the central most portion of the driving waveform dominates the measured time-integrated current, and acts a sub-cycle gate limiting interaction with the signal field (see Fig. 3.1b). This fact

becomes more evident when taking the Fourier transform of $I_{CC}(\tau)$, which simplifies to the following expression:

$$\tilde{I}_{CC}(\omega) \propto \mathscr{F}\left(\left.\frac{d\Gamma}{dE}\right|_{E_D^{(L)}(t)}\right)^* \cdot \tilde{E}_S^{(L)}(\omega), \tag{3.3}$$

where $\mathscr{F}\left(\left.\frac{d\Gamma}{dE}\right|_{E_D^{(L)}(t)}\right)^*$ is the the complex transfer function of the detector and is denoted as $\tilde{H}_{Det}(\omega)$. This function $\tilde{I}_{CC}(\omega)$ describes the full sampling response to the weak signal.

To experimentally verify the device performance, a CEP-stable, 78 MHz Er:fiber-based laser source was used [9], with a pulse duration of ∼10 fs full-width at half-maximum (FWHM) (∼2.5 cycles) and central wavelength of ∼1170 nm, locked to a fixed CEP. Laser pulse characterization can be found in Supplementary Information Sec. S2. A dispersion-balanced Mach-Zehnder interferometer was used to generate pairs of strong driver and weak signal pulses with a variable delay for the experiment. The driver and signal pulse energies (fields) were measured to be approximately 50 pJ (0.64 GV m^{-1} at focus) and ∼5 fJ (6.4 MV m^{-1} at focus) respectively. The two pulses were focused to a spot-size of 2.25 μm × 4.1 μm FWHM, illuminating 10-15 nanoantennas at a time. The pulses were linearly polarized along the height axis of the nanoantennas (Fig. 3.1a). Electron bursts were generated in the nanocircuit by the 50 pJ driver pulse, modulated by the 5 fJ signal pulse as the delay between the two pulses was scanned. The photocurrent was detected using a transimpedance amplifier in conjunction with lock-in detection. The signal pulses, with an intensity of 1×10^{-4} that of the driver pulses, were much too weak to drive photoemission on their own. By monitoring the photocurrent from nearly identical devices as a function of incident pulse energy, we concluded that the driving pulses were operating the devices in the optical tunneling regime where the emission follows a Fowler-Nordheim tunneling rate (see Refs. [9, 63, 65] and Supplementary Information Sec. S6). We emphasize that the experiment was performed in ambient conditions (*i.e.* in air and at room temperature). A schematic of the experiment is shown in Fig. 3.1a and in Fig. 3.5 with further details found in the Methods chapter, see Chap. 3.4.1.

3.1 Results and Discussion

Fig. 3.2 presents the measured cross-correlation $I_{CC}(\tau)$ (blue trace) for the tested antennas with a 240 nm height (from antenna base to tip, see Fig. 3.1a), and compares it to the computed simulated antenna response $E_S^{(L)}(t)$ (red trace) and the calculated incident field $E_S(t)$ (yellow trace), found by applying the measured spectral phase (see Supplementary Information Sec. S2) of the laser output to the measured intensity spectrum before converting back to the time domain. The 1σ-confidence interval (that is the interval ranging between plus and minus one standard deviation from the mean value) was calculated over all 60 scans and is shown as the light blue shaded region in Fig. 3.2. One standard deviation is ≈ 10 % of the peak amplitude. Considering the estimated peak field of around 6.4 MV m^{-1} for the incident field, the confidence interval

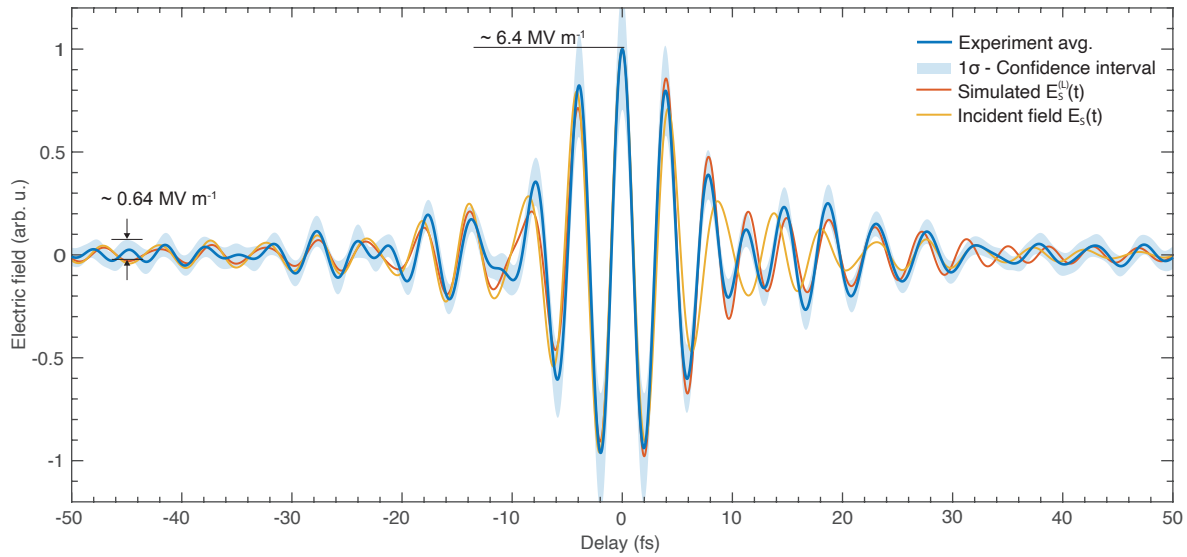

Figure 3.2: **Experimental field sampling results and analysis.** Time-domain results for devices with a height of 240 nm comparing measured (blue) and simulated near-fields ($E_S^{(L)}(t)$, red) to the calculated incident field ($E_S(t)$, yellow). Negative delays indicate that the driver pulse arrives before the signal pulse. The 1σ-confidence interval is shown as a blue shaded ribbon centered around the average value (blue solid line) retrieved from 60 scans. The plasmonic resonance of the antenna results in the dephasing in the time-domain between $E_S(t)$ and $E_S^{(L)}(t)$ observed around 12 fs. The label 6.4 MV m^{-1} at the center peak is indicating the approximated field strength corresponding to this peak. The label 0.64 MV m^{-1} at the left hand is indicating corresponding approximate field strength to the confidence interval.

is estimated around 640 kV m^{-1}. The measured trace (blue) shows significant deviations from $E_S(t)$ (yellow), especially in the pedestal from 5 fs to 20 fs. However, this measured pulse shape in the time domain (blue trace) is almost identical to $E_S^{(L)}(t)$ (red trace), both with a 180° dephasing near 12 fs with respect to $E_S(t)$ (yellow trace). Similar dephasing dynamics have been investigated by others in both nanoantenna and extended nanotip structures [84] and are a hallmark of the resonant electron dynamics excited within the nanoantennas.

In the frequency domain (Fig. 3.3), two prominent maxima are visible in the Fourier transform of the measured data (blue solid trace). These maxima are also exhibited in the simulation of the antenna response ($\tilde{E}_S^{(L)}(\omega)$, light blue dashed trace), but only one (at 218 THz) is observed in the measured spectrum of the incident field ($\tilde{E}_S(\omega)$, grey dotted trace). The second peak (at 257 THz) is due to the plasmonic response of the antenna $\tilde{H}_{Pl.}(\omega)$ which must be incorporated when calculating the electric near-field. The peak in the spectral phase of the measured data (red solid trace) is due to the plasmonic resonance of the antenna and closely matches the simulation of the antenna response (orange dashed trace). This spectral analysis further supports our conclusion that the observed discrepancies and dephasing between the incident field $E_S(t)$ and the measured pulse in the time-domain (Fig. 3.2) arise due to the resonant response of

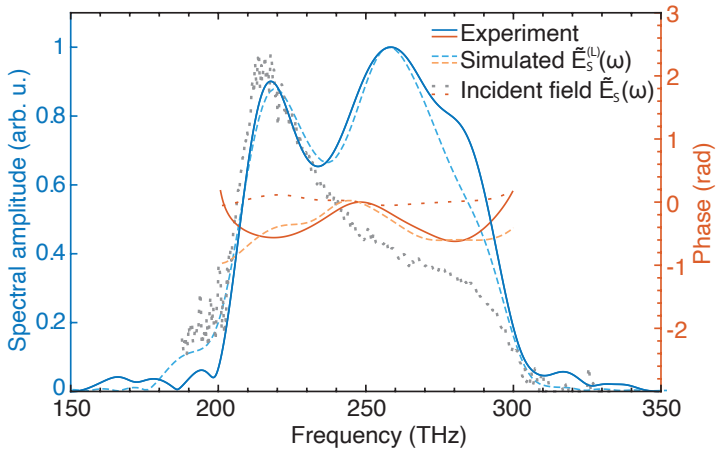

ja

Figure 3.3: **Frequency-domain of the experimental field sampling results** Frequency-domain comparison of measured (solid) and simulated ($\tilde{E}_S^{(L)}(\omega)$, dashed) near-fields for devices with a 240 nm height to the calculated incident laser field ($\tilde{E}_S(\omega)$, dotted). This on-resonant 240 nm device shows two peaks present in the cross-correlation data, one corresponding to the measured spectrum of the incident field (at 218 THz) and the other to the plasmonic enhancement of the antenna (at 257 THz).

the nanoantenna. The retrieved incident electric field deconvolved from $E_S^{(L)}(t)$ can be found in Chap. 3.4.7. Similar experimental results and analysis for 200 nm devices can be found in Chap. 3.4.11. The excellent agreement between the measured $I_{CC}(\tau)$ and $E_S^{(L)}$ in the temporal and spectral domains demonstrate that we are generating sufficiently short electronic gate windows to sample the complete local electric field waveform at the tips of the nanoantennae.

There are several practical considerations for sampling incident signal fields with such a detector. In our experimental data, we attribute the minor discrepancies with the the simulated model to slight uncertainties in the fabrication process, as well as to the multiplexed nature of our current detection scheme. As we illuminated 10-15 nanoantennas at a time, the measurements we show are an averaged trace, with all antennas contributing simultaneously to the detected current. When exposed to high-intensity illuminations (greater than $\sim 150\,\mathrm{pJ}$), the nanostructures experience some reshaping which can cause degradation and restabilization of the photocurrent as the field enhancement resonance shifts (see Chap. 3.4.5), which can affect the overall signal to noise ratio, but does not damage the devices to a point where they can no longer operate [9, 23]. The noise floor of the measurements is ultimately shot noise limited [23]. This adds a limitation to our detection scheme as the devices have a finite amount of time the laser can remain illuminating one spot without changing the resonance of the antenna. This can be overcome by devising methods for stabilizing the antenna shape which would improve the noise floor as well. Beyond these limitations, one must also take into account the intensity of $E_S(t)$. If comparatively strong, approximately three orders of magnitude below $E_D(t)$ and higher, nonlinear distortions will form. The distortions will be of the form $E_S^2(t)$ degrading the accuracy of the small-signal model. Finally, if the signal pulse reaches photon energies higher

than the work function of the emitter, linear photoemission due to single-photon absorption will cause a substantial background current placing an upper frequency limit of a gold device near 1 PHz.

Our detection scheme can be directly compared to hetero- and homodyne methods that are often used in techniques such as frequency-comb spectroscopy [85–87]. However, most frequency-comb spectroscopy measurements use detectors that respond only to the time-average optical intensity, and do not provide sub-cycle field gating, resulting in a narrower detection bandwidth that is confined to the amplitude spectrum of the local oscillator (*i.e.* the driver pulse). Recently, it has been shown that nonlinear gating techniques can be incorporated into frequency-comb spectroscopy systems to enable highly-broadband field-resolved spectroscopy throughout the mid-infrared [88]. Given their compact form-factor and ability to provide sub-cycle gating with a highly broadband detection response, nanoantenna detectors such as those presented in this work, could be incorporated into chip-scale platforms, and could enable simultaneous tracking of linear and nonlinear light-matter interaction dynamics into the near-infrared and potentially visible spectral regions.

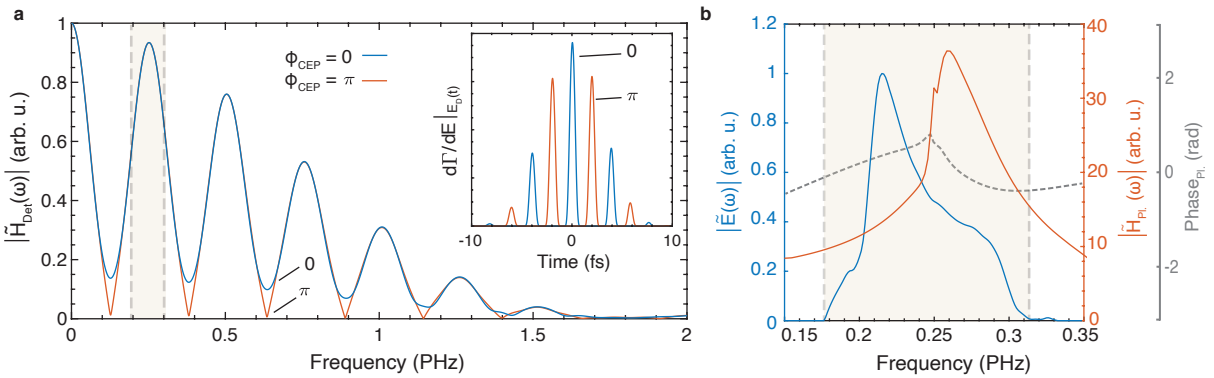

Figure 3.4: **Theoretical sampling bandwidth. a,** Calculation of the accessible sampling bandwidth $\tilde{H}_{\mathrm{Det}}(\omega)$ for the carrier-envelope phases $\Phi_{\mathrm{CEP}} = 0, \pi$ of the driver pulse (blue and red respectively). (Inset) The time-domain picture of $\frac{\mathrm{d}\Gamma}{\mathrm{d}E}\big|_{E_{\mathrm{D}}(t)}$ corresponding to the bandwidth shown in **a**. **b,** The spectral amplitude of the driving pulse ($|\tilde{E}_{\mathrm{D}}(\omega)|$, blue) and the plasmonic nanoantenna transfer function in amplitude $\left|\tilde{H}_{\mathrm{Pl.}}(\omega)\right|$ (red) and in phase (grey). The shaded area in **a** and **b** indicates the spectral region occupied by the driving pulse.

To investigate the highly-broadband nature of this technique, we can theoretically study $\tilde{H}_{\mathrm{Det}}(\omega)$ for electromagnetic frequencies outside of the tested spectral region. In Fig. 3.4a we show the calculation of $\tilde{H}_{\mathrm{Det}}(\omega)$ assuming our experimental driving pulse and antenna resonance, modeled from our experimental conditions, and are both shown in Fig. 3.4b for reference. For Γ, we used a quasi-static Fowler-Nordheim emission rate [9, 63, 65], which has been shown to accurately describe the tunneling emission from similar nanostructures for Keldysh parameters γ [66] on the order of but less than 1 [9, 65]. We calculate $\gamma \approx 0.9$ given our experimental conditions, and measurements of the power-law scaling of the electron emission with pulse energy

indicate driving intensities beyond the transition from multiphoton to the tunneling regime (see Chap. 3.4.8). Due to the highly-nonlinear, sub-cycle response of the emission rate on the driving electric field, we calculate that $\tilde{H}_{\mathrm{Det}}(\omega)$ spans several octaves from DC to more than 1 PHz (see Fig. 3.4a). The resultant small-signal gain enhances the response of the system to the weak signals of interest $\tilde{E}_{\mathrm{S}}^{(\mathrm{L})}(\omega)$ that would not be able to generate detectable electron emission signals on their own, even for wavelengths far outside of the driving pulse spectrum. We note the periodic structure in the plot of $\tilde{H}_{\mathrm{Det}}(\omega)$ shown in Fig. 3.4a is due to the presence of regularly-spaced electron pulses in the time domain modulating the amplitude of $\tilde{H}_{\mathrm{Det}}(\omega)$ (see inset of Fig. 3.4a). These pulses are spaced by one cycle of the driving laser, and change in number and strength depending on the carrier-envelope phase (CEP). However, for few-cycle pulses, such as those used in this experiment, the response remains relatively flat over the bandwidth of the driving pulse, and is only minimally affected by the modulation, which supports our experimental findings in Figs. 3.2 and 3.3. More detailed discussion of CEP and pulse duration effects can be found in Chap. 3.4.10 and 3.4.9.

3.2 Conclusion

While other direct time-domain optical sampling techniques for visible and near-infrared optical pulses currently exist [4, 15–17, 75, 76], they require nJ- to mJ-level pulse energies, bulky apparatus, and/or vacuum enclosures. By providing a compact, chip-scale platform that enables sub-cycle, field-sensitive detection of sub- to few-fJ optical waveforms in ambient conditions, devices similar to those discussed in this work could find applications such as phase-resolved spectroscopy and imaging, and could have an impact in a variety of fields such as biology, medicine, food-safety, gas sensing, and drug discovery. In particular, due to their compact footprint and pJ-level energy requirements, such detectors could be used to enhance the performance and operating bandwidth of frequency comb spectroscopy systems. Further development of the devices and detection scheme, such as spatially-resolved measurements, arbitrary polarization detection, as well as improvements to the photocurrent detection chain are the subject of ongoing research. We believe that on-chip petahertz field-sampling devices will enable many fundamental scientific investigations such as the time-domain characterization of attosecond electron dynamics and optical-field-driven nonlinear phenomena in light-matter interactions.

3.3 Methods

3.3.1 Experimental Methods

The nanodevices were illuminated by a few-cycle, supercontinuum-based [89], CEP-stablilized fiber laser source [90]. The source has a central wavelength of ∼1170 nm, with a pulse duration of ∼10 fs FWHM (∼2.5 cycles), and repetition rate of 78 MHz. The supercontinuum was gen-

erated from a highly non-linear gemanosilicate fiber pumped by a Er:fiber-based laser oscillator and Er-doped fiber amplifier (EDFA) system and compressed with a SF10 prism compressor. The CEP was locked to a fixed CEP value for all measurements taken. Pulse characterization of the laser source was performed by two-dimensional spectral shearing interferometry (2DSI) measurements [91] and can be found in Supplementary Information Sec. 3.4.2. The spectrum of the laser source was measured with a fiber-coupled optical spectrum analyzer (Ando Electric Co., Ltd.). More details about the supercontinuum source can be found in Ref. [90].

A dispersion-balanced Mach-Zehnder interferometer was used to generate the pulse pairs for the experiment. An Inconel reflective neutral density (ND) filter of optical density (OD) 4 on a 2 mm thick BK7 substrate (Thorlabs) was placed in one arm and used to generate a weak signal pulse with pulse energy of $\sim$5 fJ. An optical chopper was placed in this weak arm for lock-in detection and amplification. The strong, driver arm had a pulse energy of $\sim$50 pJ. A corresponding 2 mm thick BK7 window was placed in the driver arm to balance the dispersion between arms. The added chirp from the glass was precompensated using the prism compressor. The delay between the two pulses was controlled with a home built 15 μm piezo stage. The signal and driver arms were verified to be collinear using the second harmonic generation from a β-barium borate (BBO) crystal placed at the interaction region and optimizing the contrast of the interferrometric autocorrelation. A chopper was placed in the weak arm to modulate the signal for lock-in amplification. A schematic of experimental setup can be found in Supplementary Information Fig. 3.4.1.

The pulses were focused onto the chip using a Cassegrain reflector to a spot-size of 2.25 µm by 4.1 µm FWHM. This spot-size allowed for illumination of 10-15 nanoantennas at a time. The polarization of the pulses was parallel to the nanoantenna height axis (Fig. 1A). A bias voltage of 3 V was applied across the 50 nm device gap to enhance its photoemission response and accentuate its rectified behavior [92]. The emitted current was collected and amplified by a transimpedance amplifier (FEMTO Messtechnik GmbH) in conjunction with a lock-in amplifier (Stanford Research Systems), with a modulation of 200 Hz of the optical chopper.

For each data set, 60 scans of 10 second acquisition time over the 100 fs time window were performed. Post-processing was done in Matlab. Each data set was Fourier transformed and windowed from 150 THz to 350 THz with a tukey-window steepness of $\alpha = 0.2$. The resulting output was averaged in the time-domain.

3.3.2 Device Fabrication

[2] We used a fabrication process based on that described in Ref. [23]. The data presented in this work comes from devices fabricated on two different chips. The devices were fabricated on BK7 substrates. The patterning was performed using an electron beam lithography process

[2]The devices were fabricated at the MIT cleanroom facilities by Marco Turchetti.

with PMMA A2 resist (Microchem), a writing current of 2 nA, a dose of 5000 μC cm^{-2}, and an electron beam energy of 125 keB. To avoid charging, an Electra92 layer was spin-coated on top of the PMMA at 2 krpm and baked for 2 min at 90 °C. Since these are large arrays, a proximity effect correction step was also included when designing the layout. After exposure, the resist was cold-developed in a 3:1 isopropyl alcohol to methyl isobutyl ketone solution for 60 s at 0 °C. Then, a 2 nm adhesion layer followed by 20 nm of Au were deposited using electron beam evaporation. An adhesion layer of Ti was used for the 240 nm and Cr for the 200 nm antennas chips. Subsequently a liftoff process in a 65 °C bath of n-methylpyrrolidone (NMP) (Microchem) was used to release the structures. Finally, we used a photolithography procedure to fabricate the contact pads for external electrical connections.

3.3.3 Electromagnetic Simulations

[3] The optical response of the plasmonic nanoantennas was simulated in a finite-element-method electromagnetic solver (COMSOL Multiphysics). The nanoantenna geometry was extracted from SEM images. The refractive index of gold was taken from Ref. [93], and the refractive index of the glass substrate was fixed at 1.5 with negligible dispersion in the simulation spectral range. To simulate nanoantenna arrays, periodic boundary conditions were used. The normally incident plane wave was polarized along the nanotriangle axis (perpendicular to the nanowire). Perfectly matched layers were used to avoid spurious reflections at the simulation domain boundaries. The complex field response $\tilde{H}_{\mathrm{Pl.}}(\omega) = \tilde{E}^{(L)}(\omega)/\tilde{E}(\omega)$ was evaluated as a function of frequency. The field enhancement was defined as the ratio of the near-field at the nanotriangle tip to the incident optical field.

3.4 Supplementary Materials

3.4.1 Experimental Setup

A CEP-stable, 78 MHz Er:fiber-based supercontinuum laser source was used, with a central wavelength of ∼1170 nm and pulse duration of ∼10 fs FWHM. A dispersion-balanced Mach-Zehnder interferometer was used to generate the pulse pairs for the experiment (Fig. 3.5). An Inconel reflective neutral density (ND) filter of optical density (OD) 4 on a 2 mm thick BK7 substrate (Thorlabs) was placed in one arm and used to generate a weak signal pulse with pulse energy of ∼5 fJ. An optical chopper was placed in this weak arm for lock-in amplification and detection. The strong, driver arm had a pulse energy of ∼50 pJ. A corresponding 2 mm thick BK7 window was placed in the driver arm to balance the dispersion between arms. The added chirp from the glass was precompensated using the prism compressor. The delay between the two pulses was controlled with a home built 15 µm piezo stage. The generated electron emission

[3] The electromagnetic simulation of our devices were done by Dario Cattozzo Mor.

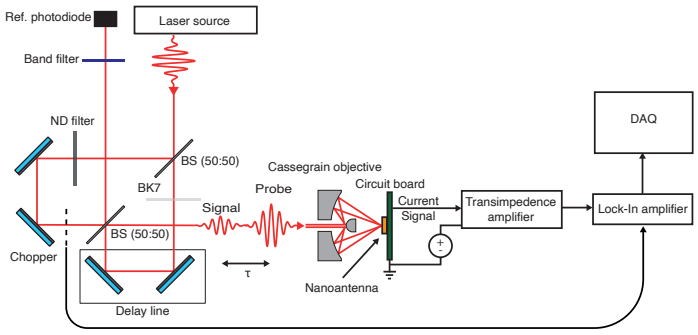

Figure 3.5: **Experimental Setup** Overview of the optical layout and signal detection chain of our experiments. Abbreviations: BS: beamsplitter, ND: neutral density filter, DAQ: data acquisition.

is collected and amplified by a transimpedance amplifier (FEMTO Messtechnik GmbH). The resulting voltage signal is demodulated by the Lock-In amplifier with the 200 Hz frequency of the chopper wheel and subsequently low-pass filtered.

3.4.2 Source Spectral Phase Measurements

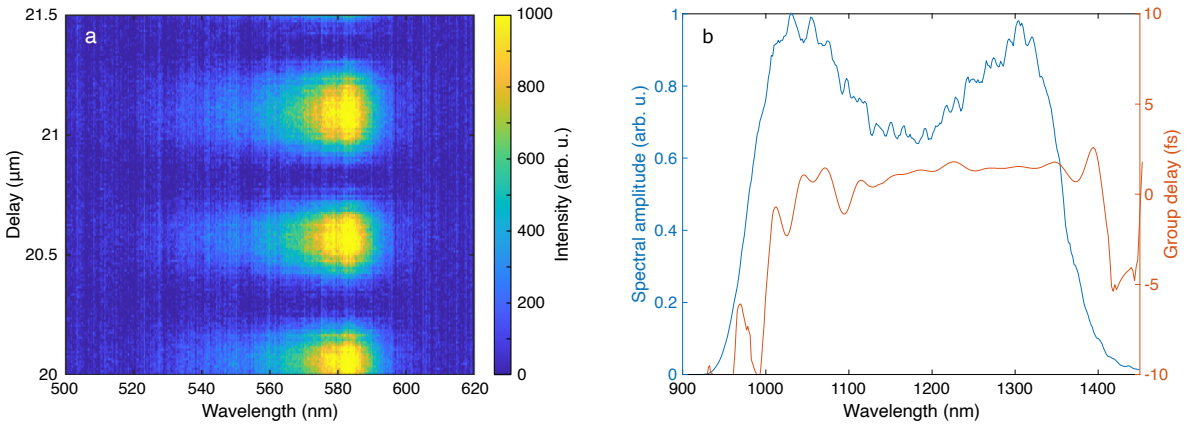

Figure 3.6: **Source spectral phase characterization using 2DSI. a,** Raw 2DSI spectrogram of the source in the experiment conditions. **b,** Retrieved group delay (red) and laser spectrum (blue). The optimized values of shear frequency and upconversion wavelength are $f_{\text{shear}} = 5.5$ THz and $\lambda_{\text{up}} = 1050$ nm.

In order to characterize the spectral phase of our supercontinuum source we performed two-dimensional spectral shearing interferometry (2DSI) measurements [91]. Two spectrograms were obtained for the measurement: the first with the laser in similar conditions to that of the experiment, and the second with an added 1.5 mm fused silica window placed in the beam path. The spectrogram of the source in the experimental conditions is shown in Fig. 3.6a. The second spectrogram taken with an additional propagation through 1.5 mm fused silica was used to calibrate the shear frequency f_{shear} and upconversion wavelength λ_{up} needed for group delay retrieval from the 2DSI measurement. Using an optimization routine, we found the values for f_{shear} and λ_{up} that resulted in the minimum error between the group delay difference measured with and without the fused silica using 2DSI and that predicted using the known optical properties of fused silica. The resulting retrieved group delay and the spectrum of our laser source are reported in Fig. 3.6b.

3.4.3 Effect of fabrication tolerances

The effects of fabrication tolerances on the antenna resonance were investigated via numerical simulation as well as experimentally (for similar devices) in Ref. [23]. The main effects affecting the resonance are: the wire position within the antenna; the tip radius of curvature; the height of the nanoantenna. However, we image the devices before taking measurements so that these effects are taken into account during our simulations investigating resonance for our specific device design.

3.4.3.1 The Wire Position

The fabrication process can cause a small variation ($\pm$5% with respect to the expected position) in the connecting wire position in the triangular nanoantenna which in turn causes a $\pm$ 30 nm shift in wavelength for the maximum field enhancement value. In particular, a connection wire closer to the antenna tip leads to a shift towards higher frequencies and vice versa. However, the device is imaged before testing, therefore this error is taken into account in our simulations. Only a residual ±5nm variation exists within the different fabricated antennas in the array due to fabrication variability (e.g. uneven exposure due to beam current fluctuation), which can only cause much smaller shifts in the resonance.

3.4.3.2 The Tip Radius of Curvature

Fabrication variability can also account for a $\pm$ 3 nm variation in the radius of curvature throughout the array. This can lead to a 1.3-1.5 fold reduction or increase in the field enhancement and a $\mp$ 20 nm resonance shift.

3.4.3.3 The Height of the Nanoantenna

Similarly to the wire position, the nanoantenna height can also have a variation of approximately $\pm$5% with respect to the expected height specified in the layout that can result approximately in a $\pm$ 70 nm shift in the resonance. However, as for all other dimensions mentioned above, this can be taken into account in the model by imaging the array before the experiment. This leaves a residual $\pm$ 5 nm fluctuation within the array due to fabrication.

3.4.4 Effect of Experimental Variability

We also used simulations to investigate some effects that can alter the antenna response due to the modifications induced by the experiment or the variability of the experimental setup itself. Specifically, we investigated the effect of the laser induced reshaping and sample tilting on an antenna geometry of the same shape as in the experiment having a nominal resonance around $\approx$1100 nm .

3.4.5 Laser-Induced Reshaping

The laser-induced reshaping consists mainly in shrinkage of the portion of antenna that protrudes from the connecting wire towards the ”rectifying” wire (i.e. the tip of the device). This shrinkage effectively results in a slight change in the effective radius of curvature, and increase in the gap width. Some shape transformation can also seen in the rest of the device (triangles and wires). This can be seen in Ref. [23], where similar devices are systematically studied with post-imaging of the devices after illumination.

This process can be simulated by keeping the points where the triangle meets the connecting wire fixed and by making the triangle vertex position closer to the connecting wire. The tip length is decreased in the following range: [-5 nm, -20 nm], with steps of 2.5 nm. The impact of this shrinkage on the field enhancement spectrum of the antenna is shown in Fig. 3.7. The main field enhancement peak shifts to higher frequencies for shorter tips (larger gaps), with an approximately $\sim$ 20 nm shift per each 2.5 nm step.

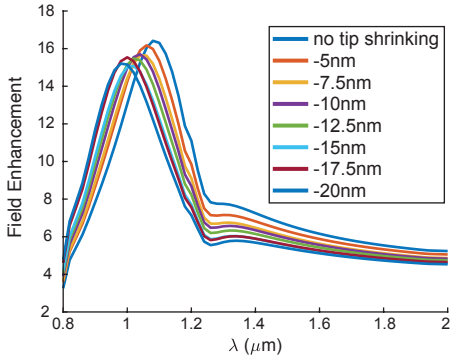

Figure 3.7: **Effect of laser-induced reshaping.** Field enhancement as a function of wavelength for an antenna resonant at $\approx$1100 nm for different amounts of tip shrinkage.

3.4.6 Spatial Overlap and Sample Tilting

There is some sensitivity with respect to imperfect spatial overlap or incident beam tilt. An imperfect spatial overlap would cause a reduced signal to noise ratio that is directly proportional to the amount of overlap between the signal and driving pulses due to the linear response of the device. However, as the response is a linear replica of the signal everywhere, it would not

obscure the response so long as the two beams are sufficiently collinear such that the relative delay does not change significantly over the driving beam spot.

If both the signal and driving pulses are tilted with respect to the device, a small shifting and decrease of the field enhancement occurs (see simulations in Fig. 3.8). If there is tilt between the signal and driving pulse, a geometric temporal smearing will occur.

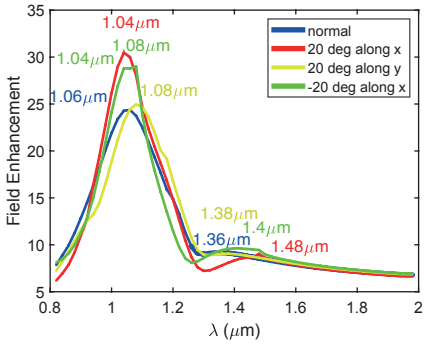

Figure 3.8: **Effect of sample tilting.** Field enhancement as a function of wavelength for a 20° tilt along the x and y axes, with x being the axis parallel to the tip direction and y the axis parallel to the wire direction.

3.4.7 Retrieved Incident-Field from Measured Data

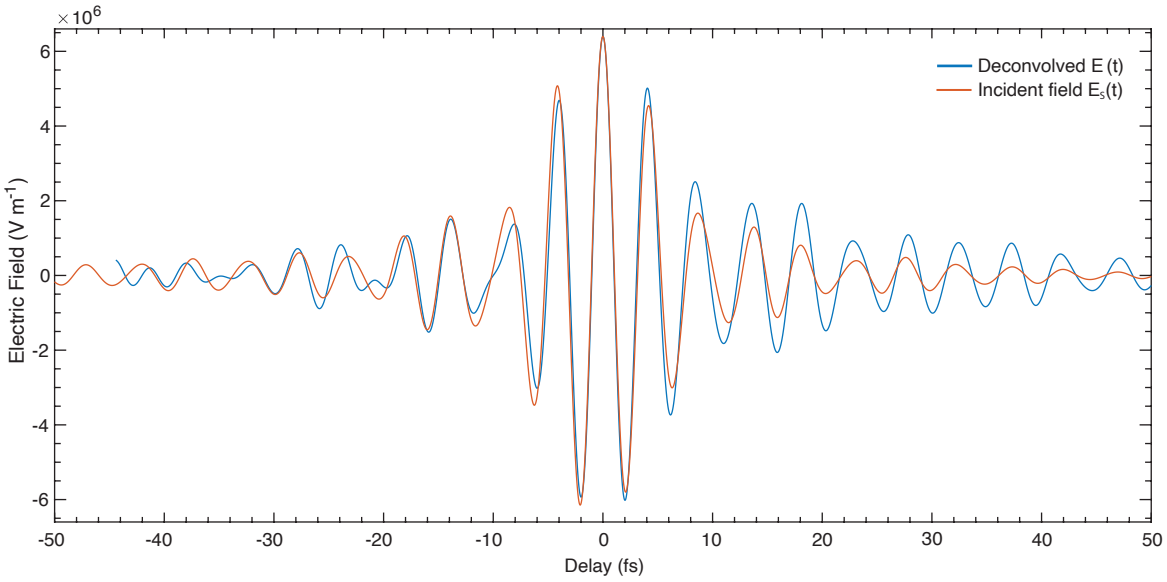

Figure 3.9: **Deconvolution of measured data with the simulated antenna impulse response.** The measured data is deconvolved with the simulated antenna transfer function of a 240 nm sized device and the scaled to the calculated field strength $6.4 \cdot 10^6$ V m^{-1} (blue) and compared to the calculated incident electric field (orange).

With the presented field sampling technique, the local electric field at the antenna tip $E^{(L)}(t)$ is measured. To retrieve the incident electric field $E(t)$ the local field $E^{(L)}(t)$ was deconvolved with the antenna transfer function $E(t) = \mathscr{F}^{-1}\left(\frac{\tilde{E}^{(\mathrm{L})}(\omega)}{\tilde{H}_{\mathrm{Pl.}}(\omega)}\right)$. The resulting deconvoluted electric field of the measured data with the antenna transfer function is shown in Fig. 3.9 in blue. For comparison, the calculated incident electric field is shown in red.

3.4.8 Dependence of Average Photocurrent on Pulse Energy

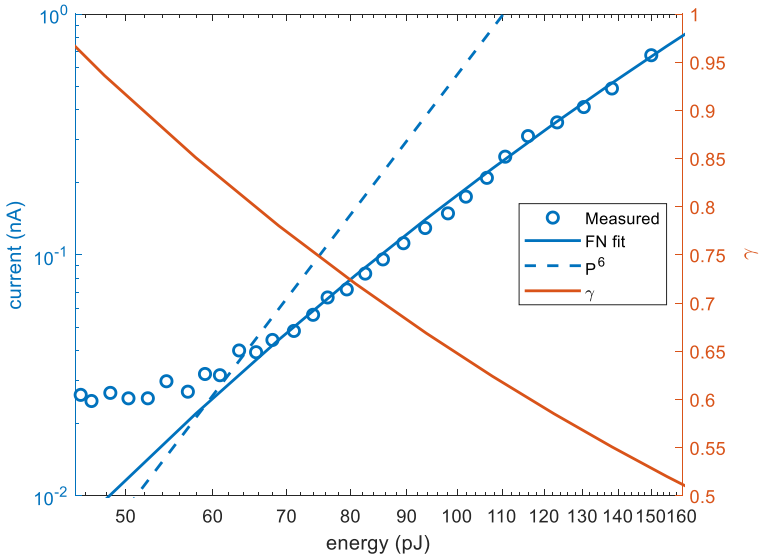

Figure 3.10: **Measurement of average photocurrent as a function of incident pulse energy**. These measurements were performed on a nominally similar set of 240 nm devices to those used for optical field sampling in the manuscript. A Fowler-Nordheim fit (solid line) is shown indicating emission that scales approximately as $I \propto P^{3.5}$ over the measured pulse energy range. For reference, the dashed line shows $I \propto P^6$ which is similar to the observed multiphoton power-law scaling rate from similar structures characterized in [9]. The Keldysh parameter γ (red line) is also calculated in the same energy range.

Studies of the average photocurrent were performed to verify the operating regime of the devices. Fig. 3.10 shows results from a set of 240 nm devices similar to those used in the main text. We note that this scan was not performed on the exact set of devices used for optical field sampling measurements as to avoid device reshaping at the highest intensities (see Sec. **??**). To further reduce the exposure time of the devices to ensure an accurate scaling rate measurement, we reduced the amount of averaging per data point. This results in an electronic noise floor a bit higher than in the manuscript, appearing below values of ≈60 pJ. The results indicate a photocurrent power-law scaling of $I \propto P^{\sim 3.5}$, where P is the incident pulse energy. Multiple scans were performed showing power-law scaling rates ranging from $I \propto P^3$ to $I \propto P^4$ over the measured range of pulse energies. The experimental results fit very well to a quasi-static Fowler-Nordheim photoemission model which is shown as the solid blue curve in Fig. 3.10 assuming a field-enhancement of ≈ 20 in the time domain. This field enhancement is an excellent match to that predicted by our electromagnetic models (time-domain field-enhancement of 20.16 given our incident pulses). For comparison, in Fig. 3.10, we also show a power-law scaling reference line for $I_{\mathrm{MP}} \propto P^6$ which is comparable to the experimentally observed multiphoton scaling rate from similar devices in prior work with similar material and resonance properties [9]. We also used the peak field from the quasi-static Fowler-Nordheim fit to calculate the expected Keldysh parameter γ, finding that $\gamma < 1$ over the entire range of intensities as would be expected for

optical-field tunneling. Importantly, we find that $\gamma \approx 0.9$ at 50 pJ which was the operating point of the driving field used for the sampling measurements in the text.

3.4.9 Discussion of Sampling Bandwidth

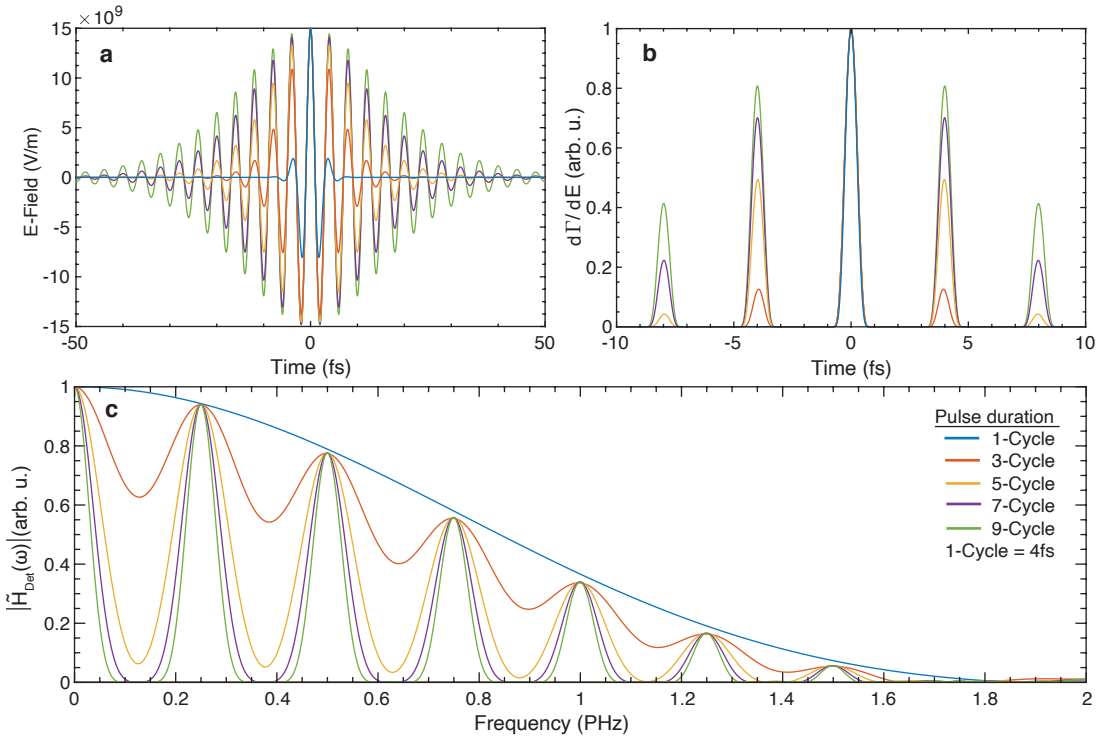

Figure 3.11: **Sampling bandwidth as a function of pulse duration.** **a,** Electric-field transients for near-infrared pulses with a FWHM duration of 1-, 3-, 5-, 7-, and 9-cycles and a central frequency of 250 THz. **b,** Calculation of $\frac{\mathrm{d}\Gamma}{\mathrm{d}E}\big|_{E_\mathrm{D}(t)}$ for the field transients shown in (A) and assuming $F_t = 78.7$ V nm^{-1} as the characteristic tunneling field. **c,** Fourier transform of $\frac{\mathrm{d}\Gamma}{\mathrm{d}E}\big|_{E_\mathrm{D}(t)}$ showing the accessible sampling bandwidth provided by the field transients shown in **a**.

A strong local electric-field transient (driver) drives the electron emission at the metallic nanoantenna [8–10, 83]. For simplicity in this section we will be discussing the field driving the emission at a surface, $E_\mathrm{D}(t)$. When a weak electric-field waveform (signal) perturbs the emission process, the detected time-averaged current is proportional to the electric field of the small signal. The small-signal gain, as defined by $\frac{\mathrm{d}\Gamma}{\mathrm{d}E}\big|_{E_\mathrm{D}(t)}$, is therefore dictated by the strong driving electric field waveform. To demonstrate the influence of the FWHM of the driving pulse duration on the sampling bandwidth, we calculated $\tilde{H}_\mathrm{Det}(\omega)$ for 1-, 3-, 5-, 7-, and 9-cycle sech^2 driver pulses each with a central frequency of 250 THz and a peak field strength at the antenna surface of 15 GV m^{-1} (see Fig. 3.11a).

The small-signal gain $\frac{\mathrm{d}\Gamma}{\mathrm{d}E}\big|_{E_\mathrm{D}(t)}$ was calculated by assuming Fowler-Nordheim tunneling emission with a characteristic tunneling field of $F_t = 78.7$ V nm^{-1}. Fig. 3.11b shows the effective gate signal $\frac{\mathrm{d}\Gamma}{\mathrm{d}E}\big|_{E_\mathrm{D}(t)}$ for the sampling process for each pulse duration. Only the single-cycle pulse (blue) exhibits an isolated peak. However, for driver pulses with an increasing number of cycles, satellite pulses start to emerge. For the 9-cycle case (green traces) the height of satellite pulses at -4 fs and 4 fs approach the height of the center peak. Fig. 3.11c shows the Fourier

transform of $\frac{d\Gamma}{dE}\big|_{E_D(t)}$.

The sampling bandwidth generated by a single-cycle field transient (Fig. 2C, blue curve) shows a smooth response from DC to 1.8 PHz and corresponds to the Fourier transform of the isolated peak in Fig. 3.11b (blue trace). With increasing pulse duration, the bandwidth becomes increasingly modulated due to the destructive interference of the additional peaks in the gate signal. The modulation is periodic with the frequency f_0 of the driving electric field at 250 THz and exhibits maxima at the higher harmonics $n \cdot f_0$ for $n \, \varepsilon \, \mathbb{N}$. We highlight that although a 5-cycle driver waveform results in strong modulation of the sampling response $\tilde{H}_{\mathrm{Det}}(\omega)$, the sampling response does not completely vanish at the minima (yellow traces). However, for driver pulses having a FWHM duration greater than five cycles, we find that the sampling response completely vanishes at the minima. This sampling technique allows for detection of higher harmonics of the driving signal regardless of the pulse duration, which originates from the fact that the individual peaks are deeply sub-cycle in duration [83].

3.4.10 Carrier-Envelope Phase Discussion

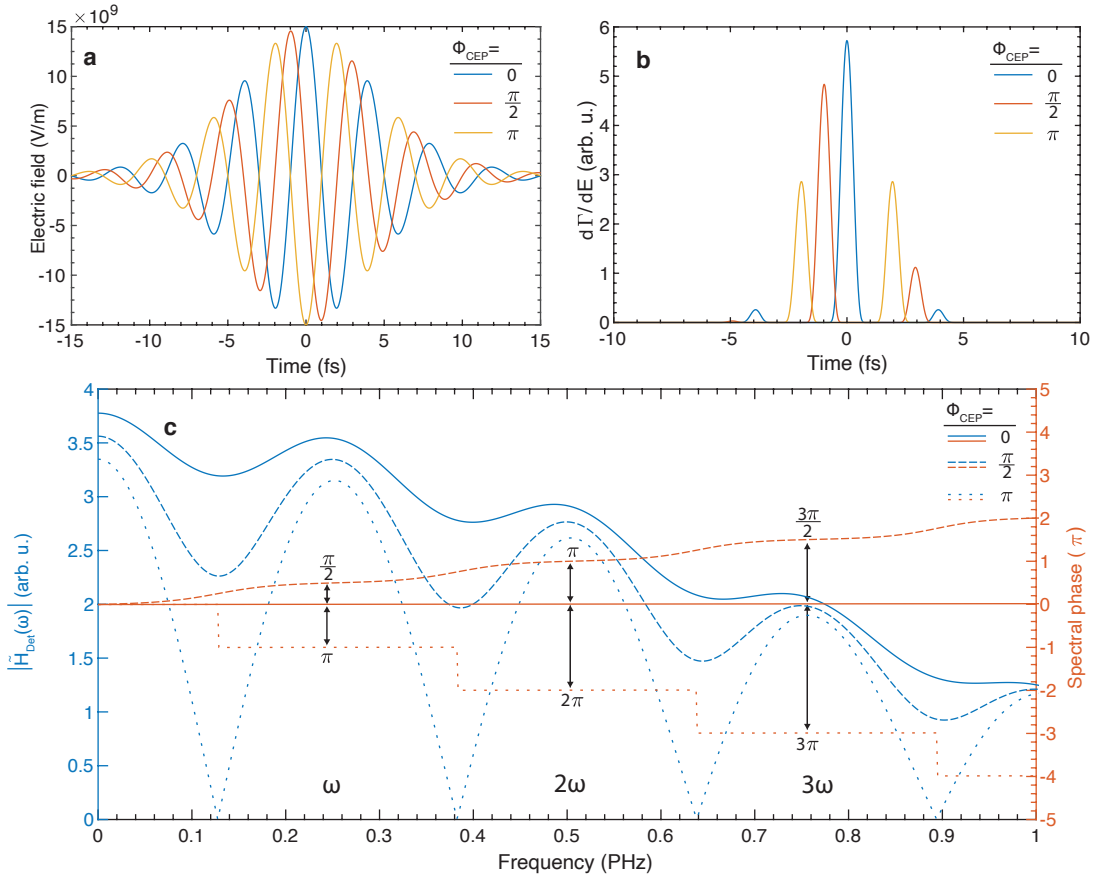

Figure 3.12: **Sampling response as a function of CEP. a,** Calculated sech^2 pulse centered at 250 THz with a pulse duration of 10 fs (2.5 cycles), a peak electric field of 15 GV m^{-1}, and a $\Phi_{\mathrm{CEP}} = 0,\ \frac{\pi}{2},\ \pi$. **b,** The small signal gain $\frac{\mathrm{d}\Gamma}{\mathrm{d}E}\big|_{E_{\mathrm{D}}(t)}$ is calculated by assuming Fowler-Nordheim tunneling emission with a characteristic tunneling field of $F_t = 78.7$ V nm^{-1}. The electric-field transients used here correspond to **a**. **c,** The spectral amplitude and phase of the complex sampling response of $\tilde{H}_{\mathrm{Det}}(\omega)$ as a function of frequency. Calculated for $\Phi_{\mathrm{CEP}} = 0,\ \frac{\pi}{2}, \pi$.

The carrier-envelope phase (CEP) of a few-cycle pulse plays a significant role in strong-field physics and heavily influences the electron emission characteristics from resonant nanoantenna devices. In this section we discuss the role of the driving waveform's CEP in the sampling process. For simplicity in this section we will be discussing the field driving the emission at a surface, $E_{\mathrm{D}}(t)$.

For our analysis, we calculated the complex sampling response $\tilde{H}_{\mathrm{Det}}(\omega)$ assuming a sech^2 driving pulse with a central frequency of 250 THz and a pulse duration of 10 fs ($\sim$2.5 cycle), as given by the output of the laser used to experimentally verify device performance. As in Sec. S1, the incident electric field was taken to be 15 GV m^{-1}. The results are plotted in Fig. 3.12a for various CEP values of the driving pulse. The small signal gain $\frac{\mathrm{d}\Gamma}{\mathrm{d}E}\big|_{E_{\mathrm{D}}(t)}$ was calculated by assuming Fowler-Nordheim tunnel emission with a characteristic tunneling field of

$F_t = 78.7$ V nm^{-1} and is plotted in Fig. 3.12b. In Fig. 3.12c the complex sampling response $\tilde{H}_{\mathrm{Det}}(\omega)$ derived from $\frac{\mathrm{d}\Gamma}{\mathrm{d}E}\big|_{E_{\mathrm{D}}(t)}$ is shown.

The CEP, Φ_{CEP}, of the driving pulse dictates the amplitude of the modulation of $\tilde{H}_{\mathrm{Det}}(\omega)$. For the driver pulse duration modeled in Fig. 3.12a, a cosine shaped pulse ($\Phi_{\mathrm{CEP}} = 0$) exhibits minimal modulation of the sampling bandwidth, which corresponds to an isolated electron burst with small satellites in the time-domain if the pulse is sufficiently short (see Fig. 3.12b). A CEP of $\Phi_{\mathrm{CEP}} = \pi$ corresponds to a negative cosine shaped pulse, which corresponds to two electron bursts of equal height, resulting in the sharp minima in the sampling bandwidth as shown in Fig. 3.12c (dotted traces). More importantly, with an adequately short driving pulse, it is possible to choose an appropriate Φ_{CEP} value such that only one electron burst dominates the field emission process, resulting in a smooth, unmodulated $\tilde{H}_{\mathrm{Det}}(\omega)$ from DC to 1 PHz, as shown in Fig. 3.11c. Nevertheless, independently of Φ_{CEP} a full octave of spectrum can still be sampled with distortion due to $\tilde{H}_{\mathrm{Det}}$.

Another important characteristic of the sampling process to consider is the absolute phase of the sampled output. When $\Phi_{\mathrm{CEP}} = 0$, a dominant electron burst exists in the time domain and the absolute phase of the signal pulse will be transferred to the sampled output, as $\tilde{H}_{\mathrm{Det}}(\omega)$ will be a purely real function (see Fig. 3.12c). For comparison, if $\Phi_{\mathrm{CEP}} \neq 0$ the spectral phase of $\tilde{H}_{\mathrm{Det}}(\omega)$ is not flat. As shown in Fig. 3.12, this phase resembles a stair function with plateaus of flat phase around the central frequency ω_0 and its harmonics. Looking closely at Fig. 3.12, we see that we can write the spectral phase at the nth harmonic as $\angle\tilde{H}_{\mathrm{Det}}(n\omega) = n \cdot \Phi_{\mathrm{CEP}}$ for $n \,\varepsilon\, \mathbb{N}$. With these spectral phase behaviors, we then see that the constant phase component of the sampled output becomes the difference between that of the sampling pulse, $n \cdot \Phi_{\mathrm{CEP}}$, and that of the signal, Φ_{S}. Therefore, the constant, or absolute, phase of the sampled output can be written $\Phi_{\mathrm{S}} - n \cdot \Phi_{\mathrm{CEP}}$. In the case where the driving pulse, E_{D}, and the signal pulse, E_{S}, originate from the same laser source, they will share a common Φ_{CEP}, and in this case, the absolute phase of the sampled pulse will therefore be zero. Importantly, we should note that this result is independent of Φ_{CEP}, and even laser sources with a carrier envelope offset $f_{\mathrm{CEO}} \neq 0$ can be used for sampling. Lastly, we should additionally note that in stark contrast to other phase-sensitive techniques, like homo- and hetero-dyne detection, the absolute phase of E_{D} can be derived unambiguously *in situ* from the field emission current generated by E_{D} in our devices, as demonstrated in [8, 23].

3.4.11 Field-Sampling Measurements with 200 nm Devices

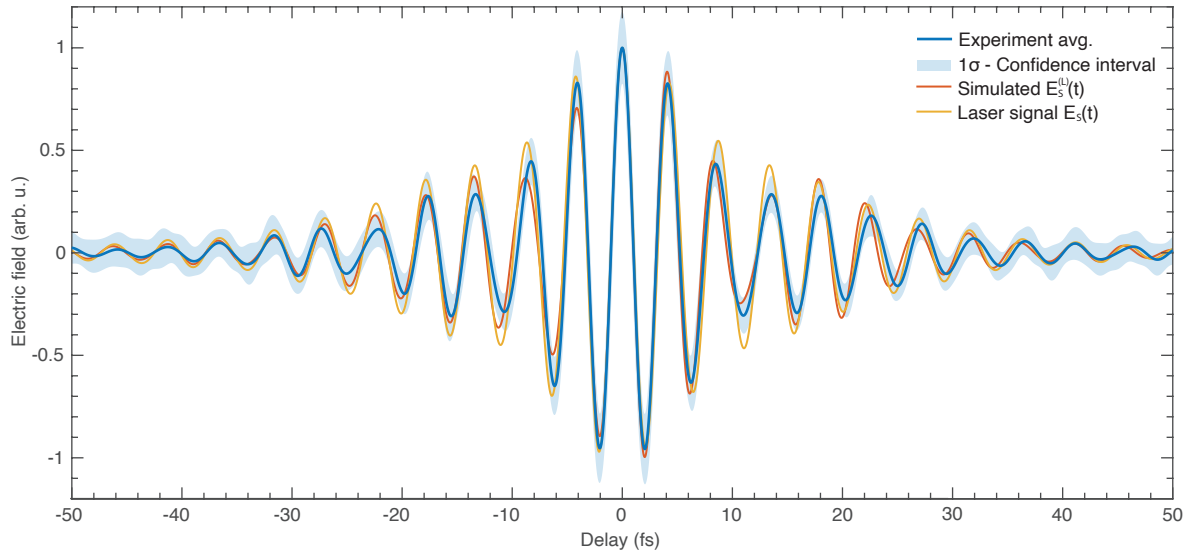

Figure 3.13: **Experimental field sampling results using 200 nm devices.** Time-domain results for 200 nm devices comparing measured (blue) and simulated near-fields ($E_{\mathrm{S}}^{(\mathrm{L})}(t)$, red) to the calculated incident laser signal ($E_{\mathrm{S}}(t)$, yellow). Here, negative delays indicate the driver pulse arrives before the signal pulse. The 200 nm device is designed to be off-resonant with the laser pulse and the measured trace yields good agreement to the calculated laser output. The 1σ-confidence interval is shown as a blue shaded ribbon centered at the average value (blue solid line) retrieved from 47 scans.

Our technique was also tested using devices consisting of triangular antennas with a 200 nm height. These devices were designed to be off-resonant with the laser pulse and were fabricated on a separate chip from the 240 nm antenna. Fig. 3.13 presents the acquired cross-correlation trace (blue) for these devices. For each data set, 47 scans of 5 seconds acquisition time over the 100 fs time window were performed. Post-processing was done in Matlab. Each data set was Fourier transformed and windowed from 150 THz to 350 THz with a tukey-window (steepness of $\alpha = 0.2$). The resulting output was averaged in the time-domain.

We find good agreement between the measured trace (blue) to the simulated local signal field, $E_{\mathrm{S}}^{(\mathrm{L})}(t)$ (red). We note that both the measurement and simulated local signal fields are both slightly shorter than the calculated laser output (yellow). The reason for this is apparent when examining the pulses in the frequency domain as shown in Fig. 3.14. While the main spectral peak at ≈ 220 THz agrees with the measured laser spectrum ($\tilde{E}_{\mathrm{S}}(\omega)$, gray dotted curve) and the expected antenna response ($\tilde{E}_{\mathrm{S}}^{(\mathrm{L})}(\omega)$, light blue dashed curve), both the simulated and experimental local signal field spectra exhibit an enhanced shoulder out to 300 THz relative to the measured laser output spectrum (solid blue curve). This is due to the plasmonic resonance which enhances these higher frequency components, resulting in a shorter time domain response of the local fields relative to the incident fields after interaction with the antenna.

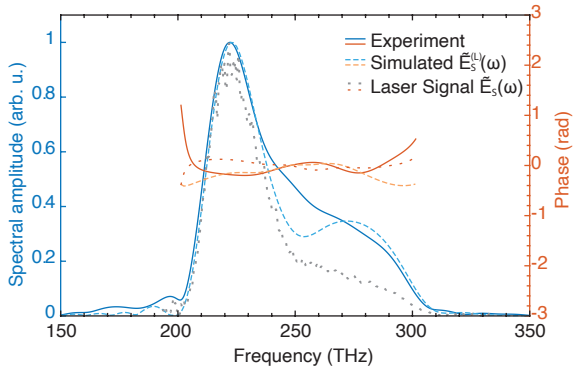

Figure 3.14: **Frequency-domain analysis of 200 nm device results.** Frequency-domain analysis comparing measured (solid) and simulated ($\tilde{E}_S^{(L)}(\omega)$, dashed) near-fields for 200 nm devices to the calculated incident laser signal ($\tilde{E}_S(\omega)$, dotted). The 200 nm device is designed to be off-resonant with the laser pulse, thus the measured and simulated spectrum only show a single spectral peak corresponding with that of the laser spectrum at $\approx$ 220 THz.

3.4.12 Data Processing and Error Analysis

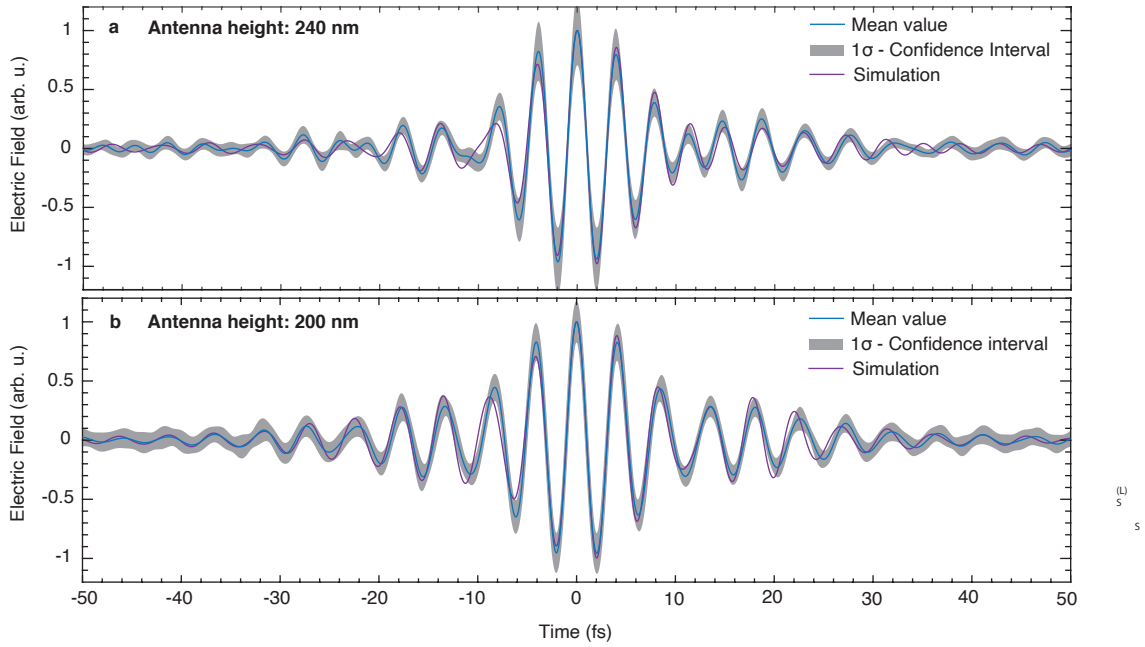

Figure 3.15: **Mean value and 1σ-confidence interval** Time-domain measurement and simulation for **a** 240 nm devices (Fig. 3, main text), and **b** 200 nm devices (Fig. 3.13). The blue curves shows the mean value for every electric field/time coordinate over all individual scans. The grey ribbon shows the 1σ-confidence interval for the respective coordinate. For comparison, the simulated electric field is shown in purple.

To determine the error in our measurement, we took the Fourier transform of the each of the $\sim$50 individual data sets and applied a tukey-window in the frequency-domain with a steepness of $\alpha = 0.2$ from 150 THz to 350 THz. The windowed data sets were then back transformed into the time-domain and averaged for each time coordinate over all data sets. To determine the 1σ-confidence interval the standard deviation was calculated for each time coordinate over all data sets. The result is shown in Fig. 3.15 and compared to the respective simulation shown in Fig. 3 (main text) for the 240 nm devices and Fig. 3.13 for the 200 nm devices.

4 Tailoring the Impulse Response of Petahertz Optical Field-Sampling Devices

In the previous Chapter 3 , optical field-sampling with attosecond resolution was experimentally demonstrated [20]. The sampling technique is based on attosecond fast electron emission from plasmonic nanoantennas and was shown to have a potential bandwidth of up to one petahertz with sensitivities of $< 1\,\mathrm{MV\,m^{-1}}$. This corresponds to measuring few-cycle pulses with only femtojoules of energy. Aside from nanoantenna-based sampling, many other approaches, predominantly based on the ionization of air [16, 17, 19] and in solids [15], have been explored. Interestingly, all these techniques share the commonality that a strong pulse is generating a short sub-cycle ionization gate, that is used to probe a secondary electric field. Unlike the common technique of attosecond streaking, the kinetic energy of electrons is not measured, but the total ionization yield instead. This allows reducing the complexity of the experimental setup, as no such thing as a time-of-flight spectrometer or similar is necessary, and in addition allows for in-air operation. To understand fundamental principles of this field sampling approach, the nanoantenna based sampling is used as a conduit to extract fundamental insights into this technique. As will be explained in this chapter, the antenna-based sampling platform has a high degree of flexibility with respect to its impulse response function, which is defined by the driving waveform and the antenna symmetry properties. With this, the connection of specific antenna devices to the air-based ionization scheme is made.

The previous chapter shows that the measured electric field is the cross-correlation between the first derivative of the emission function $\Gamma(E)$ evaluated at the driving electric field $E_\mathrm{D}(t)$ and the weak signal field $E_\mathrm{S}(t)$,

$$I(\tau) \propto \int_{-\frac{T_\mathrm{Rep.}}{2}}^{\frac{T_\mathrm{Rep.}}{2}} \left(\Gamma\big(E_\mathrm{D}(t-\tau)\big) + \left.\frac{\mathrm{d}\Gamma}{\mathrm{d}E}\right|_{E_\mathrm{D}(t-\tau)} \cdot E_\mathrm{S}(t) + \mathrm{O}(E_\mathrm{S}^2(t)) \right) dt, \tag{4.1}$$

with $I(\tau)$ denoting the current measured as a function of delay τ and error $\mathrm{O}(E_\mathrm{S}^2(t))$. This shows that the defining term for the sampling process is the cross-correlation term between the signal $E_\mathrm{S}(t)$ and the first derivative $\frac{\mathrm{d}\Gamma}{\mathrm{d}E}\big|_{E_\mathrm{D}(t-\tau)}$, with the latter defining the impulse response of the method. The error $\mathrm{O}(E_\mathrm{S}^2(t))$ scales quadratically with the signal field strength and can cause distortion of the measured result. However, an algorithmic correction to this problem is proposed in Ref. [94]. The frequency domain of the sampling technique is written,

$$\tilde{I}(\omega) \propto \underbrace{\mathscr{F}\left(\left.\frac{\mathrm{d}\Gamma}{\mathrm{d}E}\right|_{E_\mathrm{D}(t)} \right)^*}_{:=\tilde{H}(\omega)} \cdot \tilde{E}_\mathrm{S}(\omega), \tag{4.2}$$

with $\tilde{H}(\omega)$, defining the gate frequency transfer function. In Chapter 3 Fig. 3.4 the transfer function $\left|\tilde{H}(\omega)\right|$ is shown for the experimental test case, but it is instructive to gain insight into the properties of this function, such as accessible bandwidth, modulation strength and fringe spacing and how those can be influenced.

Starting with the function Γ defining the electron emission rate, which is for this particular case defined in the quasi-static limit $\gamma \ll 1$ as the Fowler-Nordheim function[1] [63]. This function describes an electron emission rate that instantaneously follows the electric field, see Chap. 2 for details. The emission rate is defined as, $\Gamma(E) \propto E^2 \cdot e^{-\frac{f_{crit.}}{|E|}}$. $f_{crit.}$ denotes the critical field strength. Further, we define a square-wave function,

$$s(t) := \begin{cases} 1 & \text{if } \sin(\omega_0 t) \geq 0 \\ 0 & \text{otherwise} \end{cases}, \tag{4.3}$$

This function accounts for positive-sign half-cycles contributing to the emission, which is the case for emission at metal-vacuum boundaries. With an arbitrary Gaussian pulse as the driver $E_{\mathrm{D}}(t) = A(t) \cdot \sin(\omega_0 t)$, the influence of the envelope $A(t)$ and the carrier frequency ω_0 can be conceptually explored. Individual contributions shaping the sampling response function from the envelope and the carrier wave in the time and frequency domains are shown in Fig. 4.1. It should be noted that the separation holds strictly true only if $\Gamma'(E)$ is a multiplicative function, which is not the case for the Fowler-Nordheim function, but within reasonable approximation it is described with a polynomial function $\Gamma'(E) \approx E^n$ of suitable order n. This approximation yields a qualitatively instructive picture and helps in understanding the individual roles that contribute to the frequency response.

We begin by examining the influence of the carrier oscillation on the sampling response. The carrier wave alone results in a train of gate pulses with a flipping sign (Fig. 4.1 orange), while forming in the frequency domain a comb of narrowband lines at odd orders of the fundamental ω_0. The envelope contribution (Fig. 4.1 green) results in a broad Gaussian and is essentially a window function for the emission in time, that subsequently defines the in the frequency domain the baseband shape at $f = 0$. The function representing the rectification of the current $s(t)$ is a rectangular wave (Fig. 4.1 red), that results in a strong DC component in the frequency domain and the same odd higher harmonics at multiples of ω_0. The resulting frequency response is now approximately the convolution of the individual contributions, resulting in a broadband, but modulated, frequency response (Fig. 4.1 blue).

With that, one can see that the envelope of the pulse defines the width of the harmonics, and for the case of very short envelopes approaching a smooth continuous response, as also shown in Chapter 3 Fig. 3.11. The carrier frequency ω_0 defines the spacing of the harmonics. These two components define the frequency response throughout the entire bandwidth. However, a component neglected so far is the role of the nonlinearity. With increasing nonlinearity of the instantaneous current response, the time duration of the electron emission will become shorter in time. A higher nonlinearity therefore implies a broader frequency response of the sampling

[1] This analysis does not explicitly require the Fowler-Nordheim equation, but can be adapted to multiphoton ionization processes, that have the functional form $\Gamma(E) = E^{2n}$. The most important characteristic of the emission function is the strict field dependence, as purely intensity dependent emission has no sub-cycle characteristic.

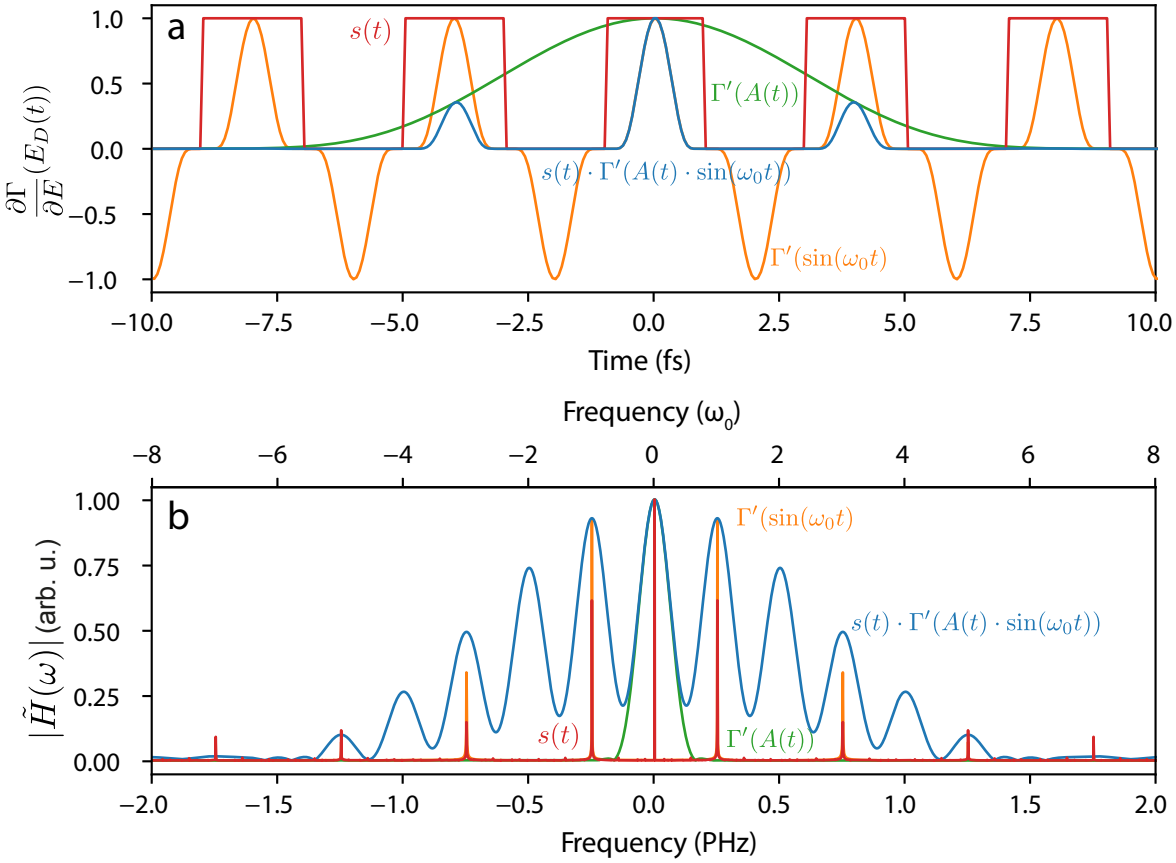

Figure 4.1: **Deconstruction of the Sampling Response:** (**a**) Time domain of the gate function showing the role of the carrier wave (orange), the envelope (green), and the rectification (red). (**b**) Frequency domain of the gate function showing the role of the carrier wave (orange), the envelope (green), and the rectification (red).

measurement. This can be seen, by just considering the envelope $A(t)$ and a multitphoton ionization process $A(t)^{2n-1}$ defined by a polynomial of order n. With increasing order n the shorter the nonlinear envelope and the broader the baseband of the frequency response will become. This analysis also implies to the individual half-cycle emission that will become increasingly shorter as well, broadening the overall frequency response, by creating more harmonics of the carrier wave. It should be noted, that with emission defined by the Fowler-Nordheim function $\propto E^2 \cdot e^{-\frac{f_{crit.}}{|E|}}$ that for high fields the function approaches $\propto E^2$. This significantly reduces the sampling response and would potentially reduce the accessible bandwidth.

Changing the frequency response by changing the driving laser pulse is in most cases not straightforward and is usually fixed after the laser source is built. However, an important benefit of the nanoantenna platform is the possibility of designing devices of almost arbitrary shape. This gives an interesting control pathway, which is the effective modification of the rectification function $s(t)$. A conceptual approach to this is to consider the rectifying antenna as a electronic diode that can be integrated in different ways into an electronic circuit. By using two diodes in parallel with opposing direction, one can create in total a point-symmetric current-voltage

curve. With this concept in mind three different antenna shapes with fundamentally different current-voltage response functions are defined, such as the rectifying antenna, the bow-tie antenna and the diamond-/rod-type antenna, see Fig. 4.2.

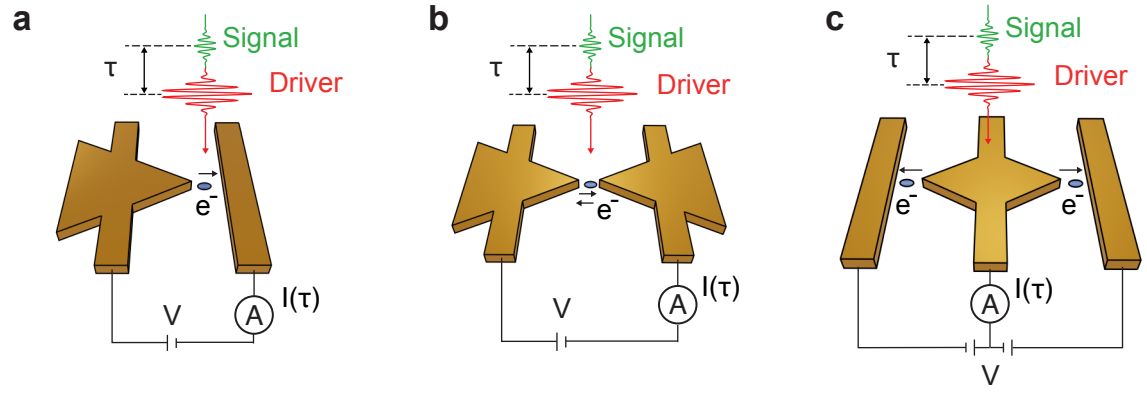

Figure 4.2: **Different Antenna Designs for Field Sampling:** (**a**) Fully rectifying antenna design, as demonstrated in Chapter 3. (**b**) Bow-tie antenna design as demonstrated for CEP measurement in Chapter 6 and Ref. [8, 10]. (**c**) Diamond-shaped antenna similar to Ref. [95]. V denotes a bias voltage; A a current meter; $I(\tau)$ the current measured as a function of delay τ.

The effective static response functions are shown in Fig. 4.3. These three types of devices exhibit essentially three fundamental symmetries with respect to the current flow at the device junction. The bow tie antenna has an inversion symmetry, a diamond-type antenna mirror symmetry, and a fully rectifying antenna asymmetry. To complete the previous analysis for the rectifying device, one can also state the appropriate function accounting for the current direction. In the bow-tie case, the Signum function $\mathrm{sgn}(E)$ is used, while in the symmetric case, the function is simply $s(t) = 1$. To calculate the frequency response of such devices, we use a single-cycle pulse of 4 fs duration and a center wavelength of 1.2 µm. The electric field of this pulse is shown for $\varphi_{\mathrm{CEP}} = 0,\ \pi/2,\ \pi$ in Fig. 4.4. Using a fixed local field strength of $20\,\mathrm{V\,nm^{-1}}$, close to what is used in Chap. 3, and the field $E(t)$ with varying CEP, an exemplary sampling gate is generated. The instantaneous current $\Gamma(E(t))$ and the corresponding frequency response $\left|\tilde{H}(\omega)\right|$ are shown for the three different devices in Fig. 4.5. The current responses show different behavior for the three different cases (see Fig. 4.5). The response function in the frequency domain shows distinct behavior depending on the type of antenna and the CEP. The rectifying antenna shows for CEP $= 0$ a smooth envelope, while at CEP $= \pi$ the transfer function is reduced in amplitude and shows a sharp modulation. This is caused be two effects, visible in the time domain of the current. Due to the narrow envelope of the pulse the amplitudes of the contributing half-cycles in the CEP $= \pi$ case are significantly lower, causing an overall lower emission. The sharp modulation of the response function is caused by two equal height peaks in the time domain, where a signal at these frequency blindspots modifies the emission rate of the first peak to go slightly up and for the second peak equal amounts down or vice versa.

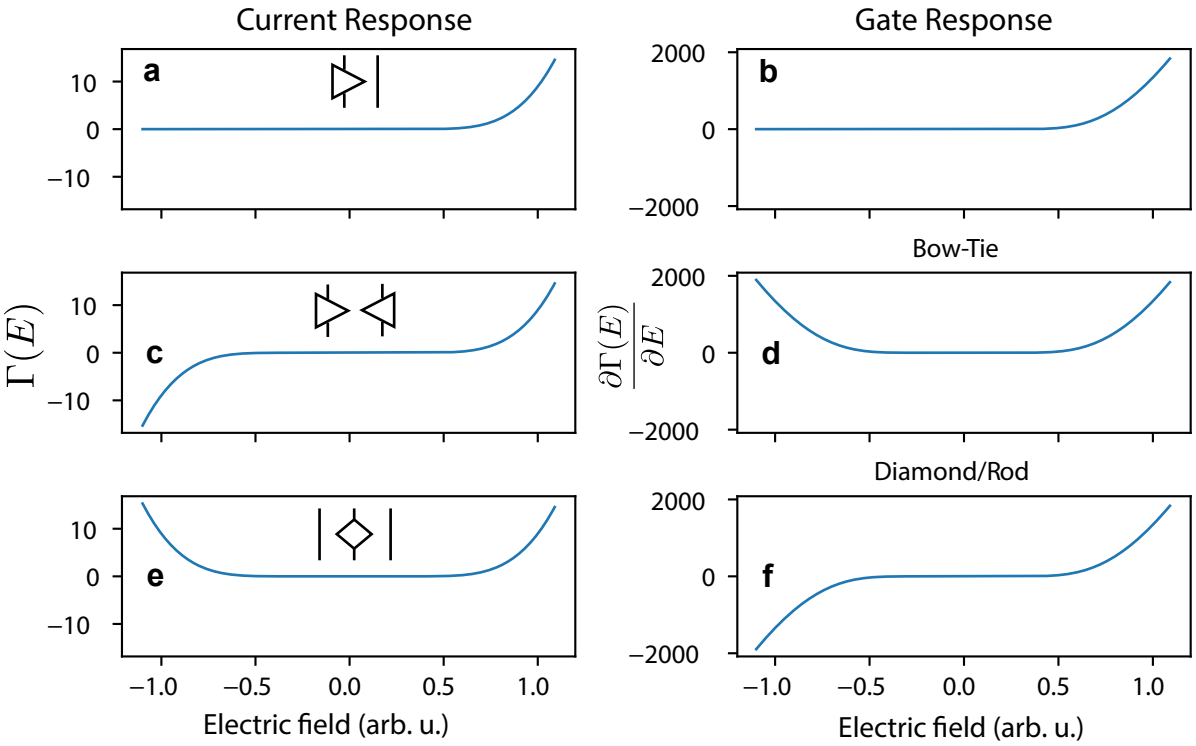

Figure 4.3: **Static Antenna Response Function:** (**a,b**) Response function of the current and gate of a rectifying antenna. (**c,d**) Response function of the current and gate of a bow-tie antenna. (**d,e**) Response function of the current and gate of the diamond-type antenna.

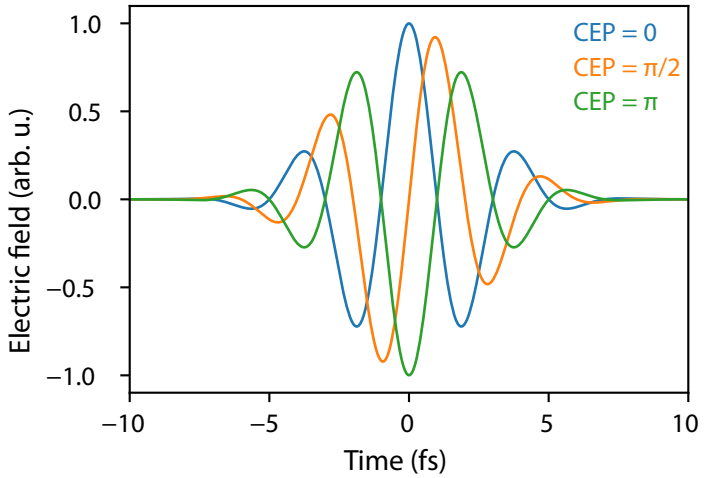

Figure 4.4: **Electric Field of a Single-Cycle Pulse:** Electric field of a single-cycle pulse with 4 fs duration at a center wavelength of 1.2 µm.

Similar behavior but at different harmonics is seen in all devices. In case of the bow-tie and the diamond-type antenna all CEP values show multiple current peaks in the time domain, which transfers to a modulated spectrum for all cases. With the response function symmetries, point symmetry for the bow-tie and mirror symmetry for the diamond-type antenna, we see differ-

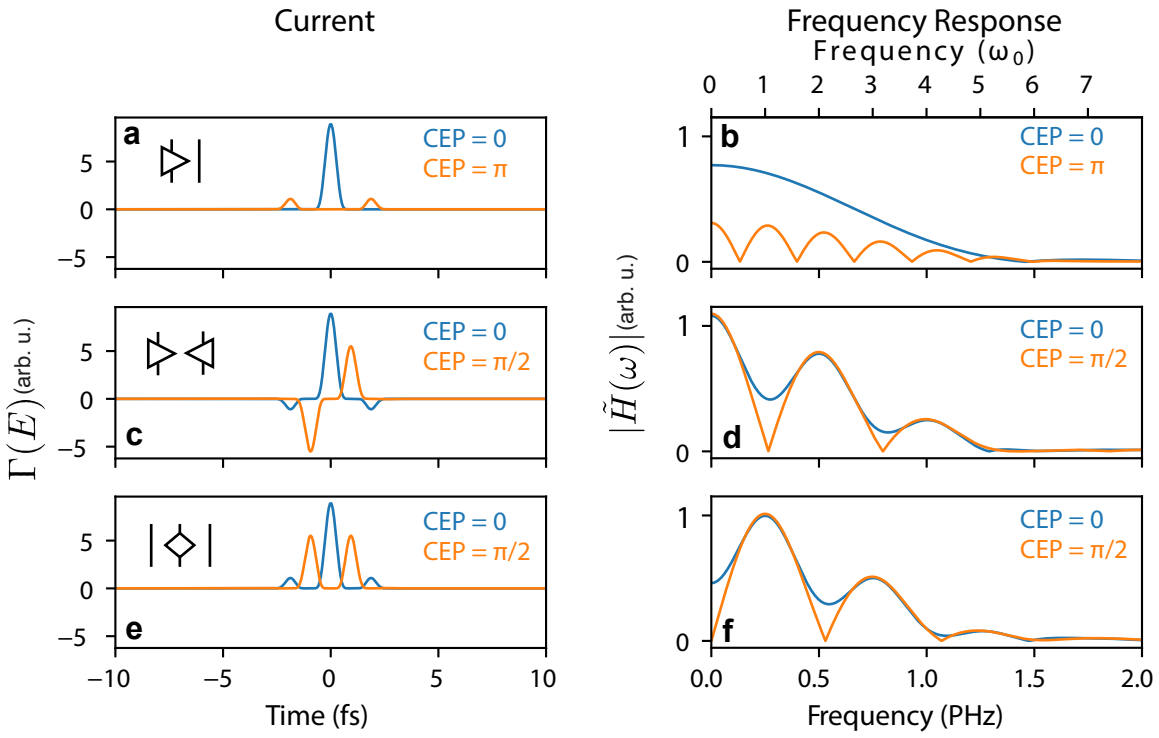

Figure 4.5: **Antenna Response Function:** Time domain current of different antenna types as a function of CEP, driven by pulses, as shown in 4.4. Accessible sampling frequency response of the respective antenna cases and CEP. (**a, b**) Time response of the current and accessible sampling bandwidth for a rectifying antenna. (**c, d**) Time response of the current and accessible sampling bandwidth for a bow-tie antenna. (**e, f**) Time response of the current and accessible sampling bandwidth for a diamond-type antenna.

ent accessible harmonics in the frequency domain. The bow-tie is sensitive to even harmonics, whereas the diamond-type is sensitive to odd harmonics. Considering the CEP dependence, we also see sharp cuts into the frequency response at CEP $= \pi/2$. As was noted earlier this analysis is not limited to the nanoantenna case, as response functions similar to Fig. 4.3 can be constructed in other test cases. The diamond-type antenna with mirror symmetry is qualitatively identical sampling techniques based on in-air ionization [16], as the ionization yield is counted independently from the direction of the electric field. This fact is also supported, that a strong CEP modulation is present for these techniques at the second harmonic [16, 19]. In contrast to ionization of air or the nonlinear injection of charge carriers into the conduction bands of solids, sampling techniques based on emission from a sharp metal-vacuum interface allows for rectification otherwise not accessible in isotropic media. In addition, by using resonant nanoantenna structures the emission direction can be tailored by the device geometry to construct the desirable sampling response. This demonstrates how the geometry of the device can select specific frequency bands and is advantageous for designing devices for specific applications.

The ability of to engineer the frequency response of the devices via simple geometric con-

siderations is advantageous for many applications. For infrared frequencies down to terahertz frequencies, a common technique is electro-optic sampling, which is based on the generation of sum-frequencies in a nonlinear crystal [96, 97], but is limited in its frequency range due to phase-matching constraints [97, 98]. In the case of the nanoantenna, which is usually 30 nm in thickness, there would be no phase-matching issue for low frequencies. By choosing a bow-tie nanoantenna, a sampling device could be designed that continuously covers the entire frequency range from gigahertz to hundreds of terahertz. In addition, integrated nanoantennas are also an excellent candidate to replace Auston switches on-chip terahertz spectroscopy[99], which is based on the detection of terahertz pulses in electrical circuits [100].

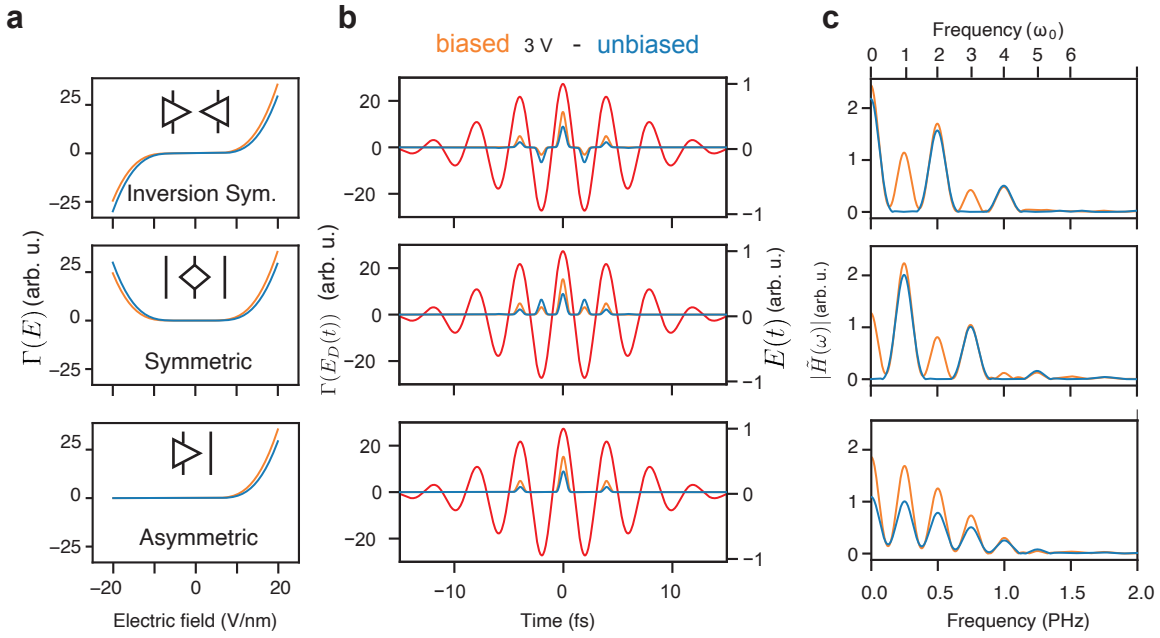

Figure 4.6: **Antenna Response for different Devices with and without Bias:** (**a**) Static response function of the devices presented in Fig. 4.2 with and without a static bias of 3 V. (**b**) Instantaneous current response for the respective devices shown in a, with and without a static bias of 3 V. (**c**) Sampling frequency response of devices presented in a, with and without a static bias of 3 V.

Furthermore, due to the field enhancement of the antenna and nanometer gap distances, it is possible to apply DC biases at the volt scale that provide local field strength on the order of $> 100\,\mathrm{MV\,m^{-1}}$, which can fully reconfigure the dynamics of electron emission and transport [101]. With 15 nm gap size, a field enhancement of 10 and a 3 V bias the local field strength at the nanotip reaches up to $1\,\mathrm{GV\,m^{-1}}$. To consider the influence of such a bias on the frequency response of the sampling technique we calculate a test case for a drive laser pulse with 10 fs duration pulse and a center wavelength of 1.2 µm. This analysis is shown in Fig. 4.6. Starting with the static current response, the bias effectively tilts the static response function in the direction

defined by the bias, suppressing emission in one direction or the other. The instantaneous current is then modified according to the new effective response function. The frequency response $\left|\tilde{H}(\omega)\right|$ shows a behavior that is completely different from the unbiased case. Previously, only odd or even harmonics were available, but the bias breaks the original symmetry, and opposite harmonics become available. For the case of a rectifying antenna, no such behavior is seen, as it intrinsically already broke the symmetry and only broadband suppression or increase in the amplitude is observed. The possibility of applying strong biases to modify the sampling response is unique to the nanoantenna-based sampling technique and cannot be easily implemented in air- or solid-based techniques. It also has interesting applications, as the electronic bias enables modulation of certain frequency harmonics that can be turned on and off without changing the device geometry itself. Additionally, the response to a static bias is also useful for the indirect investigation of ultrafast transport in the time domain. An applied bias would give distinct changes in the frequency response depending on the symmetry properties of the transport.

5 Development of a CEP-stable Few-Cycle Source in the Mid-Infrared

Introduction

As this thesis investigates the attosecond fast emission of electrons from metal nanostructures, having a laser source that allows precise control over the electrical field of an optical laser is of utmost importance. The experiment presented in Chapter 3 used an erbium-based fiber oscillator at a repetition rate of 80 MHz pumping a highly nonlinear germanium doped silicate fiber [89, 90], generating 10 fs duration actively CEP-stabilized pulses at a center wavelength of 1.14 µm and 200 pJ pulse energies. The laser system shows that up to 10 nanoantenna pairs can be driven simultaneously to yield around 1 electron per shot in CEP-dependent charge [23]. Yang et al. showed that two orders of magnitude more electrons can be generated by pulses with single-cycle duration. Furthermore, scaling up the nanoantenna array size and pulse energy, while keeping the peak intensity for every antenna constant, would proportionally scale up the total charge yield to thousands of electrons with only nanojoules of pulse energy. This pushes the yield into a regime where single-shot charge detection becomes possible. Therefore, demonstrating single-shot readout of CEP-dependent charges is the precise goal for the laser system presented in this thesis. The underlying design concept was to achieve close to single-cycle CEP-stable pulses with at least tens of nanojoules of energy. Further, a longer central wavelength was considered to yield more emitted charge per half-cycle at the same peak field and also to have a higher ponderomotive energy ideal to drive field emission processes. The starting point was the seminal work of Krogen et al. [53], demonstrating single-cycle pulses in the MIR with 1.5 µJ of energy at a repetition rate of 1 kHz. They further demonstrated that with the approach of adiabatic difference frequency generation (ADFG), it is possible not only to generate but also to arbitrarily shape the output MIR waveform in spectral amplitude and phase. While this brings great flexibility in the control of the output waveform, it also adds a high degree of complexity to the optical setup, requiring acousto-optic programmable dispersive filters (AOPDF) and also sacrificing the total energy efficiency due to high losses. In addition, this system does not have CEP-stable output pulses, since it uses a large amplifier system for the ADFG pump that was not interferometrically stabilized with the seed pulse, which in the case of any DFG process will produce phase noise in the idler proportional to the relative phase noise between the pump and seed [102]. In general, the CEP stability of an ADFG process has not yet been investigated. However, this system is attractive and can be adapted with considerable design changes to a less complex optical setup while also operating at a higher repetition rate.
In this chapter, we describe a 1.7-cycle source at a center wavelength of 2.7 µm that is passively CEP-stable and runs at a repetition rate of 50 kHz delivering 84 nJ of energy. The first section presents a summary of the work published in optics letters. The later sections describe the system design in full detail, giving details on alignment, design strategies, and pulse characterization techniques.

5.1 Passively CEP Stable Sub-2-Cycle Mid-Infrared Laser Source

[1] Control over the carrier-envelope offset frequency and its time-domain counterpart, the carrier-envelope phase (CEP), on the one hand, allowed the link between optical and microwave domains with unprecedented precision, leading to important advances in metrology [45, 103]; on the other hand, allowed the stabilization of the electric field waveform of optical pulses, with major developments in strong-field physics [104]. Controlling the precise optical waveform enabled the generation and shaping of attosecond optical pulses via high harmonic generation and sparked a demand for ultrafast CEP-stable single-cycle sources in the near-infrared (NIR) [105]. A recent frontier in the development of novel single-cycle sources is the mid-infrared (MIR) spectral region, which opened the door to attosecond pulses spanning the soft X-ray region or controlling states of solid matter [99, 106]. Despite scientific motivation, the generation of milliwatt-level few- to single-cycle MIR pulses has proven difficult, and many different approaches have been explored [107]. One viable approach is to rely on parametric downconversion based on very mature and robust ytterbium pump laser technology. Krogen et al. implemented a first demonstration of single-cycle ultra-broadband MIR pulses through adiabatic difference frequency generation (ADFG) [53]. The benefit of adiabatic frequency conversion is that the MIR pulse inherits directly the amplitude and phase of the input NIR pulse [22]. This allows for tight control of the output MIR pulse properties by controlling the properties of the input NIR pulse. Remarkably, this allows one to precisely predict the MIR dispersion after the conversion process independent of seed intensity and spectral phase. Using this novel frequency conversion technique, Krogen et. al generated 11 fs pulses at a central wavelength of 2.8 µm with a pulse energy of 1.5 µJ and a repetition rate of 1 kHz, corresponding to 1.5 mW. In order to achieve such a short pulse duration, the system featured an acousto-optical programmable dispersive filter (AOPDF), including a grism compressor, allowing to shape the near-IR input. To compensate for the high losses introduced by the AOPDF setup, it was necessary to implement a two-stage NIR OPCPA scheme. This implementation allows compensating for higher-order dispersion of the ADFG process and for full pulse shaping of the MIR output around the optimum compression point. The carrier-envelope phase stability of pulses generated via adiabatic frequency conversion has not yet been characterized. This is extremely important for field-controlled experiments, which require tight control over the CEP while preserving a quasi-single-cycle waveform [8, 20, 105].

Here, we report a high repetition rate implementation of a passively CEP-stable adiabatic frequency down converter, relying only on material dispersion to compensate for the large ADFG dispersion and compress the octave-spanning MIR pulses to 16 fs at a center wavelength of

[1] This section is based on the work published in Optics Letters; see Ref. [54]. The author of this thesis, is the main author of this publication and was involved in every aspect of the creation of this manuscript from the design of the source, the construction, the characterization and the writing of the manuscript.

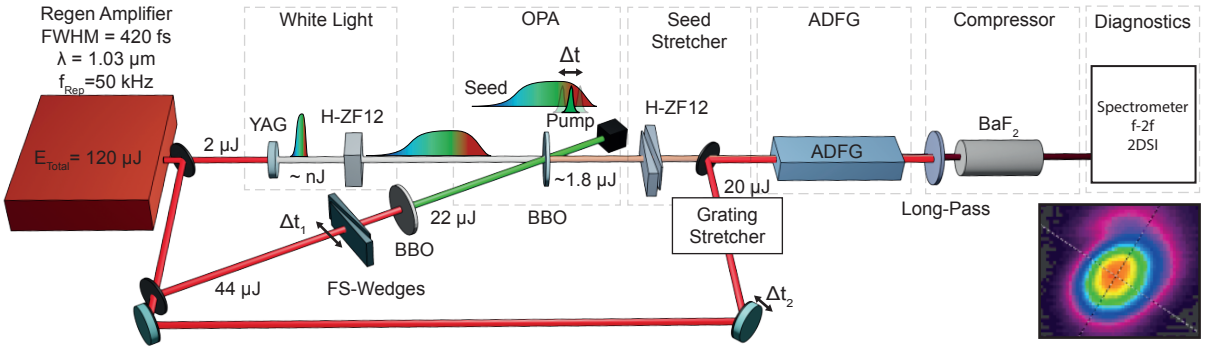

Figure 5.1: **Schematic system overview:** The whole system consists of a pump laser at 1.03 µm wavelength distributing 60uJ of energy to white light, an OPA, and an ADFG stage. Bottom right corner, a mid-infrared far-field beam profile after 2m of propagation. Abbreviations: yttrium aluminum garnet **YAG**; dense flint glass **H-ZF12**; β-barium borate **BBO**; barium fluoride glass **BaF$_2$**; fused silica **FS**.

2.7 µm. At a repetition rate of 50 kHz we achieve a pulse energy of 84 nJ resulting in 4.2 mW of average power. A simple dispersion management scheme based on bulk materials offers robust operation of the laser system. At the core of the laser system is the adiabatic difference frequency generation process, which allows the conversion of a broadband NIR pulse into an octave-spanning MIR pulse mediated by a strong intermediate wavelength narrowband pump. Detailed background on ADFG is found in references [22, 53]. During an ADFG conversion process, the input pulse propagates through the adiabatically poled crystal, experiencing a slowly swept phase-matching condition that eventually crosses the $\Delta k = 0$ phase-matching point for every wavelength within its spectrum (see supplementary Fig. 5.7) [22]. When the ideal phase matching is crossed, NIR waves at frequency ω_{NIR} undergo an almost instantaneous conversion into MIR waves at frequency $\omega_{MIR} = \omega_{NIR} - \omega_{Pump}$, called rapid adiabatic passage [22]. Therefore, the total ADFG dispersion $\tau_{ADFG}(\omega)$ as a function of frequency ω is considered to be the group delay of the NIR photon τ_{NIR} acquired until the phase matching point $z_c(\omega)$ plus the group delay τ_{MIR} acquired propagating as a MIR photon after the phase matching point [22, 53]. This can be summarized in the following analytic expression describing the resulting group delay in the mid-IR,

$$\tau_{ADFG}(\omega) = \frac{dk}{d\omega}(\omega + \omega_{pump}) \cdot z_c(\omega) + \frac{dk}{d\omega}(\omega) \cdot (L - z_c(\omega)), \tag{5.1}$$

given an ADFG crystal of length $L = 20$ mm and an aperture of 2 mm by 1 mm. Here, k is the frequency-dependent wave vector in $LiNbO_3$ [108]. In this implementation of an adiabatic difference frequency converter, we use a crystal design identical to [53] and have to compensate mainly for the second and third-order dispersion. Compression is achieved by balancing the acquired total dispersion through the material passage of the NIR seed and the MIR output. Considering that the MIR pulse is generated from a well-defined NIR pulse, it can effectively inherit normal dispersion from the original NIR pulse that propagated through materials like

dense flint glass. After down-conversion, the MIR pulse can easily acquire anomalous dispersion through propagation in materials like barium fluoride. The balancing of these contributions allows for flexible compression of any second-order dispersion of the system. The compensation of higher-order dispersion (as third-order) can be achieved through numeric optimization of the inserted material type and its thickness for the shortest output pulse at a given spectrum. This allows for effective compression of the MIR output without the need for chirped mirrors, prisms, gratings, or active dispersion elements, therefore keeping the optical setup very simple. Our system design is shown in Fig. 5.1. The pump laser is a commercial Yb:KYW regen producing 420 fs duration pulses at a wavelength of 1.03 µm and a repetition rate of 50 kHz. We use 70 µJ of the available 120 µJ of pulse energy for our generation scheme. To generate a broadband NIR seed for the ADFG process, we use a noncollinear OPA. This OPA is pumped by the second harmonic of the laser fundamental (515 nm, 22 µJ, generated in 2 mm long β-barium borate crystal) and seeded via white light (WL) generation in a 4 mm long yttrium aluminum garnet (YAG) crystal [109]. The WL pulse is short-pass filtered with a cut-off at 900 nm and stretched by 2 mm of dense flint glass (H-ZF12) in order to match its duration to the duration of the OPA pump in the crystal. The OPA crystal is β-barium borate cut at $\alpha = 24.1^\circ$ and 1.5 mm long). The angle between the pump and the seed is $\sim 2.4^\circ$ inside the crystal. The center wavelength of the broadband amplified signal can be tuned by controlling the pump-seed delay via the insertion of a fused silica wedge in the pump beam path. The resulting NIR spectrum is shown in Fig. 5.2. The NIR signal with a central wavelength of ~750 nm (see Fig. 5.2) has an energy of 1.8 µJ. To precompensate for the dispersion of the ADFG stage and the bulk material placed afterwards, the NIR seed is initially stretched by bulk 2 mm H-ZF12 and 3 mm BK7. Afterward, an antireflection coated wedge pair of H-ZF12 with a thickness of 5 mm and a tuning range of $\pm$2 mm allows continuous control of NIR dispersion. The pulse duration of the NIR seed at the input of the ADFG is $<$1 ps. To avoid temporal walk-off during the ADFG process, the pump laser is stretched in a transmission grating stretcher to ~10 ps. The pump pulse with 20 µJ energy is then shallowly focused a few cm in front of the crystal to allow for a large and slightly divergent mode of ~0.75 mm diameter (at $1/e^2$) and a peak intensity of $< 1\,\mathrm{GW\,cm^{-2}}$ within the crystal. The NIR seed is focused in the center of the ADFG crystal with a mode size diameter of 280 µm (at 1/e2) and collinearly propagates with the pump beam. This mode configuration sufficiently approximates a spatially homogeneous pump intensity perceived by the seed. The resulting MIR spectrum is shown in Fig. 5.2. In addition, we emphasize the great flexibility of the adiabatic downconverter supporting spectra at different central wavelengths making it continuously tunable from 2 µm to 3.5 µm, see supplementary Fig. 5.8. The measured spectrum shows complete down-conversion of the broadband NIR signal spectrum into an octave-spanning MIR spectrum, covering 2 µm to 4.5 µm. The MIR output reaches an average power of 4.2 mW corresponding to 84 nJ, which includes reflection losses during the compression process. To separate the MIR from the residual signal and pump light, a custom long-pass filter with a cut-off at 1.25 µm and 2 mm of Si at the Brewster angle are used. The

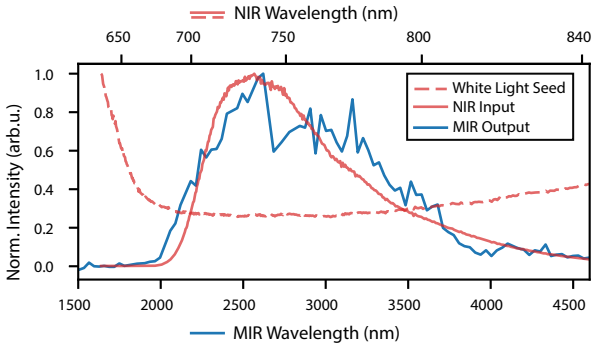

Figure 5.2: **Optical Seed and Output Spectra:** Spectral intensities of the white light seed, the near-infrared input measured on Si-CCD spectrometer and the corresponding MIR spectra measured with a PbSe-CCD based spectrometer (Spectral Products, SM301EX, $\Delta\lambda = \sim 25 - 30$ nm).

resulting MIR beam profile measured on a pyroelectric camera is shown in the inset of Fig. 5.1. For the final compression 39 mm of barium fluoride (BaF_2) are inserted. To benchmark the pulse-to-pulse intensity fluctuations we measured the MIR output over 1 s at a bandwidth of 80 kHz on a mercury cadmium telluride detector and recorded a relative intensity noise of 1.3 % RMS. See supplementary Fig. S2 for the data. The fluctuations can be explained as follows: the intensity noise of the pump laser fundamental is $\sim$ 0.5 % rms. The SHG output pulse has therefore $\sim$ 1 % fluctuation that is imprinted on the NIR OPA output (plus additional fluctuations from the white light). In the ADFG the pump fluctuation should be irrelevant, while the NIR fluctuation will be directly imprinted on the MIR output. For the spectral phase characterization,

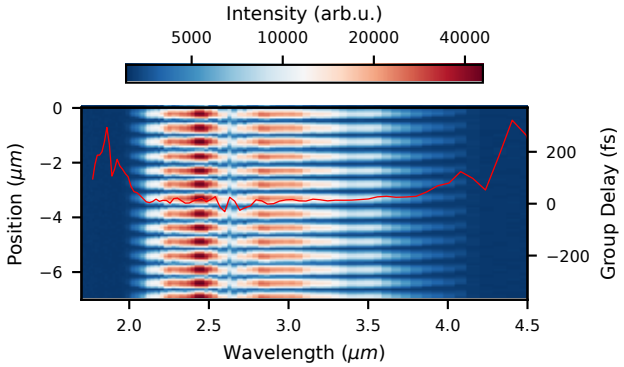

Figure 5.3: **Two-dimensional spectral shearing interferometry:** Recorded interferogram of the compressed broadband MIR pulse and two narrowband ancillaries at 1.03 µm separated by 1.35 THz. The 2d color map is shown with logarithmic color scaling. The secondary Y-axis shows the group delay (red line) retrieved from the shown interferogram.

we adapted two-dimensional spectral shearing interferometry (2DSI). In 2DSI the MIR pulses are upconverted with two narrowband ancillaries with a shear frequency of 1.35 THz derived from the pump laser [91, 110]. This allows the up-converted spectrum to be in the easy-to-detect

NIR spectral region between 650 nm and 850 nm. The resulting 2DSI measurement is shown in Fig. 5.3. The derived group delay shows a reasonably flat behavior between 2 µm and 4 µm. Furthermore, we note that there are strong group delay oscillations at ∼2.7 µm, which originate from several known water absorption lines in this spectral band [111]. The temporal envelope of the compressed MIR pulse is retrieved by combining the calibrated spectral amplitude measurement with the retrieved group delay, as presented in Fig. 5.4, [112]. The MIR pulse duration is 16 fs that, at a center wavelength of 2.7 µm, corresponds to 1.7 cycles at FWHM, see Fig. 5.4 and Fig. 5.5. We attribute the precursor pulse appearing at a time delay of $t = -60$ fs, to residual third-order dispersion, effectively interfering with the low- and high-frequency wings of the pulse in the time domain. The achieved pulse duration is only 1.14 times longer than the transform-limited duration of 14 fs.

To characterize the carrier-envelope phase of the system, we set up an f-2f interferometer

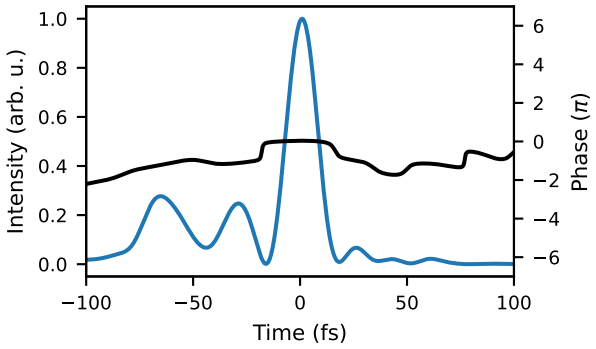

Figure 5.4: **Temporal Shape:** Pulse shape (blue) and phase (black) retrieved from the measured MIR spectrum and the measured group delay from Fig. 5.3.

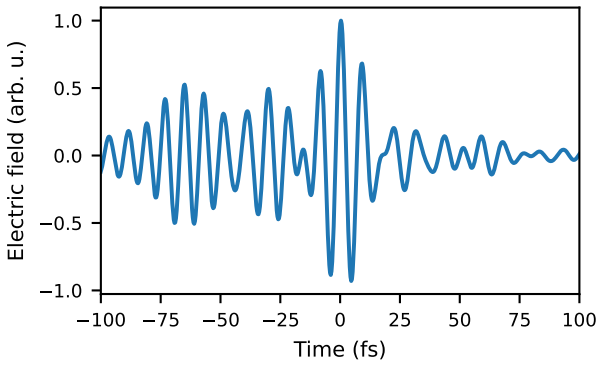

Figure 5.5: **Electric field transient:** electric field transient calculated from the measured MIR spectrum and the group delay from Fig. 5.3 at an arbitrarily chosen CEP.

that frequency doubles the long wavelength side of the octave-spanning MIR spectrum in a silver thiogallate crystal (AGS) and creates spectral interference on the short wavelength side [113]. The spectra are recorded with a bandwidth of 3 Hz and an integration time of 2 ms, cor-

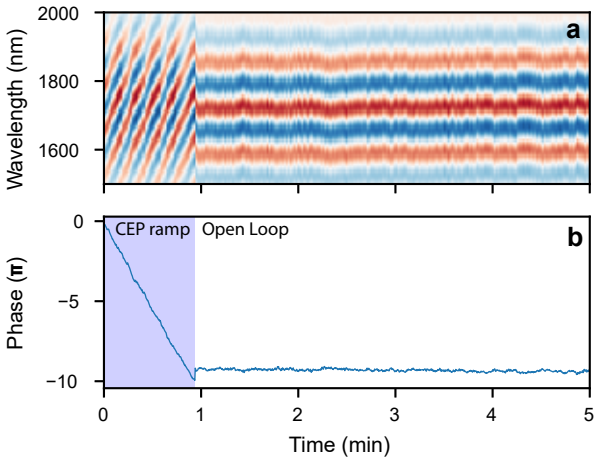

Figure 5.6: **CEP-Control and Open-Loop Stability:** a) f-2f interferogram of the octave spanning MIR pulse. The first 50 s shows a linear ramp of the CEP. 50 s to 5 min show a open loop CEP. b) Relative CEP obtained from a), showing the linear phase ramp and the open loop phase stability.

responding to an average of over 100 individual pulses. The filtered interference pattern from the measurement is shown in Fig. 5.6 **a** with the retrieved phase in **b**. To verify the control of the CEP, we linearly sweep the relative phase between the pump and seed in the ADFG stage by simply shifting the delay of the pump over 5150 nm (five times the pump wavelengths). This causes a highly linear shift of the interference pattern, which is also reflected in the retrieved phase. After 50 s the phase sweep is stopped and the CEP is running freely for the rest of the measurement. As can be seen, already the passive stability of the CEP is high with less than 190 mrad rms over 15 min (see Fig. 5.9 for the full data range).

In conclusion, we have demonstrated the first passively CEP stable implementation of an ADFG-based MIR source that provides 1.7-cycle pulses at a central wavelength of 2.7 µm with an excellent passive CEP stability of 190 mrad. Remarkably, close-to-transform limited compression is achieved by using only propagation in bulk materials, which improves the inherent stability of the system. This demonstration further emphasizes that the inherent one-to-one pulse transfer in adiabatic frequency conversion techniques allows for simple compressor designs, due to the precisely predictable system dispersion. With that information, one can also design custom chirped mirrors that compensate for the specific dispersion of a given adiabatic frequency converter, enabling the compression of even broader spectra than those demonstrated in this work and full elimination of higher-order dispersion components. The presented setup is an excellent addition to many existing OPA sources, that can convert broadband non-CEP stable NIR pulses to octave-spanning CEP stable few- to single-cycle pulses in the MIR. This source provides pulses with ideal characteristics for many non-linear field-sensitive experiments in solids, such as petahertz electronics and field sampling [20, 48].

5.1.1 Additional Figures

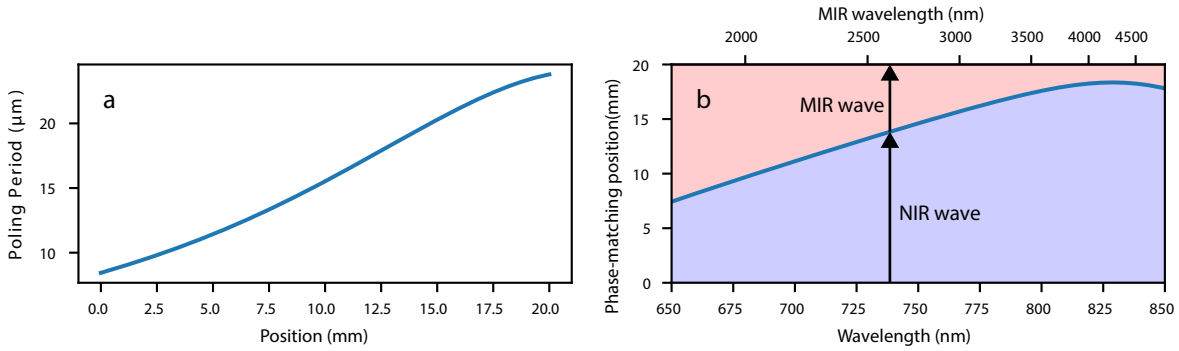

Figure 5.7: **Poling period and phase-matching points of the ADFG crystal: a,** Poling period of the magnesium doped lithium niobate crystal used for the ADFG conversion process. **b**, Phase-matching points along the propagation direction in the ADFG crystal as a function of the wavelength of the NIR input and the MIR output. The arrows symbolize a NIR wave propagating until the conversion point and propagating for the rest of the crystal as a MIR wave.

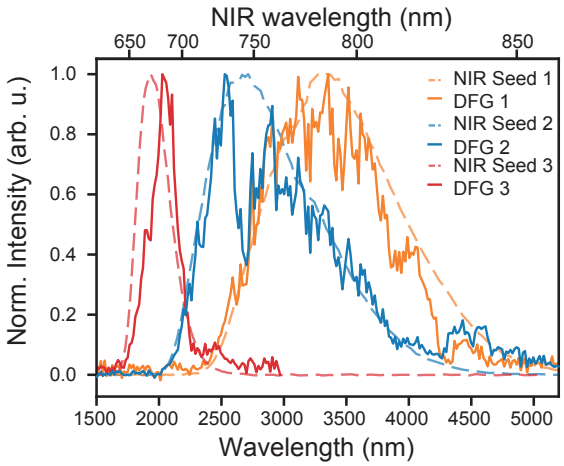

Figure 5.8: **Optical seed and output spectra tuning range:** Spectral intensities of the near-infrared seed spectra measured on Si-CCD spectrometer and the corresponding MIR spectra measured with a PbSe-CCD spectrometer. The tuning of the center wavelength is achieved through a varied delay between the pump and seed in the non-collinear OPA.

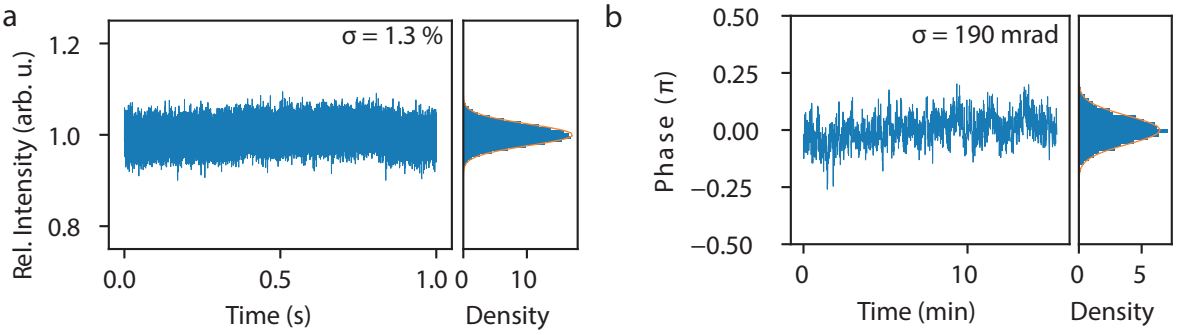

Figure 5.9: **Stability measurement of intensity and carrier-envelope phase:** a) The intensity fluctuations are measured at a bandwidth of 50 kHz with an 80 kHz bandwidth mercury cadmium telluride detector over 1 s. The statistical distribution of measurement values is shown in the histogram in blue with a normal distribution fit in orange. b) The phase measurement is implemented by f-2f interferometry at a sampling rate of 3 Hz and an integration time of 2 ms corresponding to averaging over 100 laser shots. The statistical distribution of measurement values is shown in the histogram in blue with a normal distribution fit in orange.

5.2 Technical Information

This section is intended to supplement the description of the laser source described in the previous section by providing additional information that was not published in Ref. [54]. It will provide background information, detailed setup sketches, recommended alignment strategies, and benchmark figures for correct alignment.

5.2.1 Detailed Setup Overview

This section gives a detailed drawing of the optical layout of the MIR generation setup; see Fig. 5.10. The system is pumped by a commercial Yb:KYW regen amplifier from Amplitude that delivers 420 fs pulses at a center wavelength of 1.03 µm, with a pulse energy of up to 120 µJ at a repetition rate of 50 kHz, not shown in the drawing. The design guideline behind the optical layout is to reduce the total beam path for the ADFG seed and the pump beam, leading to better passive timing stability between the two, since a relative phase jitter directly translates into CEP noise in the DFG process [102].

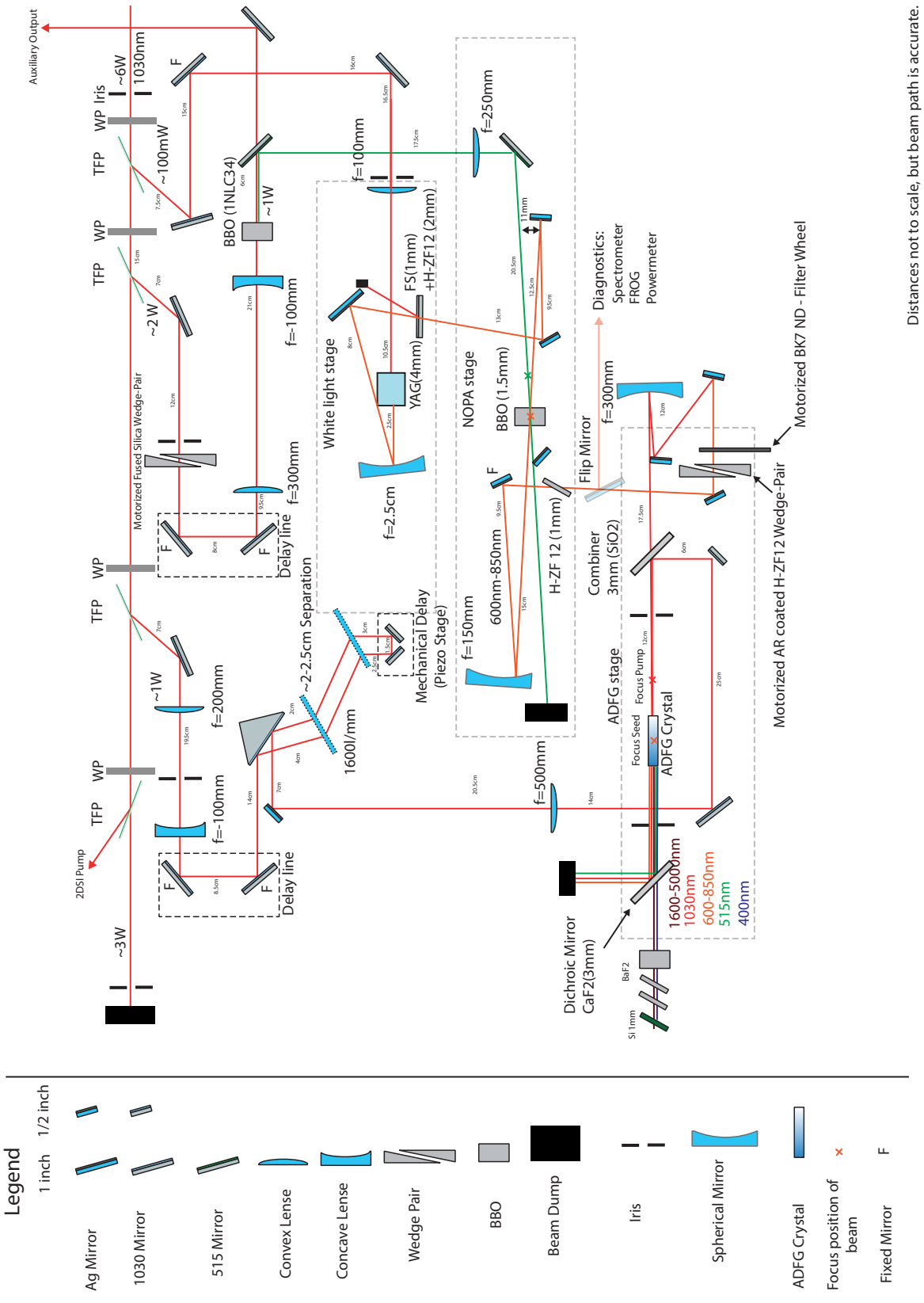

Figure 5.10: **Detailed Sketch of the Optical Setup:** The sketch includes the full optical layout with the latest distance measurements of the beam paths. At the bottom, a legend of all non-annotated components can be found.

5.2.2 White Light Generation

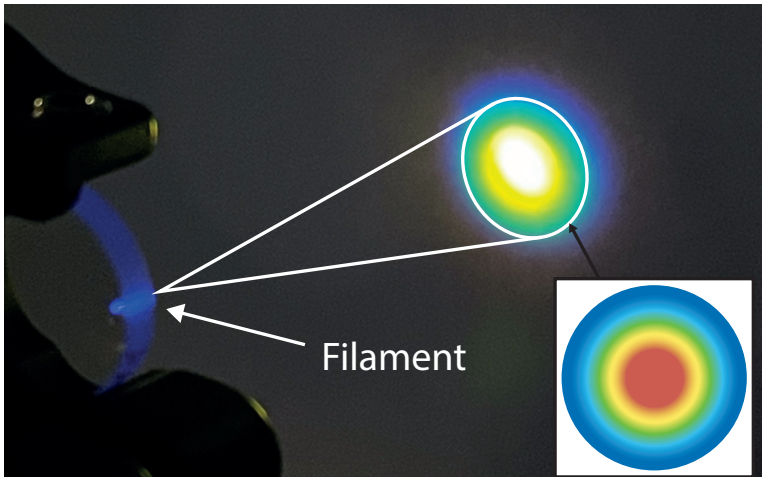

Figure 5.11: **White Light Spectrum:** White light spatial mode generated in 2mm of yttrium aluminum garnet (YAG) with ∼2 µJ of energy, with an idealized color distribution as an inset. The camera saturates in the central mode and the image, therefore, appears white.

To seed the optical parametric amplifier, we generated a broadband white light in a yttrium aluminum garnet crystal (YAG). This highly nonlinear process can yield octave-spanning coherent spectra and is a cornerstone to most modern optical parametric amplifiers, details are extensively discussed in [109, 114, 115]. For the generation, ∼2 µJ of pump energy are split via thin film polarizer from the pump distribution line, see Fig. 5.10 for details. The pump beam is sent to a planoconvex BK7 lens with a focal length of 100 mm and a 1-inch iris attached to the lens mount on the input side. The YAG crystal is positioned within 1 mm behind the focus. The crystal thickness of 4 mm is chosen to avoid long-term optical damage, which was found to occur with thinner crystals at high repetition rates [109]. Nevertheless, damage can only be postponed but not completely avoided, therefore the crystal is placed on a translation stage with lateral translation to the beam axis. When sufficient energy is provided and the crystal is at the correct position, a small blueish filament appears inside the crystal, and a large visible mode appears at the output; see Fig. 5.11 for reference. The spatial mode should be homogeneous and radially symmetric; sharp features indicate multiple filaments or some other not desired process.

After generation, white light is refocused 550 mm downstream into the NOPA stage by a concave silver mirror with a focal length of 25 mm. During propagation, the white light passes a short-pass filter with a cut-off at 900 nm (Asahi Spectra USA, XIS0900). Under ideal operation, the spectrum has a shape similar to Fig. 5.12, and the output energy after the short-pass filter is on the order of few nJ.

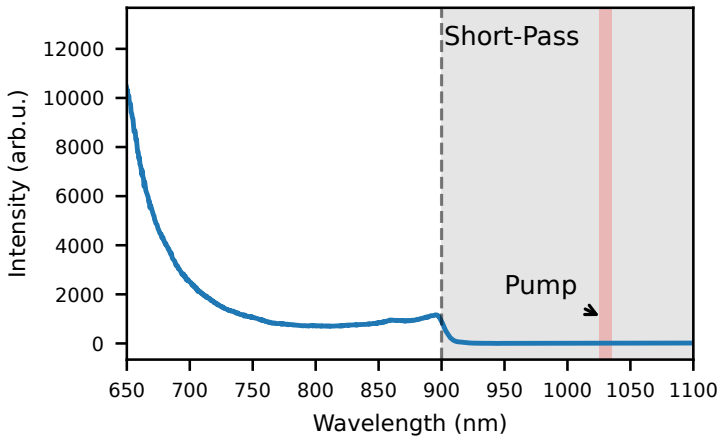

Figure 5.12: **White Light Spectrum:** White light spectrum generated in 4mm of yttrium aluminum garnet (YAG) with ∼2 µJ of energy. The spectrum is filtered with a 900 nm short-pass filter (Asahi Spectra USA, XIS0900).

Alignment

When aligning the white light, care must be taken with the position of the crystal and the adjustment of the input energy. Ideally, the crystal is moved slowly from behind the focus towards the focal point while adjusting the input energy to keep a homogeneous radially symmetric mode, as demonstrated in Fig. 5.11. The optimization should lead to a minimization of input energy while keeping a spatial mode as shown in Fig. 5.11. When the white light is driven with not enough pump energy, it may still yield a homogeneous mode, but with fewer red components of the center. This configuration has shown in experience higher shot-to-shot noise fluctuations and should be avoided. Also, the phase noise can be higher depending on the input energy and the state of the filament; see Baltuska et al. for details [116].

5.2.3 Non-Collinear Optical Parametric Amplifier

The non-collinear optical parametric amplifier (NOPA) provides the few-µJ seed to the ADFG stage to produce the MIR output. As the NOPA dictates the bandwidth and general output characteristics of the ADFG downstream, it is important that the NOPA bandwidth and general output are matched accordingly. To ensure that a surplus of bandwidth is accessible, the NOPA is configured non-collinearly at the *magic-angle* of ∼2.3° between pump and signal within the nonlinear crystal [59]. Details for the theoretical description and design criteria of a NOPA are found in reference [59]. The nonlinear crystal is β-barium borate (BBO) cut at 24.2° for type I phase matching with 1.5 mm thickness and a protective coating centered at 515 nm (Provided by United Crystals Inc.). The pump beam is focused a few centimeters in front of the nonlinear crystal and has a beam size of ∼0.14 mm (FWHM); see Fig. 5.13. The pump pulse energy is set to ∼20 µJ, resulting in a peak intensity of ∼188 GW cm^{-2}. The pump is spatially and temporally overlapping with the white light seed at the position of the BBO. The beam size

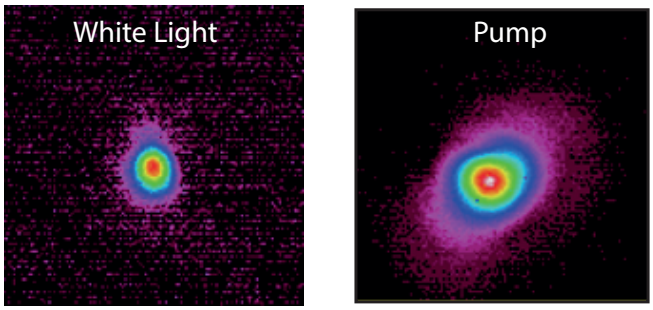

Figure 5.13: **White Light and Pump Focus Mode:** Focal modes of the white light and the pump in the NOPA stage. Full width at half-max beam sizes: **White Light**, major axis = 99 µm, minor axis = 84 µm; **Pump**, major axis = 145 µm, minor axis = 134 µm

of the white light is slightly smaller than the pump at a FWHM width of ∼90 µm. When the NOPA operates in the right configuration, a unique visible color pattern spreads over a few degrees from the pump. This color pattern is shown in Fig. 5.14 and is a strong indicator of an alignment close to the optimum. However, most of these colors are parasitic effects and second harmonic of the actual amplified signal and idler, as these are in the near-infrared and therefore not visible with a standard camera. The amplified signal has an output energy of up

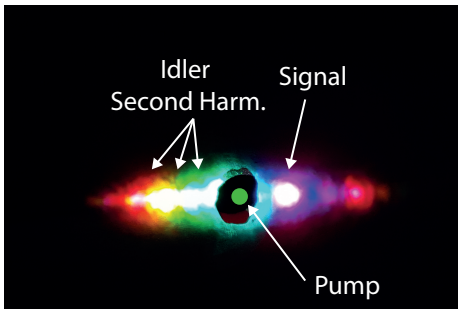

Figure 5.14: **Image of NOPA Output:** Image of the angular color pattern formed by the NOPA. The pattern is projected onto a white screen with a center hole to suppress the otherwise dominating pump light.

to 1.8 µJ that spectrally spans from 690 nm to 850 nm. The recorded spectrum and a far-field beam profile are shown in Fig. 5.15. The beam profile has a FHWM diameter of ∼800 µm and is slightly elliptical due to the non-Gaussian focii of the pump and seed.

Alignment

When aligning the NOPA a few, key points need to be kept in mind. First of all the spatial and temporal overlap need to be ensured. When the two path lengths of seed and pump are measured within a ∼1 cm difference, a camera can be placed in the position of the BBO (Pump and seed need to be attenuated to not destroy or saturate the camera). To achieve the *magic-angle* configuration, the seed, and pump need to be separated by ∼11 mm horizontally at the

position of the last seed mirror before the BBO. With that ensured the last mirror can be used to spatially overlap the seed and the pump. In case of the seed being larger than the pump, the stage of the concave mirror imaging the white light into the BBO needs to be adjusted, so that the beam sizes roughly match Fig. 5.13. The next step is to replace the camera with the BBO again and adjust the input surface so that the reflection of the pump beam is reflected back towards the last pump mirror. The temporal focus is found by moving the delay line of the pump beam until visuals, similar to Fig. 5.14 appear. To optimize, the NOPA output it is sent into the diagnostic beam path, see Fig. 5.10. Here, the average power and spectrum can be recorded simultaneously. By adjusting the last two mirrors of the white light one can carefully optimize for maximum output power. When the average power exceeds 50 mW the spectrum can be optimized by moving the motorized wedge pair in the pump beam path to change the temporal overlap, by adjusting the spatial position of the seed and the angle of the BBO. These steps need to be repeated iteratively to obtain the output performance, spectrum, and beam shape as described above.

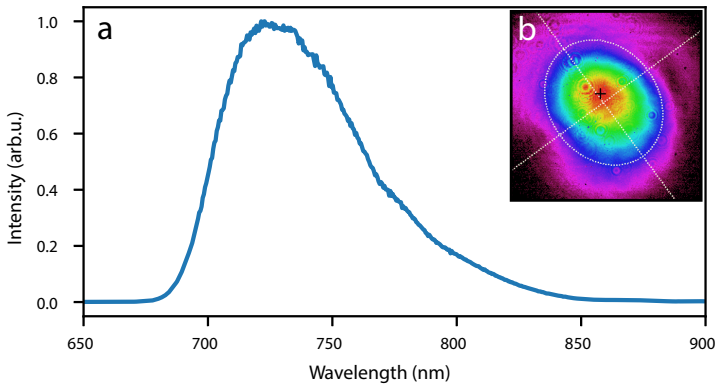

Figure 5.15: **NOPA Spectrum:** (**a**) Measured normalized spectrum of NOPA output at an average output power of 85 mW. (**b**) Measured far-field beam mode of NOPA; major axis = 850 µm, minor axis = 700 µm.

5.2.4 Adiabatic Difference Frequency Generation

Adiabatic frequency conversion techniques, as developed by Suchowski et al. [22], offer broadband conversion of optical pulses, with a theoretical photon conversion efficiency of up to 100 %. Specifically, adiabatic downconversion has been shown to be extremely broadband and to achieve octave-spanning pulses in the MIR [53]. To highlight the differences from conventional OPAs, an energy diagram of the downconversion process is shown in Fig. 5.16. Whereas a conventional OPA includes a strong narrowband pump that has the highest photon energy, providing parametric gain to a broadband seed/signal and generating an idler pulse to fulfill energy conservation in the process, in an adiabatic downconversion process the role of seed and pump are inverted. In an ADFG process, the pump merely provides coupling between the broadband seed and the idler by driving the nonlinearity in the optical crystal. More specifically, the process is called adiabatic in the sense that the energy of the seed is adiabatically transferred to the idler, as an optical analog of rapid adiabatic passage (RAP) in a two-level system [22]. To create adiabatic energy transfer, pump, and seed waves co-propagate through a periodically

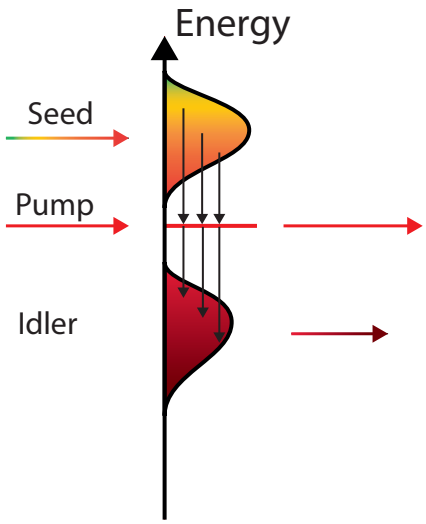

Figure 5.16: **Energy Diagram of an Adiabatic Downconversion Process:** Energy level diagram of the adiabatic downconversion process, showing the conversion of a broadband seed into a broadband idler mediated by a narrowband pump.

poled magnesium-doped lithium niobate crystal with a slowly swept polling period, as shown in Fig. 5.17. The slow change of nonlinear coupling through the swept phase matching creates RAP from the seed wave to the idler, causing an almost instantaneous transfer of energy from the seed to the pump and idler. This allows conceptually to treat the conversion process in a way that the NIR wave propagates through the crystal up to the conversion point and then propagates as a MIR wave, see Fig. 5.17. The ADFG device design used in this thesis is identical to that

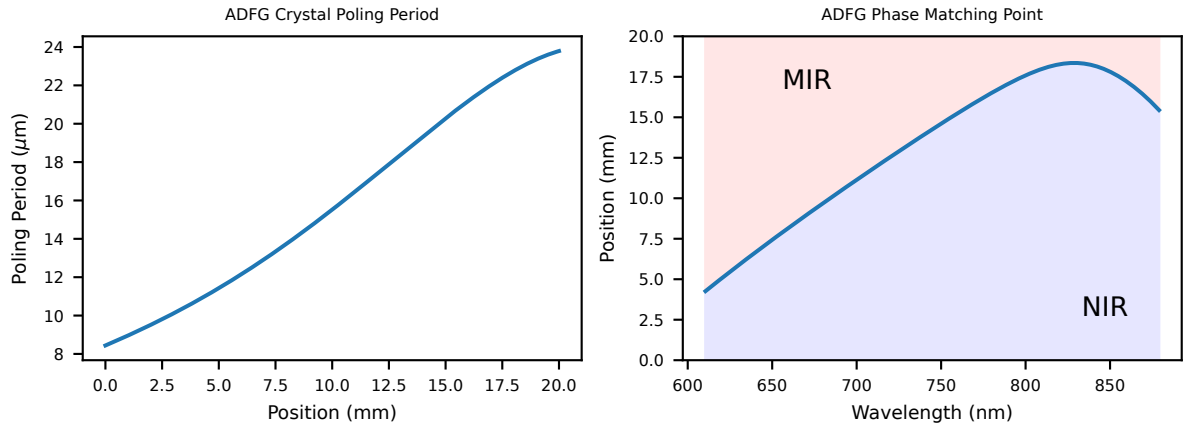

Figure 5.17: **Poling Period and Phase-Matching of the Adiabatic Frequency Converter:** (Left) Poling period of the ADFG device as a function of position along the crystal axis. (Right) ADFG phasing matching point along the crystal axis as a function of wavelength. The shaded areas mark where the propagating photons can be considered NIR or MIR.

used by Krogen et al. [53]. The polling period is described by a fifth-order polynomial,

$$\begin{aligned}\Lambda(z) =&(-1.93\cdot10^{-6})\cdot z^5+(-3.99\cdot10^{-6})\cdot z^4+\\&(-7.53\cdot10^{-4})\cdot z^3+(1.51\cdot10^{-2})\cdot z^2+(5.05\cdot10^{-1})\cdot z+8.44.\end{aligned} \tag{5.2}$$

The device was designed for a peak intensity of $10\,\mathrm{GW\,cm^{-2}}$ with a quasi-CW pump (duration much longer than the signal), to provide sufficient coupling. To achieve quasi-CW operation, the pump is stretched to $\sim$10 ps in a transmission grating stretcher using two gratings with a line density of 1600 lines/mm and an angle of incidence of 55.5° (T-1600-1030s-31.8x12.3-94, IIVI Inc.). The gratings are separated by $\sim$2.5 cm and generate $1\,300\,000\,\mathrm{fs^2}$ group delay dispersion, stretching the pump pulse to $\sim$10 ps. The pump pulse is focused with a planoconvex BK7 lens with a focal length of 500 mm a few centimeters in front of the ADFG crystal to result in a slowly converging mode. The pump and seed focal modes are measured with a camera at the position of the crystal and are shown in Fig. 5.18. To achieve an ideally homogeneous pump distribution inside the crystal, the pump mode is chosen twice the size of the seed mode. To set the sufficient pump energy, the MIR output is measured in the spectrum and average power as a function of the pump average power. The results are shown in Fig. 5.19 a. As ADFG conversion depletes the NIR pulse, the MIR output saturates when no more NIR energy is available, which is reflected in both the measurements of the spectrum and average power. As the MIR output power also depends on the NIR input power, the measurement presented here is an intermediate characterization of the system. The highest MIR output power achieved is 4.2 mW with the NOPA performance described in the previous section. The far-field beam profile is then measured with a Pyrocam IIIHR (Ophir Spiricon) at 2 m downstream of the ADFG crystal. To explore the accessible conversion bandwidth of the ADFG stage, the central

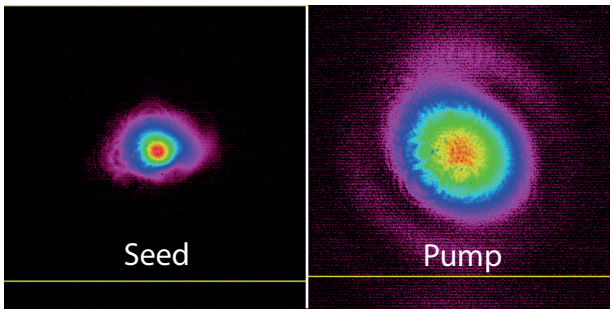

Figure 5.18: **Focii of Seed and Pump in the ADFG Stage:** Focal modes of the seed and the pump in the ADFG stage. Full width at half-max beam sizes: **Seed**, major axis = 180 µm, minor axis = 150 µm; **Pump**, major axis = 480 µm, minor axis = 400 µm.

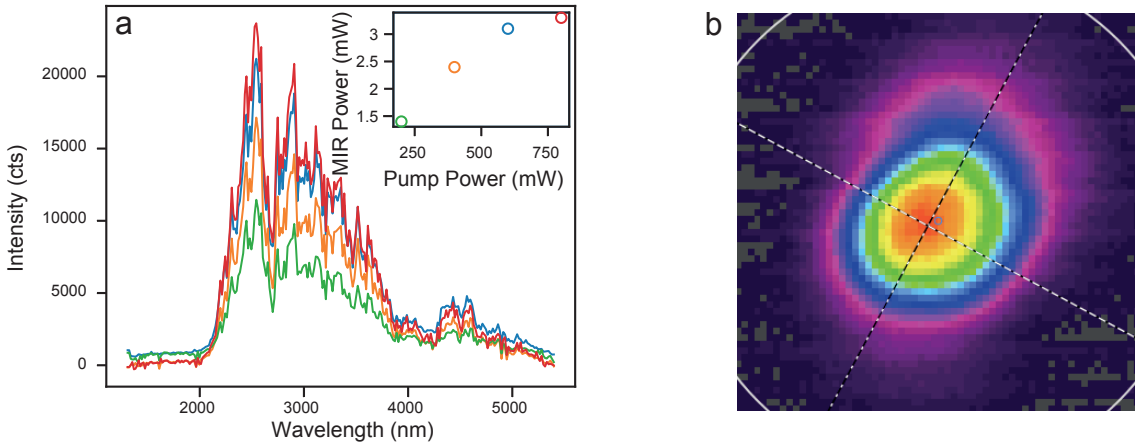

Figure 5.19: **MIR Generation:** (**a**) Measured MIR spectrum as a function of pump power, with the pump power values color-coded with the inset. The inset shows the average power of the MIR output as a function of pump power. (**b**) MIR far-field beam profile measured with a Pyrocam IIIHR (Ophir Spiricon), major axis = 3.4 mm (D4σ), minor axis = 2.7 mm (D4σ).

wavelength of the NOPA output can be shifted, resulting in MIR output spectra ranging from 2 µm to 3.5 µm, shown in Fig. 5.8. The results Experimentally, the most compressible spectrum was found to have a central wavelength of 2.7 µm, as described in the chapter 5.1.

Alignment

Before alignment the crystal temperature is set to 38 °C to avoid photo-refractive damage [53], furthermore the precise temperature was not found to be critical for phase-matching. The ADFG stage alignment strategy is to first align the pump beam through the two irises, before and after the crystal. As different angles of the pump through the ADFG crystal affect the effective dispersion generated, extra care is needed for precise alignment. After the pump beam is set, it should not be changed. When the temporal overlap is not known, the pump position dependent on the delay line position should also be checked to avoid position changes when the delay is changed. The next step is to align the seed beam with the pump, either aligned to the irises

or by removing the ADFG crystal and using a camera moving between two positions before and after the crystal position. When the two beams are collinear, the MIR output power should be measured and the pump power should be set at a moderate value of $\sim$500 mW. To find the temporal overlap either the MIR output power or visually the parasitic beam after the separator can be observed while scanning the delay line. When the temporal overlap is reached, the parasitic beam will turn blue, or the MIR output power will become detectable. The next step is to optimize the alignment by beam walking the last two mirrors of the seed beam before the ADFG crystal to increase the MIR average power. In addition, the fine-tuning of the temporal overlap can be optimized by moving the motorized retro reflector of the pump beam stretcher. As a final step in the optimization procedure, Pyrocam IIIHR is placed in the MIR beam path, and the seed alignment is optimized for a round and homogeneous beam profile. An additional check to gauge the alignment is to measure the MIR spectrum and make sure that the generated spectrum matches the NIR input spectrum in bandwidth.

5.3 Mid-Infrared Spectral Phase Characterization Techniques

When measuring the spectral phase of an optical pulse many techniques are available, such as interferometric autocorrelation, frequency-resolved optical gating (FROG), cross-correlation frequency-resolved optical gating (XFROG), dispersion scan (d-Scan), spectral phase interferometry for direct electric field reconstruction (SPIDER), and two-dimensional spectral shearing interferometry (2DSI). For the mid-infrared, all of these techniques have potential applications and can be used for the general purpose of spectral phase measurements. Nevertheless, when dealing with fully unknown pulses in the mid-infrared, there are obstacles to be overcome. First of all, the optical alignment of mid-infrared setups can be difficult, due to the worse detection sensitivity of the beam with mid-infrared sensitive detector cards. Spectrometers in the mid-infrared are less sensitive and are less commonly available compared to their near-infrared counterparts based on Si detectors. Furthermore, in the context of this thesis, the pulse energies are in the nanojoule level, the average power is only on the order of a few milliwatts, and the first iteration of the dispersion management resulted in a few hundred femtosecond pulse durations. Therefore, the techniques chosen for this particular characterization case are XFROG and 2DSI, since both techniques use the pump pulses of the laser source to up-convert the mid-infrared signal into the NIR, which is detectable by Si-based spectrometers, and also allow one fully up-convert the Mid-IR signal to the Near-IR/visible detection region thanks to a much more intense pump pulse. This is practically the ADFG time-reversed process. In particular, the XFROG has proven a useful tool for estimating the dispersion of the system with a broadband signal of unknown and highly chirped dispersion. Direct visual feedback allows optimization of the pulse compression from a single scan without the need for reconstruction algorithms, general projection principal components analysis (PCGPA), or ptychographic methods [117, 118]. In addition, the stretched pulse under test can have a maximum pulse duration only lim-

ited by the scan range of the gate pulse in time. However, the minimum temporal resolution of XFROG is severely limited by the gate pulse duration. In contrast, the 2DSI is better suited for close-to-compressed few to single-cycle pulses, due to the high temporal resolution of the interferometric approach and the independence of phase matching within the nonlinear medium, as long as any up-converted signal is detected (see details in Section 5.3.2) [91, 110]. While having a high temporal resolution, it suffers from a limited spectral resolution, effectively giving an upper bound for pulse durations to be characterized [110]. Together, these two techniques allow us to produce complementary information when characterizing unknown optical pulses.

5.3.1 Cross-Correlation Frequency Resolved Optical Gating

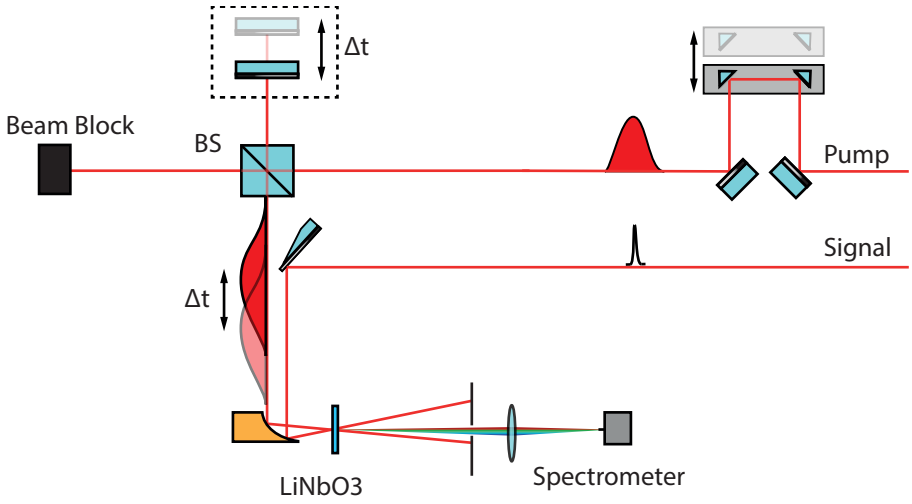

Figure 5.20: **Sketch of the XFROG Setup:** XFROG setup with two input beams referenced as pump and signal. BS: Beamsplitter.

Cross-Correlation FROG is an adaptation of the self-referenced FROG method. It uses a known gate pulse $E_{Gate}(t)$, like in most cases a well-characterized pulse from a pump laser, to characterize an unknown second pulse $E_{Signal}(t)$. Identical to FROG, the two pulses generate a third pulse through non-collinear sum frequency generation in a $\chi^{(2)}$ material, which is then spectrally resolved and recorded as a function of delay τ between the two pulses [119],

$$I_{XFROG}(\omega,\tau) = \int_{\infty}^{\infty} \left| E_{Signal}(t) \cdot E_{Gate}(t-\tau) \exp\{-i\omega t\} \right|^2 . \tag{5.3}$$

The experimental setup, as shown in Fig. 5.20, uses up to 10 mW of the 420 fs pump laser with a central wavelength of 1.03 µm. The pump beam arrival time is matched by a long-range dovetail delay line to the MIR signal to within 1 cm to 2 cm. For the femtosecond level delay tuning the pump beam is sent into a Michelson interferometer with a slip-stick piezo stage (SLC-2460 R-S, Smaract GmbH) in one arm and a beam block in the other arm. The interferometer, which is not necessary for an XFROG setup, will be necessary later for the 2DSI measurments; see details in Section 5.3.2. For up-conversion of the signal pulse, the gate pulse and the signal are

focused by a 1-inch diameter off-axis parabola with a focal length of 5 cm. The nonlinear crystal is a 10 µm thick 5 % magnesium oxide (MgO) doped lithium niobate crystal (MgO:$LiNbO_3$) cut at 44° for type 1 phase matching. After the nonlinear crystal the gate and the signal are spatially filtered by an iris and the up-converted signal is reimaged by a 5 cm focal length convex calcium fluoride lense into a spectrometer (Ocean Optics Flame-T NIR spectrometer). The resulting spectra as a function of the delay between the pump and the signal are shown in Fig. 5.21 b. The measurement shows the instantaneous wavelength distribution of the MIR signal

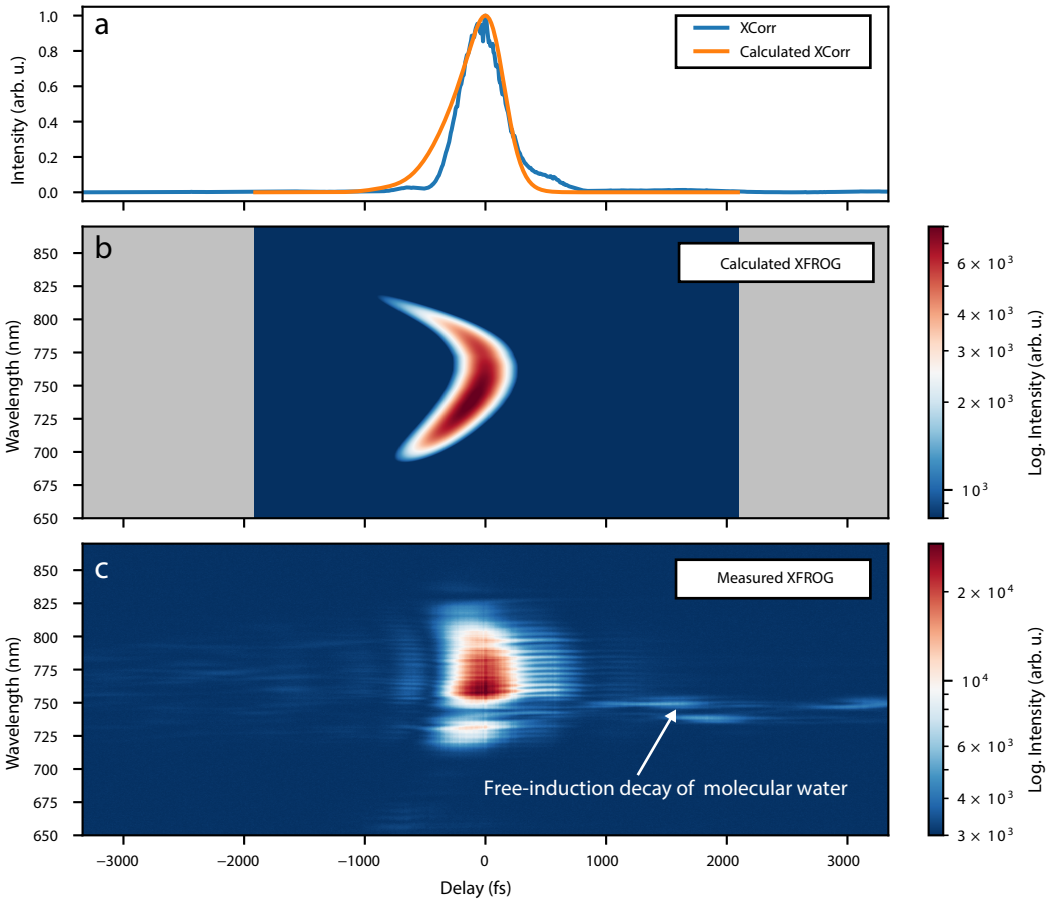

Figure 5.21: **XFROG Measurement Results Compared Against Calculation:** XFROG measurement compared to XFROG calculated from total system dispersion by neglecting phase-matching effects from the ADFG downconversion and XFROG upconversion. **a**) Comparison of the cross-correlation traces for the measured and the calculated case, derived from the spectrally resolved XFROG. **b**) Calculated XFROG trace. The grey areas on the sides of the trace mark the edges of the calculation. **c**) Measured XFROG trace. The annotation shows a signal delayed relative to the main pulse arrival time, associated with the free-induction decay of molecular water.

convoluted with the gate pulse, as intuitively the 420 fs gate pulse only up-converts wavelength components that it temporally coincides with. Without using a reconstruction algorithm one can see that the signal is dominated by third-order dispersion since both the short- and the long-wavelength components arrive earlier in time. A chirp, on the other hand, would correspond

to a linear diagonal distribution in time with, for example, long wavelengths arriving first in time and short wavelengths last. Another immediately apparent aspect of the measurement is the missing spectral component around 740 nm, corresponding to the original MIR wavelength of 2630 nm, $\lambda_{MIR} = \frac{1}{\frac{1}{740\text{nm}} - \frac{1}{\lambda_{Gate}}}$. In this wavelength range, there are many known molecular water absorption lines, which are excited during the propagation of the pulse in the air and radiate at later times [111, 120]. Therefore, these spectral components can be attributed to the free -induction decay of molecular water. For the compression of ultrashort pulses, these narrowband absorption lines have no imminent effect, despite scattering out spectral components that will deteriorate the average power of the MIR pulse, as they are narrowband in frequency and therefore are long lifetime features in the time domain, mainly causing a trailing pedestal. However, many absorption lines will have a cumulative effect on the refractive index below or above the absorption line, yet it was not observed to play a significant role for the compression of the MIR pulse presented here.

To understand if the measured XFROG trace is similar to what could be expected of the total system dispersion, we calculated the accumulated group delay of the system, using the Sellmeier equations of all relevant material and tracking the optical pulse from the point of white light generation to the XFROG setup. As this was an intermediate snapshot of the dispersion of the system, it differs from the materials used in the final compressed stage, as presented in the chapter 5.1. The calculation result is shown in Fig. 5.21 a and b. When the calculated XFROG is compared with the measured trace, the clear third-order dispersion is also visible and matches the measurement qualitatively, indicating that the dispersion calculations are approximately correct and there are no unaccounted contributions to dispersion. With every FROG measurement, one can retrieve an autocorrelation measurement by integrating over the wavelength axis. The corresponding autocorrelation traces are shown in Fig. 5.21 a. In comparison, both autocorrelation traces have a similar FWHM, indicating a comparable pulse duration, though differing in the wings of the distribution. The calculated trace has a significant tail for negative delays, which corresponds to the overestimated third-order dispersion. The measured trace on the other hand has a pronounced shoulder on the positive delay side, which compared to the measured XFROG components seems to stem from the ghost image trailing the MIR pulse. The origin of this ghost image is not fully understood but could be attributed to several effects. As can be seen, the ghost image has clear spectral interference fringes, strongly indicating that a delayed replica of the MIR pulse is the origin. However, considering the group velocity $c/2.27$ (at 2700 nm) in $LiNbO_3$ and the crystal thickness of 20 µm, the calculated delay would be ∼150 fs, incompatible with the ghost image appearing around ∼600 fs. Therefore, it may be of a different origin or cause and further investigation is warranted. Despite the peculiarity in the XFROG results, the objective of the measurement was to verify that the assumptions used for the prediction of the dispersion of the system are approximately correct to implement the full compression.

5.3.2 Two-Dimensional Spectral Shearing Interferometry

Two-Dimensional spectral shearing interferometry (2DSI) is an essential tool for the characterization of close to single-cycle optical pulses, as it allows to direct measurement of the group delay of octave-spanning pulses [91, 110]. Similarly to SPIDER, it is not affected by inhomogeneous phase matching of the nonlinear process, as the group delay is directly encoded in a spectral fringe pattern [110]. To overcome the strong dependence of SPIDER measurements on the shear frequency, 2DSI encodes the fringe pattern not along the wavelength axis, but in a 2D trace where a relative phase among the two ancillary pulses is scanned. In 2DSI the optical pulse under test $\tilde{E}_{Signal}(\omega')$ is ideally upconverted by two pure frequencies ω_1, ω_2, referenced here as ancillaries, with the shear frequency defined as $\Omega = \omega_1 - \omega_2$. The ancillaries produce consequentially two upconverted spectra $\tilde{E}_{Signal}(\omega' + \omega_1)$ and $\tilde{E}_{Signal}(\omega' + \omega_2)$, with the transformed frequency axis defined as $\omega = \omega_1 + \omega'$. When the ancillaries are collinear, the upconverted spectra will interfere exclusively depending on the relative phase delay φ between the two ancillaries. This interference $I(\omega, \varphi)$ is then recorded in a spectrometer as a function of φ,

$$I(\omega,\varphi) = \left|\tilde{E}_{Signal}(\omega) + E_{Signal}(\omega-\Omega)e^{-i\varphi}\right|^2 \tag{5.4}$$

$$I(\omega,\varphi) = 2\ \left|\tilde{E}_{Signal}(\omega)\tilde{E}_{Signal}(\omega-\Omega)\right|\ \cos\left(\varphi + \phi(\omega) - \phi(\omega-\Omega)\right) + D.C.\ , \tag{5.5}$$

with $\phi(\omega)$ denoting the spectral phase of $\tilde{E}_{Signal}(\omega)$, [121]. Here, the benefit of 2DSI is immediately seen, since $\phi(\omega) - \phi(\omega-\Omega)$ is the finite difference, which is directly related to the group delay τ_g with $\tau_g = \frac{\phi(\omega)-\phi(\omega-\Omega)}{\Omega} + \mathrm{O}(\Omega^2)$. This means that the group delay is read directly from the fringe phase of the 2DSI trace and does not even require a calibration of the phase delay as long as it is sufficiently linear across the scan range.

For the experimental implementation of 2DSI, the XFROG setup (see Fig. 5.20) is used as a starting point. In the same way, the 1.03 µm pump laser is used for the generation of the ancillaries by sending it into a Michelson interferometer with a 25 mm BK7 beamsplitter cube and two narrowband line filters in each arm (Semrock, 1030nm MaxLine Laser Clean-Up Filter, with a center wavelength of 1030 nm and bandwidth of $\Delta\lambda$ =3.9 nm). The line filters can be used to select specific frequencies for the ancillaries by rotating along their vertical axis to fine-tune their individual center wavelengths. As Ω sets the spectral resolution of the 2DSI measurement, it also sets an upper boundary for the observable time window T related to Ω with $T = 2\pi/\Omega$, and all components outside of that window are effectively aliased back into the time domain [110]. Therefore, it has to be chosen carefully, specifically when dealing with narrowband spectral features such as absorption lines or satellite pulses with longer temporal delays. The effective shear frequency for this case is set to Ω =1.4 THz (T =740 fs), measured with an optical spectrum analyzer. A recorded unprocessed 2DSI trace is shown in Fig. 5.23. Taking into account equation 5.5, the recorded trace shows a visible change in the phase of the

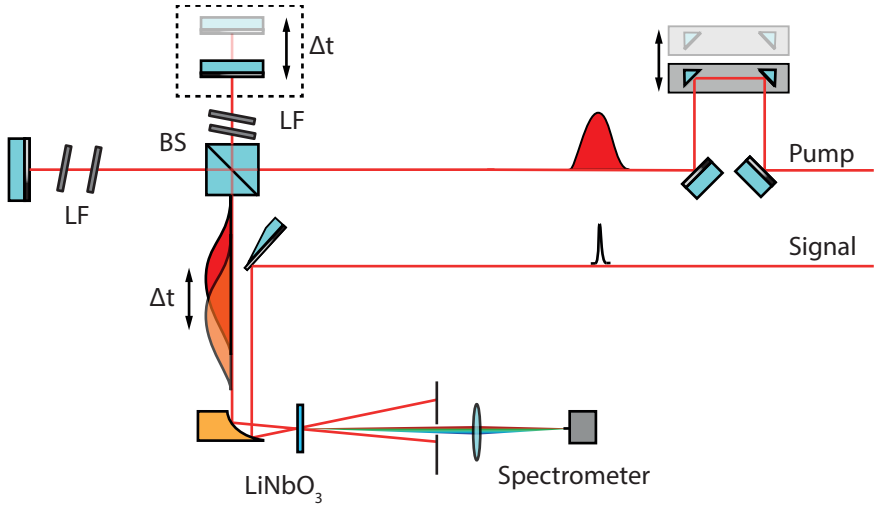

Figure 5.22: **Sketch of the 2DSI setup:** 2DSI setup with two input beams referenced as pump and signal. BS: Beamsplitter. LF: Line filter.

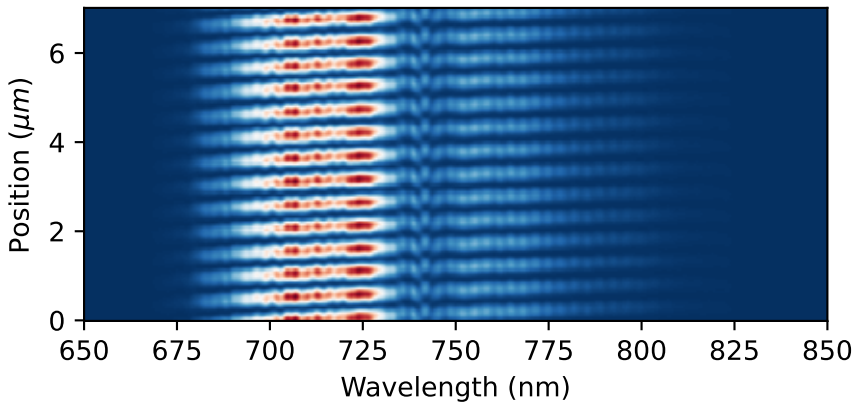

Figure 5.23: **Raw 2DSI Measurement:** Raw 2DSI measurement of a typical pulse with 2 mm of silicon inserted into the beam path. The color-coded image (red marks high values and blue low values) shows raw counts on a spectrometer as a function of wavelength and position of the delay stage.

fringes as a function of wavelength. Another visible feature of the measurement is the sharp oscillation of intensity along the wavelength axis, which we attribute to an etalon effect of the 10 µm thick crystal. As the fringe phase is proportional to the group delay, we can immediately see that there is second-order and higher-order dispersion on the measured pulse. Intuitively, a linear change in phase is caused by a second-order dispersion, and a monotonic curvature is caused by a third-order dispersion. With this visual feedback, one can already use the measured 2DSI trace to optimize the pulse compression by trying to create fringes as flat as possible.
However, for the reconstruction of the optical pulse, the trace needs to be analyzed quantitatively. To obtain an accurate measurement of the group delay, a few technical details have to be considered. The group delay approximation $\tau_g = \frac{\phi(\omega)-\phi(\omega-\Omega)}{\Omega} + \mathrm{O}(\Omega^2)$ using the finite difference is error-prone, scaling with $\mathrm{O}(\Omega^2)$, and causing inaccurate representation of satel-

lite pulses [110]. A better strategy is inversion of the finite difference operation by resampling the data exactly at the shear frequency Ω [110]. This results in $\tau_g(n) = \frac{\phi(n\cdot\Omega)-\phi(n\cdot\Omega-\Omega)}{\Omega}$, with $n = 0,1,2,\ldots$, becoming the exact derivative. However, to avoid aliasing of fast group delay oscillations, the frequency axis should first be low-pass filtered at Ω. In Fig. 5.24, a zoom-in to

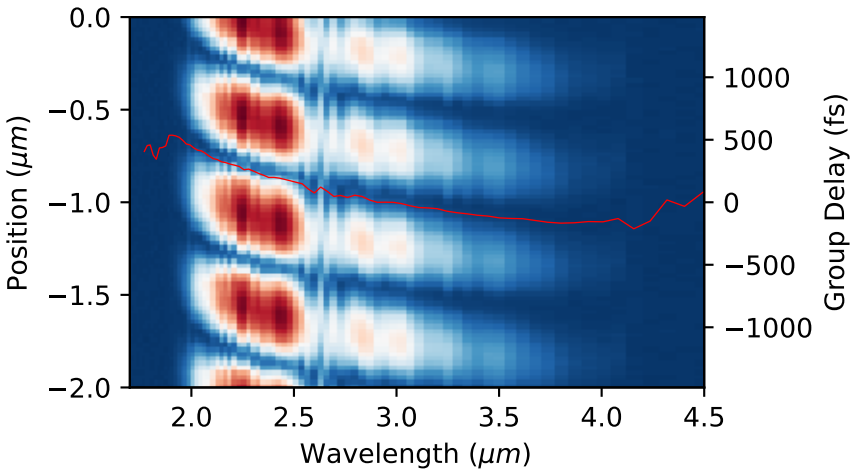

Figure 5.24: **Processed 2DSI Trace:** Processed 2DSI trace with logarithmic color coding and the group delay in red proportionally scaled to the fringe phase. The trace is processed with low-pass filtering and resampling at 1.4 THz. 2 mm of silicon are inserted into the beam path to demonstrate the measurement principle.

5 fringes of a processed 2DSI trace is shown. The trace is low-pass filtered with a second-order Butterworth filter with a cut-off frequency of 1.4 THz and resampled at the same frequency. The resulting group delay is shown as a red overlay plot and scales with the throw of the fringe pattern. To benchmark measurement accuracy, measurements with and without 2 mm of silicon are compared in Fig. 5.25. In blue, the group delay calculated from the Sellmeier equation of silicon is shown [122], whereas orange and green show two 2DSI measurements with and without silicon. It is directly visible that the measured group delay well approximates the calculated group delay. To quantify the error of the measurement, Fig. 5.26 shows the difference between the two measurements and compares it against the calculated values. Across the measurement range from 2 µm to 4 µm the calculated error is 5.3 fs rms. Further, it can be seen that the error rises sharply at the edges of the spectrum of the pulses, caused by the insufficient optical intensity in the measurement. By measuring the group delay of a known material, the effective shear frequency Ω can be also calibrated by optimizing for the lowest measurement error, compared to relying fully on the measurement of the ancillaries with an optical spectrum analyzer. As an illustrative example, a measurement with a shear frequency off by +10 % is shown in the red dashed line.

With the uncertainty of the group delay measurement in mind, it is possible to also assess the influence on the reconstructed time domain of the optical pulse. For that purpose, the electric field is reconstructed 100 times, by adding randomly generated white noise with a standard deviation

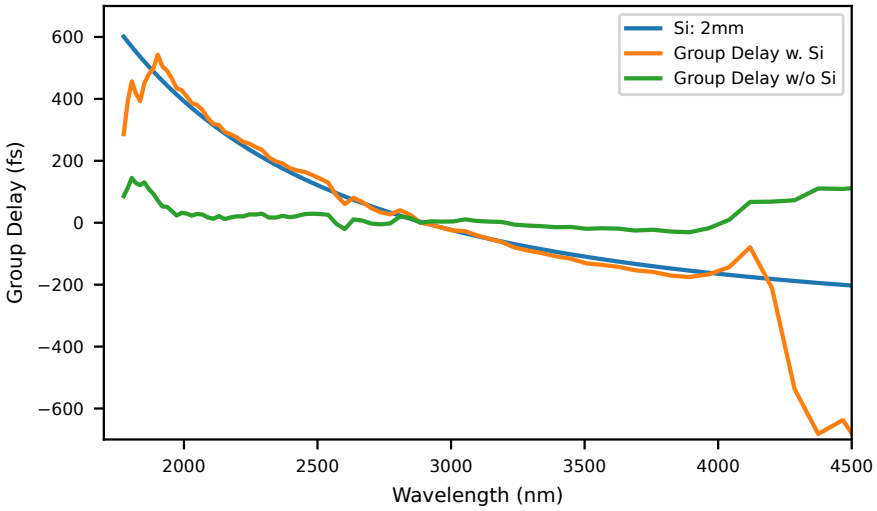

Figure 5.25: **Group Delay Reference Measurement:** Calibration of the 2DSI measurement by comparing two measurements with 2 mm of silicon (orange) and without (green). In blue, the group delay of 2 mm thick silicon, calculated from the Sellmeier equation, is shown [122].

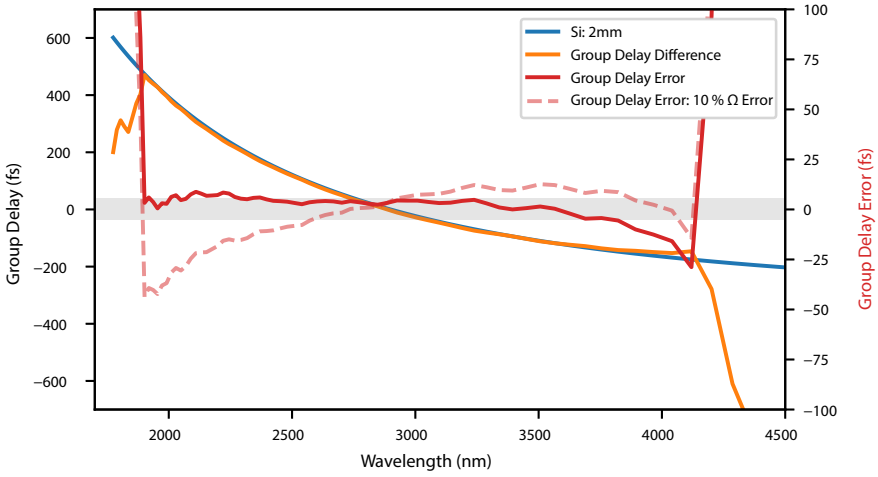

Figure 5.26: **Group Delay Error Estimation:** Retrieved silicon group delay versus the calculated group delay. The error between the calculation and retrieved values is shown in red. For illustration, a group delay error for the case of the shear frequency 10 % to large, red dashed line.

of 5.3 fs to the group delay for each individual reconstruction. With these measurements, the average electric field value as a function of time and the respective standard deviation can be defined. The result of such an analysis is shown in Fig. 5.27, with a retrieved pulse duration of 18.4 fs ±5.6 fs. However, assuming white noise of 5.3 fs rms for the group delay, is most likely not a correct assumption, since the nature of the measured error is not fully understood yet. It can, of course, be pure Gaussian measurement uncertainty or more probably a systematic and reproducible error caused for example by using ancillaries that are not ideal CW waves, not

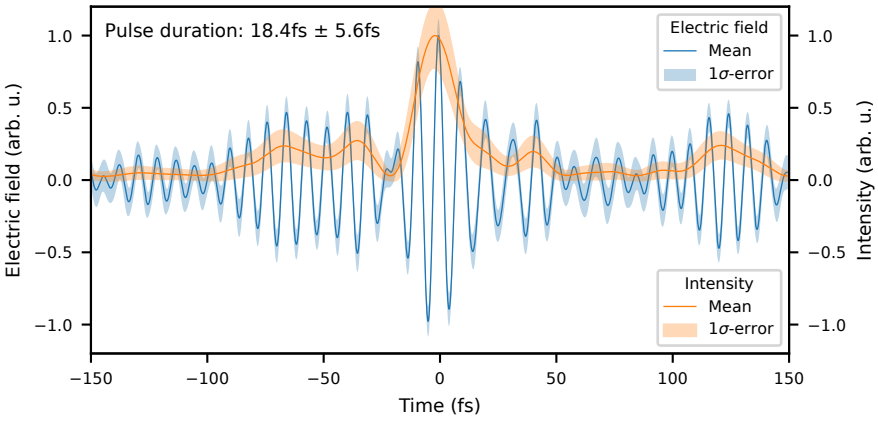

Figure 5.27: **Calibrated Pulse Retrieval Results:** Retrieved electric field and intensity profile of the optical pulse under the assumption of a group delay measurement error with 5.3 fs rms. The measurement error is retrieved from the silicon reference measurement, see Fig. 5.26.

perfect collinearity of two ancillary beam paths or not accurate Sellmeier equations describing the reference material. When for example, comparing two consecutive measurements without changing any parameters, the group delay uncertainty was found to be 1.8 fs rms. When doing the identical analysis to the above, the measured pulse duration error is reduced 0.7 fs, as seen in Fig. 5.28. It should be emphasized, that both analyses rely on two measurements each, which by no means gives accurate statistics and should be considered as a demonstration of how to approach quantitative pulse retrieval with measurement errors.

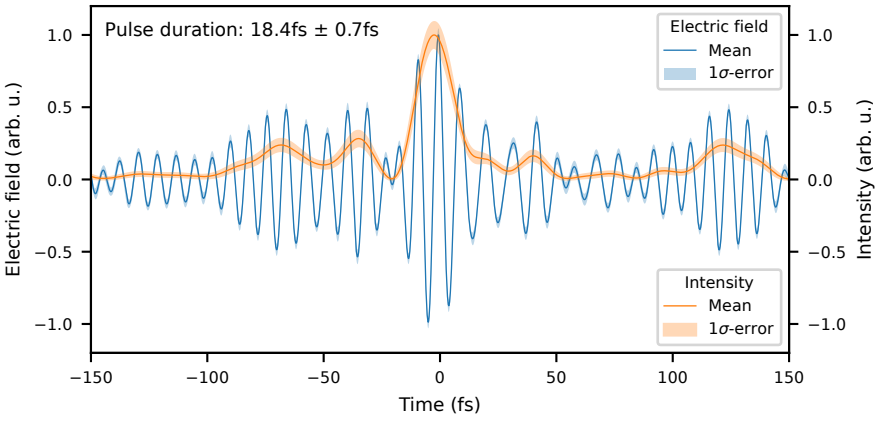

Figure 5.28: **Pulse Retrieval with Measurement Uncertainty:** Retrieved electric field and intensity profile of the optical pulse under the assumption of a group delay measurement error with 1.8 fs rms. The measurement error is retrieved from two consecutive measurements.

In conclusion, this chapter presents a complete toolkit for spectral phase retrieval techniques in the MIR, from the characterization of long highly chirped pulses by means of XFROG to an

approach for quantitative measurements of compressed 2-cycle pulses. Specifically, the quantitative analysis of errors in 2DSI measurements is a helpful tool to understand the complex field-driven nonlinear phenomena like electron emission, extensively discussed in this thesis. However, more research is needed to investigate the origin and nature of these errors. One approach could be the analysis of many consecutive 2DSI measurements, to get improved statistics, or comparisons between different material species and thicknesses.

5.3.3 Dispersion Management Strategy

As the previous section discussed the characterization of the spectral phase of MIR pulses, this section explains the underlying concept of dispersion management of the laser system and how compression of the optical pulse is optimized. One of the big advantages of adiabatic difference frequency generation is the linear spectral amplitude and phase transfer function from the NIR input to the MIR output. That is, the input group delay $\tau_{NIR}(\omega)$ of the NIR pulse is transferred to the MIR group delay τ_{out} regardless of the input energy or the spectral amplitude with the relationship [22, 53, 123],

$$\tau_{out}(\omega) = \tau_{NIR}(\omega - \omega_{pump}) + \tau_{ADFG}(\omega), \tag{5.6}$$

where $\tau_{ADFG}(\omega)$ is the contribution of the adiabatic frequency conversion. This means that by carefully choosing specific sets of material before and after the ADFG stage, we can compensate for the dispersion contribution of the ADFG device and the dispersion overall. Therefore, the total dispersion of the system is described by

$$\tau_{Total}(\omega) = \tau_{NIR}(\omega - \omega_{pump}) + \tau_{ADFG}(\omega) + \tau_{MIR}(\omega), \tag{5.7}$$

with $\tau_{MIR}(\omega)$ denoting the group delay acquired after the ADFG stage. Therefore, by choosing materials with the right dispersion properties, the large third-order dispersion of the ADFG stage and the residual chirp can be fully compensated. Naturally, this can be solved fully algebraically, when considering the Taylor expansions of the group delay contributions around the central frequency ω_0,

$$\begin{aligned} \tau'_{Total}(\omega_0) &= \tau'_{NIR}(\omega_0) + \tau'_{ADFG}(\omega_0) + \tau'_{MIR}(\omega_0) \\ \tau''_{Total}(\omega_0) &= \tau''_{NIR}(\omega_0) + \tau''_{ADFG}(\omega_0) + \tau''_{MIR}(\omega_0). \end{aligned} \tag{5.8}$$

However, this neglects existing higher-order dispersion components of the system and does not necessarily yield the shortest possible pulses. To achieve the shortest possible pulses, it is practical to make the assumption that the shortest possible pulse has the highest peak power and therefore to numerically optimize the group delay by optimizing two different material

thicknesses x, y on the NIR and MIR sides for the highest peak power of the output pulse,

$$\begin{aligned}\tau_{Total}(\omega,x,y) = &\tau_1(\omega,x) + \tau_2(\omega,y) + \\ &\tau_{NIR}(\omega-\omega_{pump}) + \tau_{ADFG}(\omega) + \tau_{MIR}(\omega).\end{aligned} \tag{5.9}$$

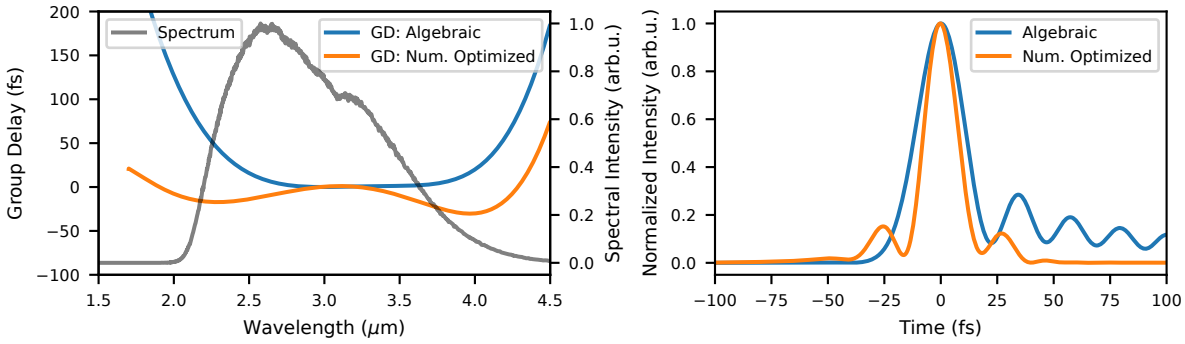

Figure 5.29: **Compression Optimization Strategy: (Left)** Optimized group delays as a function of wavelength for the algebraic and numerical optimization strategies and the spectrum used for the optimization. **(Right)** Normalized intensity as a function of time for the group delays and the spectral distribution shown on the left. Algebraic Strategy: 24 fs FHWM duration; Numerically Optimized Strategy: 16.5 fs FHWM duration.

To highlight the differences between these two compression strategies, Fig. 5.29, shows a theoretical comparison of the algebraically calculated and the numerically optimized group delays. Both sets used BaF2 on the MIR side and SF-10 on the NIR side to compensate for the dispersion of all other materials in the laser system and the ADFG device. The group delay of the algebraic solution is optimized for a central wavelength of 3 µm. As can be seen in Fig. 5.29 the two group delays differ in the way that the algebraic solution is perfectly flat for a range of 2.5 µm to 4 µm but is not able to cover the full spectrum. The numerical solution is able to cover a larger bandwidth, but with a small oscillation causing satellite pulses. When calculating the temporal intensity distribution of these two strategies, the algebraic solutions yield a 24 fs FHWM duration pulse, whereas the numerical optimization achieves a 16.5 fs FHWM duration pulse. Of course, this analysis is highly dependent on the bandwidth of the optical pulse. As can be seen immediately for narrowband pulses the algebraic solution is viable and the numerical optimization would most likely yield the same result. However, the numerical optimization strategy yields the best results for the octave-spanning pulse discussed in this thesis. The individual group delays contributions on the NIR, the ADFG device, and the MIR side of the final system configuration are shown in Fig. 5.30. The list of materials underlying the group delay calculation is shown in table 5.1.

As these are pure analytical calculations neglecting all nonlinear phase contributions, the group delay of the system needs to be experimentally verified. The total group delay is measured with 2DSI and compared against the calculated group delay above. The results, shown in Fig. 5.31,

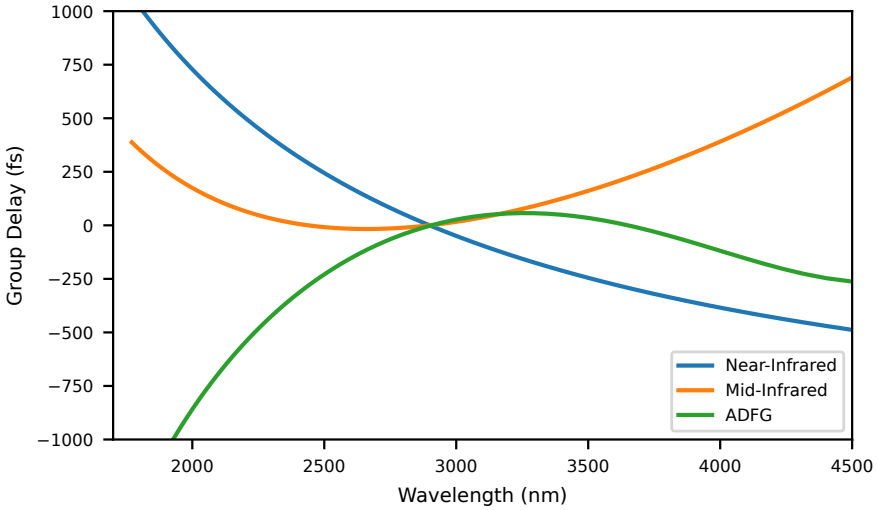

Figure 5.30: **Dispersion Design:** Group delay as a function of wavelength for the three major dispersion components of the laser system. The near-infrared contribution accounts for all group delays acquired before the ADFG stage. The effective ADFG group delay. The mid-infrared group delay was acquired after the ADFG stage.

match very well the a priori assumed dispersion. The measured group delay deviates from the expected group delay by a group delay dispersion of $-8\,\mathrm{fs}^2$. After accounting for the residual chirp and an offset of 21 fs, the calculated group delay matches the measured one for the largest part of the spectrum. Nevertheless, above wavelengths of 3.5 µm the measured group is larger than the calculated values. This behavior could be attributed to the known error of the 2DSI measurement itself, as discussed in chapter 5.3.2.

When optimizing the dispersion of the system close to the maximum compression point, the group delay needs to be measured with the 2DSI to account for any uncertainties in the group delay. With this starting point the compression optimization described above can be used again to find a combination of BaF_2 and H-ZF12 material to further compress the pulse. Another

Material	Thickness in mm	NIR/MIR side
YAG	4	NIR
SiO_2	4	NIR
H-ZF12	~ 7.5	NIR
BBO ord. axis	1.5	NIR
BK7	3	NIR
Si	2	MIR
BaF_2	39	MIR
CaF_2	3	MIR

Table 5.1: **List of relevant Materials** List of all materials in the optical beam path starting from the white light generation. The H-ZF12 consists of 4 mm of bulk material and a tunable 5 ± 2 mm wedge pair.

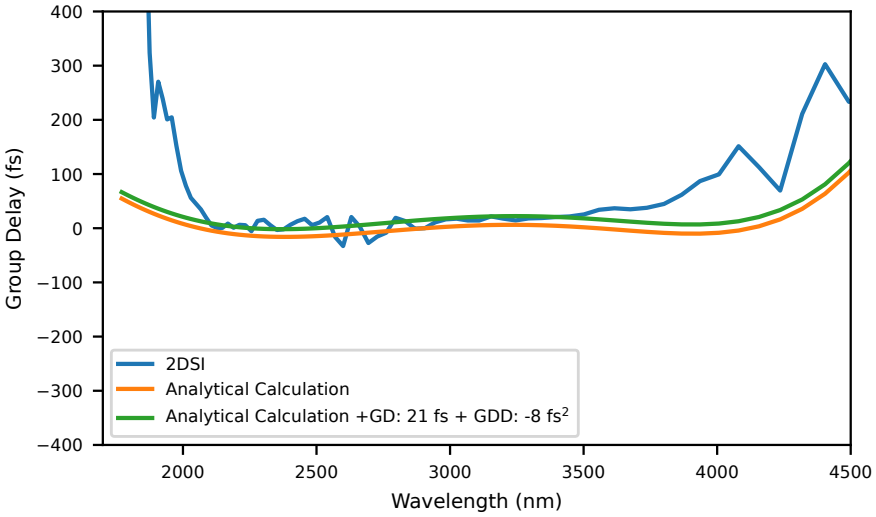

Figure 5.31: **Dispersion Analysis:** The 2DSI group delay measured compared to the analytical group delay calculation, assuming all relevant materials inside the system.

strategy can be the calculation of the compression topology around the measured pulse duration. By creating a 2D map of the pulse's peak intensity $I_{peak}(x,y)$ normalized to the starting pulse at (0 mm,0 mm) as a function of material thickness one can find the global maximum of the peak intensity. The results of such a calculation are shown in Fig. 5.32. The global maximum is found at (-2 mm,0 mm), meaning that the amount of inserted BaF_2 needs to be reduced by 2 mm. From the topology map can also be learned that when utilizing optimization algorithms these should be more refined than gradient ascent methods, which would be prone to optimizing for a local maximum. Therefore, methods like the differential evolution algorithms that do not rely on gradient methods have been shown to be useful in predicting optimal compression material combinations[124, 125].

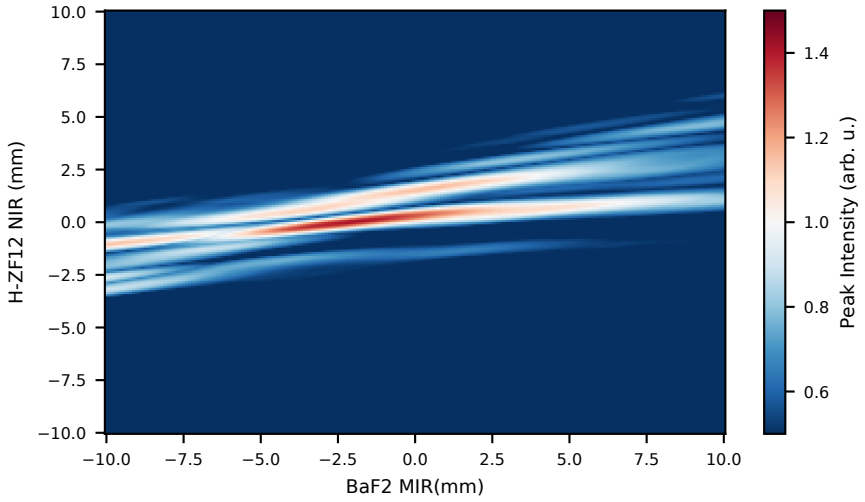

Figure 5.32: **Compression Topology:** Topology of peak intensity normalized to the starting pulse at (0,0) as a function of different material insertions on the NIR side with H-ZF12 and BaF_2 on the MIR side. The calculation uses an 18 fs slightly chirped MIR pulse measured with the 2DSI and Sellmeier equations of H-ZF12 and BaF2. The global maximum at (-2,0) yields a 16 fs duration pulse.

5.4 Concluding Remarks on the Source Development

The laser system presented achieves sub-2-cycle optical pulses at a center wavelength of 2.7 µm with 16 fs FWHM duration with passive CEP stability of $<$190 mrad rms and a pulse energy of 84 nJ at a repetition rate of 50 kHz. Close-to-transform limited compression is achieved solely through compression in bulk materials, adding to the inherent stability of the system. This system demonstrates the benefits of ADFG and the precisely predictable dispersion of the system. This system has many properties exceptionally beneficial for field-driven nanophotonic experiments, as, for example, studied in this thesis.

The main drawback of the employed MIR generation scheme is the low of output pulse energy, compared to other OPA-based generation schemes. This stems from the change in the role of the pump and seed in the ADFG conversion process compared to an OPA. Due to the seed being the pulse with the highest photon energy, the seed photons of $\sim$2 µJ provide effective parametric gain to the strong pump and idler. Of course, this can provide theoretical 100 % photon conversion efficiency from seed to idler, but the total energy efficiency considering the pump energy 20 µJ is comparably low. However, when energy efficiency is not of concern, this technique allows for close to single-cycle pulse generation as shown by Krogen et al. [53].

To achieve a microjoule-level output energy with the system presented in this thesis, the NOPA stage should be further amplified to $\sim$30 µJ with a second stage. Another avenue for improvement is the dispersion design of this system. With the knowledge of the very predictable dispersion from the ADFG device, custom chirped mirrors can be designed that pre-compensate

on the NIR side the dispersion of the ADFG stage and a larger block of material on the MIR side. This would allow for the achievement of single-cycle pulses with a minimum amount of satellites or higher-order dispersion. This approach to dispersion control also alleviates the usual problem that it is hard to design more than octave-spanning chirped mirrors, as the mirrors would be employed on the not yet octave-spanning NIR side. Another interesting possibility is to explore with this system intrapulse difference frequency generation in a $ZnGeP_2$ crystal that has shown the generation of single-cycle pulses at a wavelength of 7 µm, enabling continuous spectral coverage from 2 µm to 10 µm [126].

In conclusion, such a system with a high repetition rate and single-cycle pulses of microjoule level in the MIR and the possible extension deeper into the IR would have many interesting applications in the context of this thesis. Larger area nanoantenna detector arrays approaching the macroscopic size of 100 µm could be investigated or attosecond resolution field sampling covering the entire MIR region could be demonstrated.

6 Large Scale Optical Frequency Electronics

6.1 Introduction

[1]Attosecond science demonstrated that electrons can be controlled on the sub-cycle time scale of an optical wave, paving the way toward optical frequency electronics[4]. Using controlled few-cycle optical waveforms with microjoules of energy, the study of sub-cycle electron emission was critically enabled and demonstrated for example the generation of attosecond short ultraviolet pulses or the control of attosecond currents inside of solids. However, these experiments rely on high energy laser pulses and test systems not suitable for integration in microcircuit elements. Therefore, to move towards integrated optical frequency electronics, a system suitable for integration into microcircuits and generating detectable signals with low pulse energies needs to be devised. We show that by using hundreds of interconnected plasmonic nanoantennas integrated in a microcircuit combined with a tailored sub-2-cycle mid-infrared waveform of only tens of nanojoules of energy, we can generate in excess of 2000 electrons sensitive to the carrier-envelope phase and detect these on a single shot basis. Compared to previous results [7–9, 23], we demonstrate that single-electron emission from an individual nanoantenna is not exclusive for MHz-level repetition rate sources, but is a fully scalable approach that can be engineered for kHz-level sources to drive hundreds of nanoantennas only limited by the available pulse energy. This shows that electronically integrated plasmonic nanoantennas are a viable approach to integrated optical frequency electronics. By engineering the nanoantenna to the particular use case and optimizing the density and total amount, the output signal type and strength are fully controlled. Furthermore, having a flexible approach to optical frequency electronics will enable many interesting applications, such as petahertz-bandwidth electric field sampling or the realization of logic gates operating at optical frequencies [20, 24].

When John A. Fleming developed the first widely usable vacuum diode based on the thermionic emission of electrons from a tungsten filament, later known as the Fleming valve, he sparked a revolution in the field of electronics [31]. By rectifying a fast oscillating voltage into a DC current with a nonlinear element, key technologies such as wireless signal transmission, high-frequency amplifiers, telecommunication and digital electronics became a reality. With the advent of the laser, the idea of converting optical frequencies at hundreds of terahertz into rectified direct current was developed. Through tunnel emission in cat whisker diodes, frequency rectification of up to 88 THz ($\lambda = 3.39\,\mu m$) was demonstrated and referenced against a known microwave frequency standard [40, 127]. Nevertheless, the optical and the microwave domains could not be coherently phase-locked due to a missing key technology: the optical frequency comb. Thirty years later this was realized for the first time and a self-referenced frequency comb with a stabilized carrier envelope (CE) offset frequency, coherently locked optical frequencies to the microwave domain [44]. Soon after, ultrabroadband carrier-envelope-phase (CEP) sta-

[1]This chapter is based on a manuscript currently in submission process. The author of this thesis is also the first author of this manuscript, among Matthew Yeung as a shared first shared author. The author was involved in conceiving the experiment, conducted the experiment, analysed the data and wrote the manuscript.

ble light pulses that carry only a few oscillations of the electric field were developed. This allowed to control the electron wavepacket propagation in atoms over the time scale of an optical cycle, ultimately leading to the generation of isolated attosecond pulses in the XUV to soft X-ray spectral region [1–3, 106, 128]. With these single- to few-cycle CEP-stable pulses, it was demonstrated experimentally that the electric field oscillation of the pulse can be rectified in solid matter to generate attosecond sub-cycle electron bursts on sharp metallic tips [7, 11].

Encouraged by these results, many ways were studied to generate femto- to attosecond currents directly in closed electric circuit elements by using sub-cycle interband transitions in dielectrics [12, 13, 129, 130], or field emission from gas phase atoms [16, 18], or metallic nanoantennas [8, 9]. The step to integrated circuits significantly reduced the experimental requirements from large and bulky vacuum equipment to in air operation and even allowed charge transport on the femtosecond time scale across nanometer-sized junctions[10]. Applications exploiting the subcycle nature of these currents have been demonstrated, for example attosecond resolution electric field measurements, CEP detection of few-cycle pulses and petahertz logic gates [8, 9, 13, 16, 18–20, 24, 25, 130, 131]. In addition, the use of resonant nanoantennas significantly reduces the energy requirement of the optical pulse by three orders of magnitude down to the picojoule level and confines the electron emission to a well-defined hotspot at the sharp tip of the nanoantenna [8, 9, 20, 23, 68]. Despite the experimental benefits, the electron yield from these nanoantennas is less than one electron per shot [8, 9, 20, 23], requiring the integration of thousands of individual laser shots for a statistically significant signal, limiting the applicability to high-repetition-rate laser sources. The ability to produce nanoantennas using lithographic techniques opens a route to overcome this limitation, since their design and interconnection can be easily customized. Yang et al. demonstrated the fabrication of large nanoantenna networks up to hundreds of interconnected nanoantennas. However, the available pulse energy allowed to operate only $\sim$10 antennas simultaneously, limiting the generated CEP dependent charges to $\sim$1 e^- per shot [23], hindering the possibility of measuring single-shot CEP variations. By scaling up the pulse energy, a higher number of antennas can be driven, yielding proportionally higher charges up to thousands of electrons per shot. A further yield increase is expected from using longer wavelength pulses that allows to emit a higher number of electrons per optical cycle. Furthermore, the CEP-dependent charge yield increases significantly by reducing the number of cycles in the optical pulse [23].

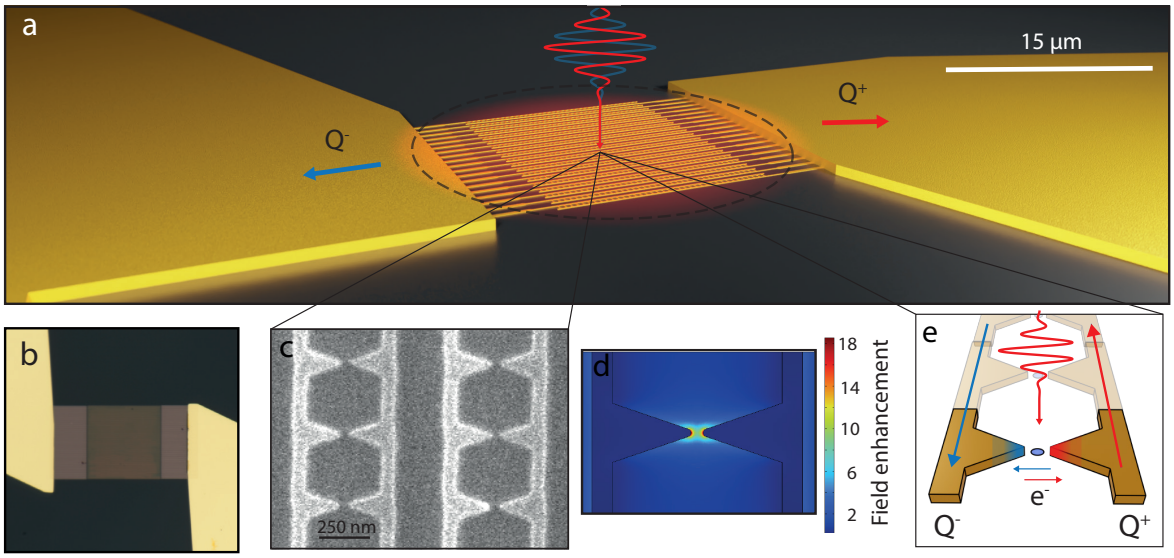

Figure 6.1: **CEP dependent charge generation Nanoantenna Arrays:** **a**) Schematic of the charge generation process in the network showing two electric field with a π phase shift corresponding to charge generated with positive Q^+ or negative sign Q^-. **b**) Optical microscope image of an integrated nanoantenna network contacted with gold leads. **c**) Scanning electron microscope image of a metallic nanoantenna array. **d**) Finite-element method simulation using COMSOL of the spatial field enhancement distribution of a single antenna pair. **e**) Schematic of the nanoscopic emission process, showing the sub-cycle electron currents generated in the antenna vacuum junction by the driving field.

6.2 Results and Discussion

We demonstrate the large-area generation of sub-cycle electron currents in metallic nanoantenna networks, producing in excess of 2000 electrons per shot, allowing for the detection of shot-to-shot changes of the CEP of the incident light at the full repetition rate of the laser system (50 kHz). Our devices, as seen in Fig. 6.1 a, consist of 722 interconnected metallic bow-tie nanoantennas embedded in a 15 µm by 15 µm network. The device is integrated into a macroscopic circuit, allowing for charge readout with conventional electronics. The individual bow-tie nanoantennas, as shown in the scanning electron microscope image in Fig. 6.1 c, have designed dimensions of 530 nm in length, 142 nm in width and 30 nm in thickness, resulting in an antenna density of $3.2\,\mu m^{-1}$. Fig. 6.1 d shows the finite element electromagnetic simulation of the field distribution, showing a peak enhancement of 18-fold for 3 µm wavelength localized at the tips of the bow-tie structure. This creates a spatially-confined hot spot for electron emission to occur. When the whole network is illuminated with a few-cycle infrared laser pulse with a peak electric field in the order of $1\,V\,nm^{-1}$, highly nonlinear tunnel ionization of electrons from the tips of the bow-tie antennas occurs. The tunnel ionization is confined to the peak regions of the strongest half-cycles of the exciting field. We can consider two cases: (i) An antenna gap size d smaller than the distance traveled by an electron during a half-cycle ($T/2$)

of the electric field, that is $d \ll x(T/2) = 2eE_0/m_e\omega^2$ where m_e is the electron mass and E_0 the electric field amplitude; (ii) A large gap where $d \gg x(T/2)$. For a small gap, a CW laser would lead to a fully symmetric charge injection and transport across the gap. In this case, the time average of the residual charge in the network is zero. In the case of a few- to single-cycle pulse, the highly nonlinear dependence of the tunnel emission with respect to the electric field amplitude does generate a residual net charge. This is caused by the significant amplitude differences between the individual half-cycles of the pulse, effectively breaking the symmetry of emission and transport. To understand the symmetry breaking, it is useful to look at the detailed instantaneous tunneling rates as a function of the electric fields for a metal-vacuum boundary. In the case of sufficiently strong electric fields, with a Keldysh parameter $\gamma \ll 1$ this can be described by the quasi-static Fowler-Nordheim tunneling rate $\Gamma_{FN}(E) \propto \theta(E)\alpha(E)^2 \exp\left(-\frac{f_t}{|E|}\right)$ [63, 66, 67, 69], with $\theta(E)$ noting the Heaviside function, f_t =78.7 V nm^{-1} the characteristic tunneling field strength for gold and α material and geometry dependent scaling factor. Since a single bow-tie is, in fact, a symmetric system consisting of two metal surfaces facing each other with a 50 nm vacuum gap, we can approximate the total instantaneous currents at the junction with $\Gamma(E) = \Gamma_{FN}(E) - \Gamma_{FN}(-E)$, as experimentally shown in [8, 10, 23].

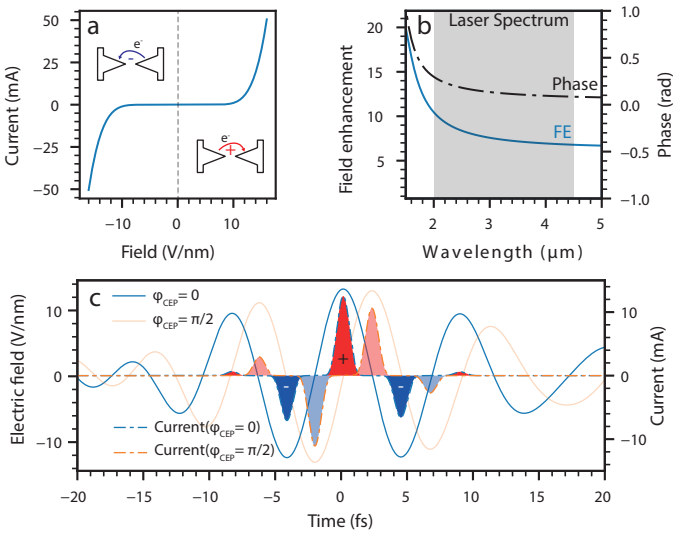

Figure 6.2: **Theoretical description of the antenna gap currents: a**, Effective instantaneous tunneling rate for two opposing gold surfaces in the nanoantenna junction, assuming scaling parameters from [23]. **b**, FEM simulated response function of the local electric field at the nanoantenna tip to an exciting electric fields showing the field enhancement and phase as a function wavelength. **c**, The electric field as a function of time and the instantaneous current as a function of the electric field for CEP of $\varphi = 0, \pi/2$. The solid lines note the electric field and the dashed lines the current. The shaded areas underneath the current curves show the total charge yield, with red areas contributing positively and blue areas contributing negatively.

The instantaneous response of this system, shown in Fig. 6.2 a, is equivalent to two parallel diodes in opposing directions. The scaling parameter is taken from the result in [23]. In the

calculation we assume a two-cycle optical pulse with a wavelength of λ =2.7 µm in the form of $E(t) = A(t) \cdot \cos(\omega_0 t + \varphi)$, with $A(t)$ as a gaussian pulse envelope, ω_0 the central frequency, and φ the CEP. As for the electron emission process the local field at the tip of the nanoantenna is relevant, we, in addition, need to consider its impulse response function[20]. The local field enhancement and the phase response of an off-resonantly designed antenna for wavelengths above 2 µm is shown in Fig. 6.2 b. The local field at the antenna tip $E_{\text{loc.}}$ is therefore the frequency domain multiplication of the incident pulse $\tilde{E}(\omega)$ and the antennas complex frequency response $\tilde{H}(\omega)$, $E_{loc.}(t) = \mathscr{F}^{-1}\{\tilde{E}(\omega) \cdot \tilde{H}(\omega)\}$. The effective instantaneous current response of the system to such a pulse with a peak field of $\sim$13 V nm^{-1} is shown in Fig. 6.2 c. The central half-cycle with the highest field amplitudes generates the largest peak current with up to 5 mA for a duration of 1.1 fs (FWHM). The neighboring half-cycles generate substantially smaller currents with the opposite sign. Since the macroscopic circuit system does not support the petahertz bandwidth currents, it acts as an integrator, and the net charge deposited by the optical pulse resides in the circuit network, similar to a photodiode. The mathematical description of these charges Q as a function of the pulse CEP φ is simply the integral over the instantaneous currents;

$$Q(\varphi) = \int_{-\infty}^{\infty} \Gamma(A(t) \cdot \cos(\omega_0 t + \varphi))\, \mathrm{dt} \tag{6.1}$$

$$Q(\varphi) = \int_{-\infty}^{\infty} \Gamma_{FN}(A(t) \cdot \cos(\omega_0 t + \varphi))\, \mathrm{dt} - \int_{-\infty}^{\infty} \Gamma_{FN}(-A(t) \cdot \cos(\omega_0 t + \varphi))\, \mathrm{dt}. \tag{6.2}$$

$$Q(\varphi) = Q^{+}(\varphi) - Q^{-}(\varphi) \tag{6.3}$$

The CEP dependence of the charge now stems from the small difference of $Q^{+}(\varphi)$ and $Q^{-}(\varphi)$. For the case of a cosine pulse ($\varphi = 0$) the charge yield becomes maximal, and for the case of a sine pulse ($\varphi = \pi/2$) the charge components cancel out to zero. Based on the results shown in [23] with 0.1 e per antenna, one can anticipate CEP dependent charge amplitudes of around 1.5 e^{-} per antenna for pulses with a central wavelength of 2.7 µm, a pulse duration of 18 fs and a peak field of 1.7 V nm^{-1}. For this case, the resulting charge increases from the previous results due to a reduced number of cycles from 2.5 to 2 and a longer wavelength [132]. With the known charge yield per antenna, one can extrapolate the charge yield of an array of interconnected antennas to a charge that is within the reach of reasonable detection limits. In order to generate a charge yield of at least 1000 e per shot, we designed a network consisting of 722 antennas in a rectangular area of 15 µm by 15 µm. The pulses used here are generated with laser source described in Chap. 5 based on optical parametric amplification and difference frequency generation that delivers passively CEP stable pulses with a FWHM duration down to 16 fs at a center wavelength of 2.7 µm. The pulse energy is >84 nJ at a repetition rate of 50 kHz. The CEP of the laser is controlled by adjusting the pump-seed delay in the difference frequency generation stage. This is implemented by controlling the bump beampath length via a retroreflector mounted on a piezo-actuated linear stage. For a detailed description of the source,

see Chap. 5.

To generate a CEP-sensitive charge in our network, we focus the incident pulse down to ∼21 µm (FWHM) with an off-axis parabola of focal length 25.4 mm. The nanoantenna array is placed in the center of the focus. We use a custom transimpedance amplifier with a gain of 1 GV A^{-1} and a −3 dB bandwidth of 50 kHz (WiredSense GmbH) connected to the nanoanntenna array to read out the charges accumulated on a shot-to-shot basis. After the pulse interacted with the nanoantenna array, its energy is measured by a pyroelectric photodetector with the same bandwidth of 50 kHz, that allows recording of pulse energy fluctuations on a shot-to-shot basis. The pyroelectric detector uses an identical transimpedance amplifier to the one used for the nanoantenna read-out to ensure comparable statistics of the individual signals. Details on the acquisition and digitization of the signal are given in Sec. 6.5.3.2. In this experiment each dataset consists of the measured charge from the nannoantenna array and the corresponding pulse energy, recorded for around 50 000 shots (1 s). In each dataset, the CEP of the laser is linearly ramped for 600 ms with a speed of $2\pi\cdot 10$ Hz, starting at ∼120 ms. For different datasets the pulse energy was systematically varied by more than a factor of ten.

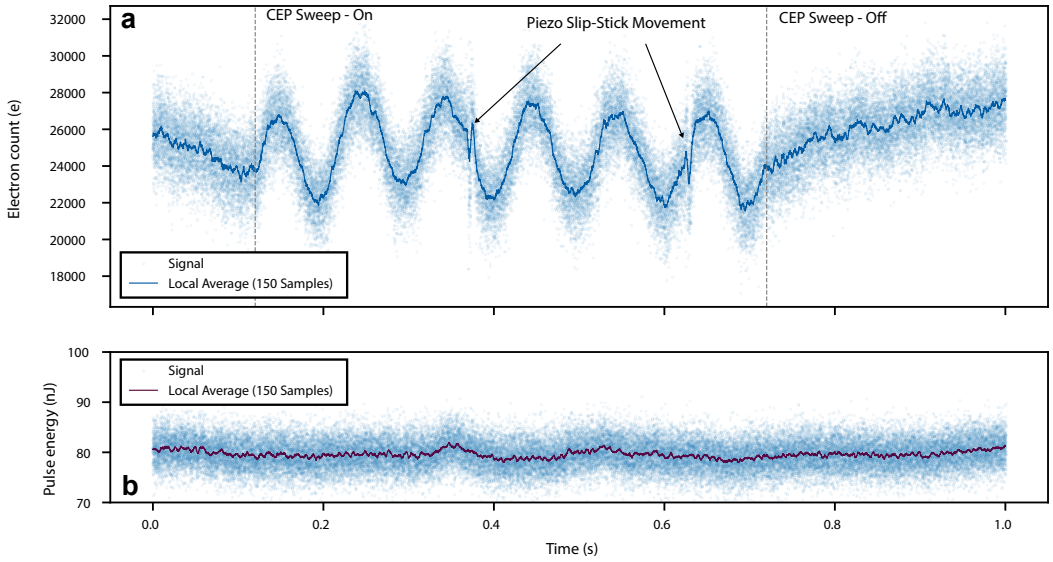

Figure 6.3: **Single-shot charge readout:** A single dataset recording of 50 000 laser shots for the charge yield of the nanoantenna detector (upper panel) and the laser energy recorded by the pyroelectric detector (bottom panel). The peak field of the incident laser pulse on the array is 1.6 V nm. From 120 ms to 720 ms the CEP is linearly ramped over 6 cycles.

A single dataset is presented in Fig. 6.3, including both the single-shot data and the moving average calculated over 150 shots (dark line). The upper panel shows the recorded charge produced by the nanoantenna array, with an average yield of 25 000 e$^-$ per shot. From 120 ms to 720 ms the CEP is linearly ramped over a 12π range. The data points show a clear sinusoidal

CEP dependence with an amplitude of 2370 e^-, while the pulse energy shows no modulation. When considering the number of illuminated antennas, the individual CEP-sensitive yield per antenna and shot is 3.3 e^-, indicating a peak current through the nanoantenna gap of up to a 100 e^-/fs, corresponding to 10 mA. Given the small cross-section of the nanoantenna tips, that is around 10 nm by 30 nm, the current density reaches a remarkable 5 GA cm^{-2}. At t =370 ms and 620 ms, sharp changes are observed in the charge yield of the detector element. These features, that are 250 ms apart, are caused by the specific movement pattern of the closed-loop slip-stick piezo stage (Smaract GmbH, SLC-2430) used to control the CEP, that recenters the piezo position every 1.3 µm.

To isolate the CEP-dependent signal from readout noise and pulse energy fluctuations, we Fourier transformed the dataset between t =120 ms and t =620 ms and compared it to the frequency spectrum obtained without any optical input; see Fig. 6.4. The spectrum of the antenna

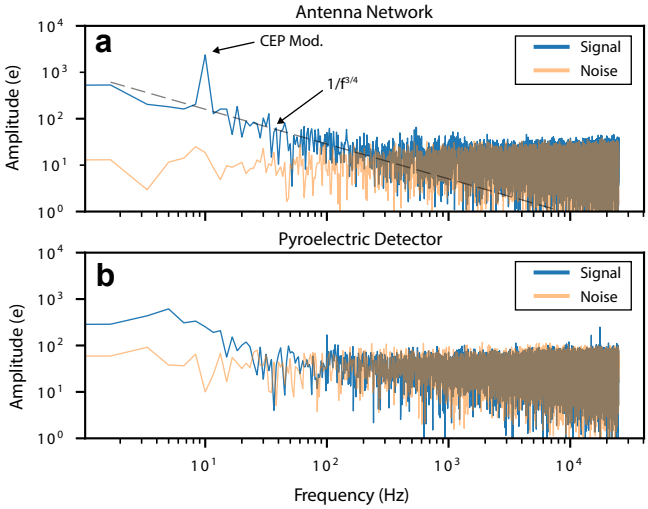

Figure 6.4: **Frequency Domain of the single-shot data:** The respective data from Fig. 6.3 t = 370 ms to t = 620 ms is Fourier transformed and shown in charge amplitude as a function of frequency. For comparison, the electronic noise floor is shown in orange for both spectra. **a**) the frequency-resolved signal of the nanoantenna network. **b**) the frequency-resolved pulse energy fluctuation, detected with the pyro-electric detector.

array shows a clear peak at 10 Hz corresponding to the $2\pi\cdot$10 Hz modulation of the CEP. This signal is around two orders of magnitude higher than the readout noise floor. The noise in the measured spectrum is dominated from DC to ~250 Hz by $1/f^{3/4}$ scaling, which is typical for field emission devices and is attributed to Brownian noise of the work function due to dynamical changes of adsorbates on the surface [23, 133]. At frequencies higher than 250 Hz the spectrum is limited by shot noise, with a substantial component originating from the detection noise of the transimpedance amplifier itself. The calculated shot noise of the signal is ~ 160 e rms. When evaluating the recorded pulse energy fluctations at the photodetector, no 10 Hz modulation is distinguishable from the background (see Fig. 6.4 b). Above 100 Hz the pulse energy spectrum

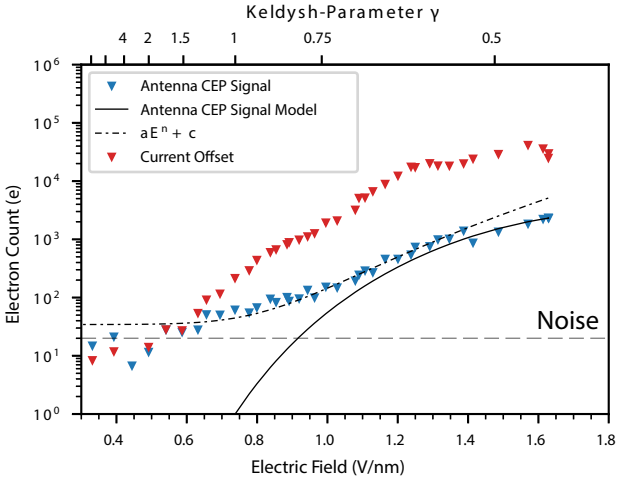

Figure 6.5: **Charge yield scaling:** The CEP modulation amplitude and the magnitude of the average charge yield are plotted as a function of the average peak field, estimated for CEP= 0, for the respective dataset. The CEP signal is taken from the amplitude of the 10 Hz frequency component of the measurement data. The antenna CEP signal model uses the model described by Eq. 6.3. Furthermore, a power law fit, $aE^n + c$ to the first 30 values is shown.

is dominated by detector noise. To elucidate the mechanism underlying the CEP-dependent electron emission, the amplitude of the CEP modulation is shown in Fig. 6.5 (blue triangles) as a function of the incident peak field of the laser pulse. In order to estimate the CEP dependent emission, we use the electric field as retrieved by the pulse characterization convoluted with the impulse response function of the nanoantenna. For peak fields larger than $1.2\,\mathrm{V\,nm^{-1}}$(estimated for CEP= 0), corresponding to a Keldysh parameter $\gamma \sim 0.6$, the CEP-dependent charge yield scales according to the quasi-static tunneling approximation shown in Eq. 6.3. For values below $1.2\,\mathrm{V\,nm^{-1}}$, the data follows a power law model $aE^n + c$, with $n = 7.85$, $a = 110$ and $c = 35$. This scaling behavior suggests a transition from nonadabatic tunneling emission to the quasi-static tunneling regime [69, 134]. This scaling behavior was verified by repeating the experiment with a different nanoantenna array. The results of this second device are presented in Supplementary S1. The interaction of the optical pulse with our nanoanntenna arrays generates not only CEP-dependent charges but also a pulse energy-dependent charge offset. The magnitude of the average charge yield of each trace (red triangles) is around one order of magnitude larger than the CEP-dependent yield and scales nonlinearly with the pulse energy. It should be noted that this current does not increase monotonically, but goes through a local minimum in the field range from $1.25\,\mathrm{V\,nm^{-1}}$ to $1.6\,\mathrm{V\,nm^{-1}}$. This current scales differently to the CEP-dependent current, implying a different origin than the nanoantenna array. Additional investigation is required as we suspect parasitic field emission from the electrodes close to the nanoantenna array or thermal emission processes that play a role. We believe that an improved electrode design would greatly suppress the charge offset. A similar behavior of the charge offset has been observed in a different size antenna network (see Chap. 6.5.4.2).

6.3 Conclusion

We have demonstrated single-shot readout of CEP-dependent charge signals at 50 kHz repetition rate, underlying sub-cycle current generation across a macroscopic device area of 225 μm^2 integrating more than 700 individual antenna pairs. This was possible by improving the average CEP-dependent charge yield per single antenna by a factor of $\sim$30 [10, 23], now reaching 3.3 e^- per shot, and by illuminating hundreds of antennas simultaneously. The enhanced antenna yield implies a remarkable peak current density of up to 5 GA cm^{-2} [8, 10, 23]. With this result, we show that metallic nanoantenna networks, fabricated via state-of-the-art lithographic methods, are a flexible and scalable approach to optical frequency electronics that allows to design individual circuit elements, similarly to conventional microelectronics. Thanks to this advance, we demonstrated off-resonant antennas that are sensitive to pulse energies two orders of magnitude lower than any other comparable single-shot absolute CEP detection technique [18, 51, 135], enabling CEP detection of optical pulses with only tens of nanojoules of energy. Further optimization of the network density (see Sec. 6.5.2) combined with a reduced number of optical cycles in the pulse would potentially increase the total yield by an additional two orders of magnitude [23].

Given the exceptional current densities generated in these nanometer sized devices, further studies will be necessary to elucidate the role of electron-electron during the sub-cycle emission process [136]. Based on this platform, many different experiments and applications can be developed, such as the investigation of petahertz bandwidth logic gates and memory cells[24, 25]. The extremely small device size, comparable to the pixel size in modern Si-based CMOS detectors, combined with the reduced pulse energy requirements, enables the integration of multiple nanoantenna arrays in a larger pixel matrix. This will allow for a CEP sensitive camera. Absolute single-shot CEP tagging can also be implemented by adapting I/Q demodulation with two separate networks recording $\pi/2$ phase-shifted currents. The previously demonstrated techniques of attosecond-resolved field sampling can be extended to single-shot readout, by making large line arrays of individual networks [20, 137]. Another area of progress will be the adaptation of the fabrication process to become fully CMOS-compatible by replacing gold with aluminum or copper. With our results and natural avenues of progress, we believe that our platform will play a major role in future ultra-high-frequency light-driven electronics.

6.4 Methods

Nanofabrication

[2] A fused silica wafer was purchased from MTI Corporation and cut with a die saw. The substrates were cleaned by sonicating in acetone and isopropyl alcohol for 5 minutes each. Subsequently, the pieces were cleaned using an oxygen plasma. Poly(methyl methacrylate) A2 was spun at 2,500 revolutions per minute and baked at 180 °C, then DisCharge H2O was spun at 1,000 revolutions per minute so that charging did not occur during the electron beam lithography write.

Electron beam lithography was performed using an electron beam energy of 125 keV with doses varied from 4000-6000 μC cm2 with a proximity effect correction. After exposure, the resist was developed in a 3:1 isopropyl alcohol/methyl isobutyl ketone solution for 50 seconds at 0 °C. Subsequently, the antenna deposition was performed using an electron beam evaporator operating below 9e-7 Torr. First, a 2 nm adhesion layer was deposited, then 20 nm of gold. Lift-off was performed in a 65 °C-70 °C bath of N-methylpyrrolidone.

After antenna fabrication, contacts were patterned by photolithography using a bilayer of PMGI and S1838 both spun at 4,500 revolutions per minute. The deposition was performed by electron beam evaporation with a 40 nm adhesion layer and 160 nm of gold so that they could be wire-bonded to a printed circuit board.

6.4.1 Extended Data Figures

[2] The devices were fabricated by Matthew Yeung at the MIT cleanroom facilities.

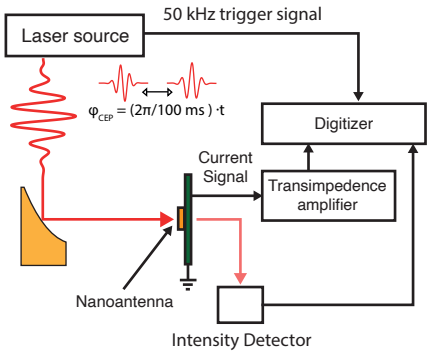

Figure 6.6: **Experimental setup:** The experimental setup consists out of a home-built laser source, delivering 18 fs at a center wavelength of 2.7 µm with up to 84 nJ of energy at a repetition-rate of 50 kHz, a 25.4 mm focal length off-axis parabola and the nanoantenna detector element at the focal spot. For detection of the charge signal, we use a custom transimpedance amplifier with a gain of $1\,\mathrm{GV\,A^{-1}}$ and a -3 dB bandwidth of 50 kHz. For detection of the single shot intensity signal of the laser pulse, we use a 50 kHz bandwidth pyro-electric detector in transmission after the detector. The charge and the intensity signals are digitized with an 8-Bit oscilloscope at a sampling rate of 20 MSa/s. To retrieve the individual single-shot events, the digitized pulses are integrated and sorted based on the timing signal of the 50 kHz trigger signal provided by the laser source. To produce a CEP-dependent signal, the CEP of the laser source is linearly swept at a rate of $2\pi/100$ms for 600 ms.

6.5 Supplementary Information

6.5.1 Description of the Sub-Cycle Field Emission Current

To gain in qualitative understanding in the sub-cycle dynamics of the field emission process, it is useful to simulate the probability of measuring an electron at a given point in time and space outside the metal in a vacuum state. To that end, Yalunin et al. showed that the numerical integration of the time-dependent Schrödinger equation [65],

$$i\frac{\partial\Psi}{\partial t} = \left(-\frac{1}{2}\frac{\partial^2}{\partial x^2} + V\right)\Psi, \tag{6.4}$$

describing the interaction of a bound electron in a metal with a time-periodic field $F(t)$ is a valid approach. The potential V used is of the form,

$$V = -\begin{cases} xeF(t), & x \geq 0 \\ E_F + W, & x < 0, \end{cases} \tag{6.5}$$

were E_F is the Fermi energy and W the workfunction. By using the modified Crank-Nicolson scheme as described in [65], we calculate the probability $|\Psi(x,t)|^2$ for a gold workfunction of

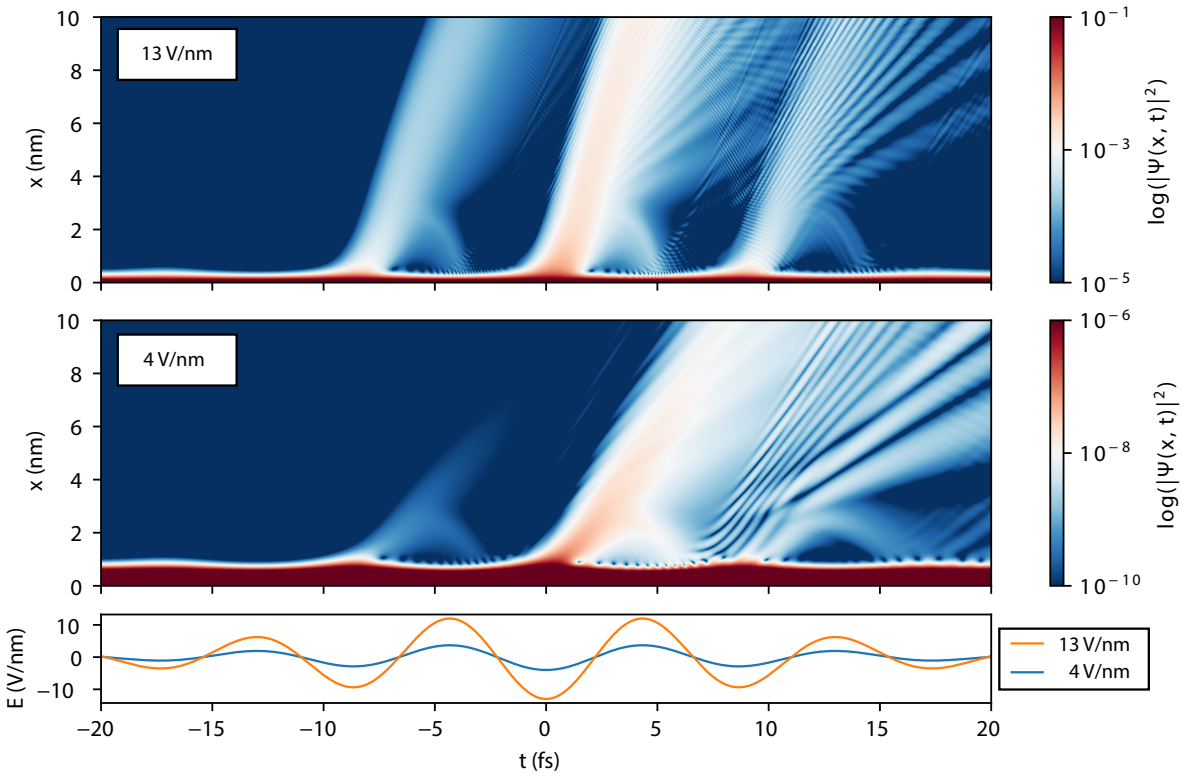

Figure 6.7: **Numerical Solution to the Time-Dependent Schrödinger Equation:** Integration of the time-dependent Schrödinger equation, by using the modified Crank-Nicolson scheme as described by [65]. The top two panels show the probability amplitudes for two cases assuming an 18 fs duration MIR pulse at a center wavelength of 2.7 µm with 4 V nm^{-1} and 13 V nm^{-1} field strength. The bottom panel is showing the used electric field as a function of time.

$W = 5.1$ eV and an 18 fs duration MIR pulse at a center wavelength of 2.7 µm. The used field strength are 4 V nm^{-1} and 13 V nm^{-1} to reflect the local fields strength measured in Fig. 5 in the main text.

The results of the integration, presented in Fig. 6.7, show the probability $|\Psi(x,t)|^2$ of measuring an electron at a given coordinate (x,t). As one can see, at the low field strength of 4 V nm^{-1} the emission process is already highly sub-cycle. Driven by the peak of the electric field the electrons are ejected from the surface within a half-cycle. Strong scattering of electrons re-accelerated to the potential barrier occurs between 5 fs and 10 fs. For the case of 13 V nm^{-1} we can see stronger emission probabilities with suppressed quiver motion and rescattering at the surface. Both cases show that for the full field strength range explored in the main text in Fig. 5, the emission mechanism is still sub-cycle field-emission.

Despite the well described qualitative and also quantitative scaling laws of electron emission using numerical integration [65], we found difficulties adapting this scheme when accounting for a system that consists of two individual emitters, driven with a π phase-shifted pulse and subtracted as described in Eq. 3. As the CEP dependent charge is on the order of 0.1 or

less of the total emitted charge, errors in the charge calculation are enlarged for the difference measurement. Therefore, we use for the CEP dependent charge yield model the quasi-static Fowler-Nordheim approximation [63].

6.5.2 Electromagnetic Simulation of the Nanoantenna

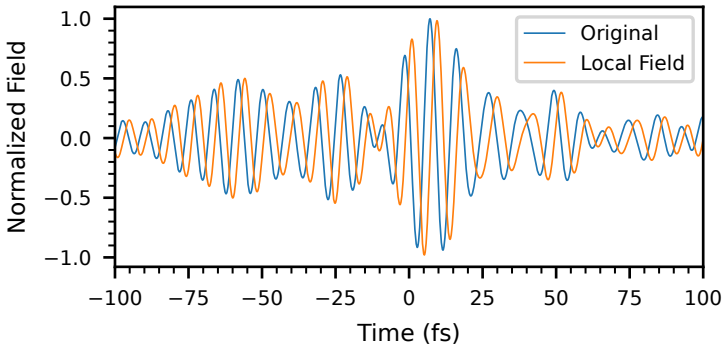

Figure 6.8: **Comparison of the Original Electric Field vs. the Local Field:** The original incident electric field and the calculated local field at the tip of the nanoantenna as a function of time.

[3] Electromagnetic simulation was performed to estimate the local field at the apex of the nanoatenna. A simulation procedure similar to the one described in [23] was used. A fully linear response of the device is assumed, which allows for calculation of the response function in the frequency domain. A numerical solution of the Maxwell equations is obtained using the finite element method electromagnetic waves, frequency domain solver from the wave optics module of COMSOL Multiphysics. The system was modeled by a connected antenna bow-tie consisting of gold placed on a glass substrate. The dimensions of the antenna geometry were chosen to fit the fabrication design parameters. The n and k values of gold were taken from [138] and a constant refractive index of 1.46 was assumed for the glass substrate. An incident plane wave with a propagation direction perpendicular to the antenna-substrate interface was added on top of the geometry. The incident light is linearly polarized with the electric field being orthogonal to the connecting wires. Periodic boundary conditions were added around the antenna boundary to model the array. The semi-infinite vacuum and substrate were modeled using perfectly matched layers on top and bottom of the simulation domain. The linear response function was evaluated by comparing the results obtained with the results of an empty simulation domain with the same simulation settings.

With the simulated complex frequency response $\tilde{H}(\omega)$, see Fig. 2, and the incident field $E(t)$

[3]The simulation of the electromagnetic antenna response was performed by Engjell Bebeti within the scope of his masters thesis and was supervised by the author.

the local field $E_L(t)$ averaged over the surface of the nanoantenna tip can be calculated,

$$\tilde{E}_L(t) = \mathscr{F}^{-1}\{\tilde{E}(\omega)\cdot\tilde{H}(\omega)\}. \tag{6.6}$$

The resulting normalized local field is shown in Fig. 6.8. The local field is only marginally different from the incident electric field. However, the effective field-enhancement is 8.2, making the local field substantially stronger than the incident one. Compared to the field enhancements of around 20 in references [8–10, 20, 23], the antenna was designed to be off-resonant to preserve the incident electric field shape, while still having a sufficiently large field enhancement. Furthermore, the antenna design allows for a high antenna density of $\sim 3\,\mu m^{-2}$, compared to an antenna design that is resonant with the MIR field, since these would require roughly double the antenna size.

Further investigation of the design showed that the maximum value of the CEP dependent current is further improved by a factor of two by increasing the antenna density. The increased density damps the resonant part of the response function, but maintains a broadband off-resonant field enhancement with a factor of $\sim 6-7$. The gradual change of antenna density is shown in Fig. 6.9. Using the formulas of the quasi static model, the increase in CEP dependent current per unit area is estimated and corresponds to a factor of two improvement from the device presented in the main text.

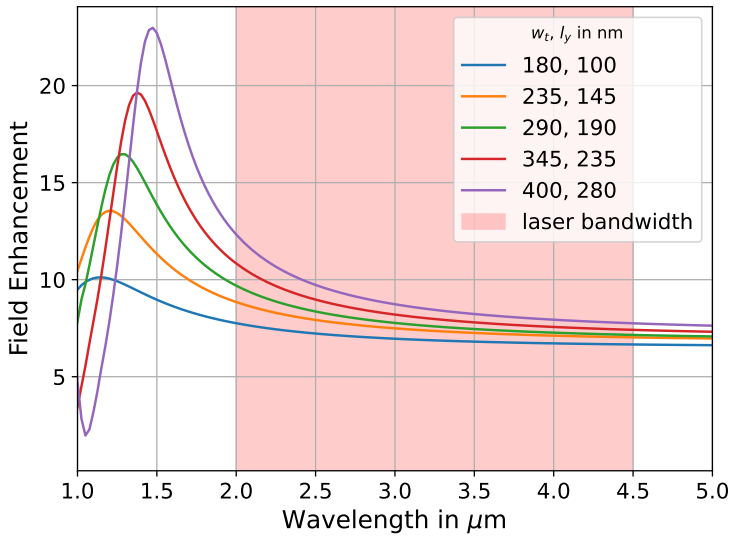

Figure 6.9: **Simulated Field Enhancement for Different Antenna Densities:** The average field enhancement at the nanoantenna apex as a function of wavelength for different antenna densities. w_t denotes the distance between neighboring antennas and l_y the closest distance between two arrays. The values $w_t = 400\,nm$ and $l_y = 280\,nm$ correspond to the fabricated device presented in the main text. The most dense case with $w_t = 180\,nm$ and $l_y = 100\,nm$ has an approximately 2.9 times higher antenna density, while maintaining a similar off-resonant field enhancement.

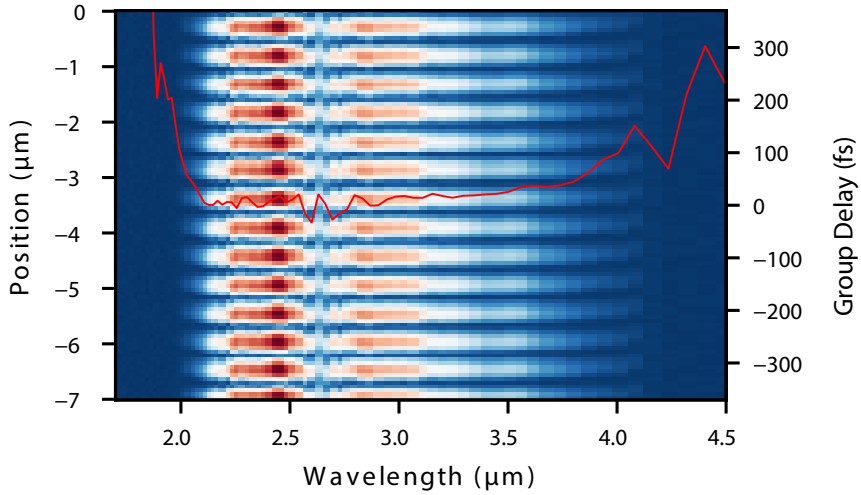

Figure 6.10: **Two-Dimensional Spectral Shearing Interferometry:** Measured 2DSI trace shown in logarithmic color coding. On the right hand axis in red is as an overlay the retrieved group delay.

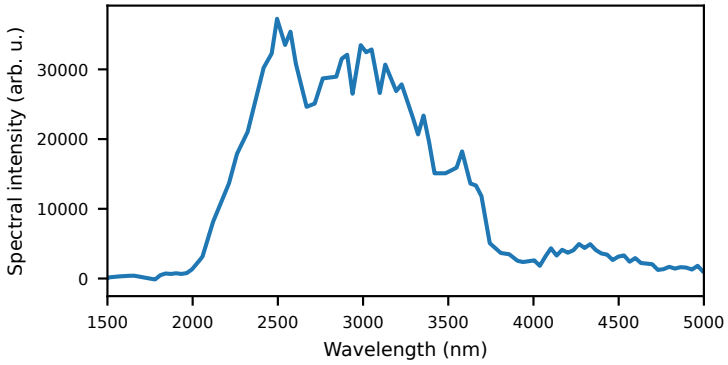

Figure 6.11: **Measured Mid-Infrared Spectrum:** Raw mid-infrared spectrum measured on a PbSe-CCD spectrometer.

6.5.3 Experimental Setup

6.5.3.1 Laser Source Characterization

To reflect the state of the laser source used for the described experiment, we show here the characterization of the pulse duration within a 24 h time window to the experiment. The pulse duration is measured by an adapted version of two-dimensional spectral shearing interferometry (2DSI) [91, 110], as presented in Chap. 5.3.2.

In Fig. 6.11 the raw mid-infrared spectrum is shown. The spectrum was measured on a PbSe-CCD spectrometer.

Using the measured mid-infrared spectrum and the retrieved group delay, the time domain of the pulse can be calculated up to an arbitrary CEP. The calculated time domain in intensity and

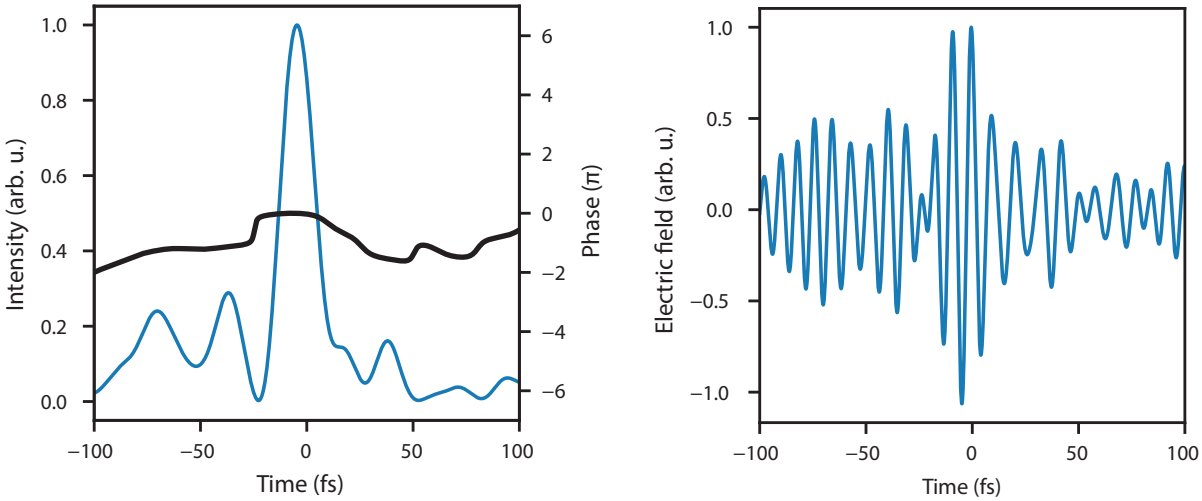

Figure 6.12: **Reconstructed Time Domain:** (Left) Reconstructed intensity distribution of the mid-infrared pulse (blue) and the retrieved phase (black). (Right) Electric field profile of the retrieved mid-infrared pulse set at an arbitrary CEP.)

electric field are shown in Fig. 6.12. The retrieved pulse FWHM duration is 18 fs at a center wavelength of 2.69 µm. This corresponds to two cycles of the carrier wave within the FWHM duration.

6.5.3.2 Charge Generation and Readout

For the readout of the charge in the nanoantenna network we used a custom transimpedance amplifier (TIA) provided by WiredSense GmbH. The amplifier has a total gain of 1 GV A^{-1} at a -3-dB bandwidth of 50 kHz. The input and the output of the TIA are AC coupled. The full response function, the output voltage noise and the equivalent input noise of the TIA are shown in Fig. 6.13. The pyro-electric detector used to detect the shot-to-shot intensity changes was also provided by WiredSense GmbH and has an identical -3 dB bandwidth 50 kHz.

To digitize both signal channels and retrieve the individual charge yields, we used an 8-Bit oscilloscope recording the TIA, the pyro-electric detector and a trigger signal provided by the laser source at a sampling rate of 10 MSa/s. For the 50 kHz repetition rate signal, the sampling rate was chosen to provide sufficient oversampling to alleviate digitization problems of the low bit-rate oscilloscope. Oversampling by a factor of x and integration of a digital signal increases the effective bit-range n by $n = \ln(x)/(2\ln(2))$, if the lowest bit is submitted to sufficient Gaussian noise. An example of recorded oscilloscope trace is shown in Fig. 6.14

The trigger signal falling slope was used as a reference to sort the individual shots with their respective time stamp. Before integrating over the AC coupled current signals, a baseline was introduced by averaging over the signal for 3 µs before every trigger and subtracting it locally for the respective time windows. The result of that subtraction is shown in Fig. 6.15. To retrieve the charge contained within each current pulse, the current pulse was integrated over and

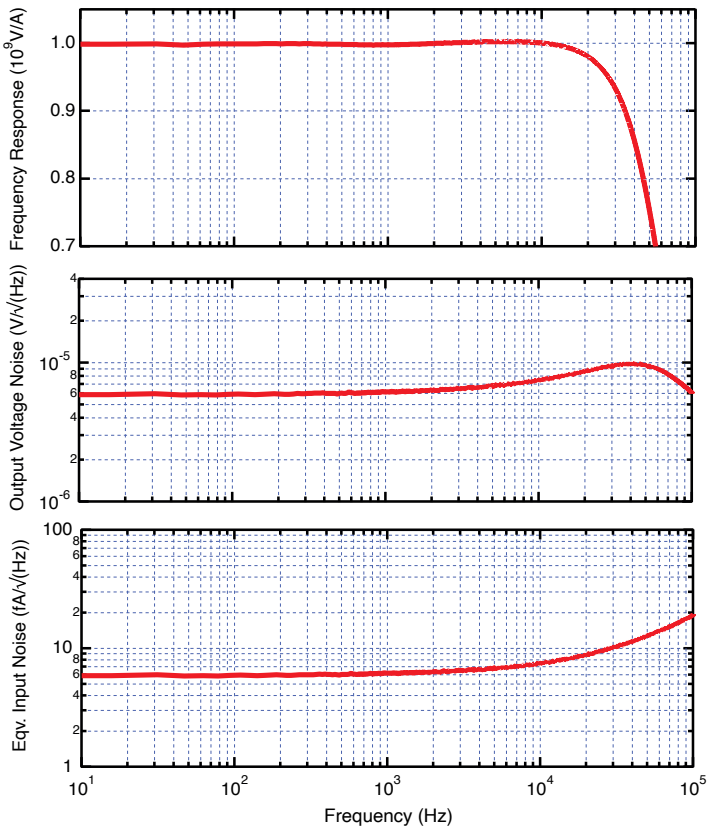

Figure 6.13: **Characterization of the Transimpedance Amplifier:**The TIA is characterized by measurements with an FFT analyser. (Top panel) The frequency response curve of the TIA. (Middle panel) Measured output voltage noise. (Bottom panel) Equivalent input current noise, this is calculated by dividing the output voltage noise with the frequency response of the TIA.

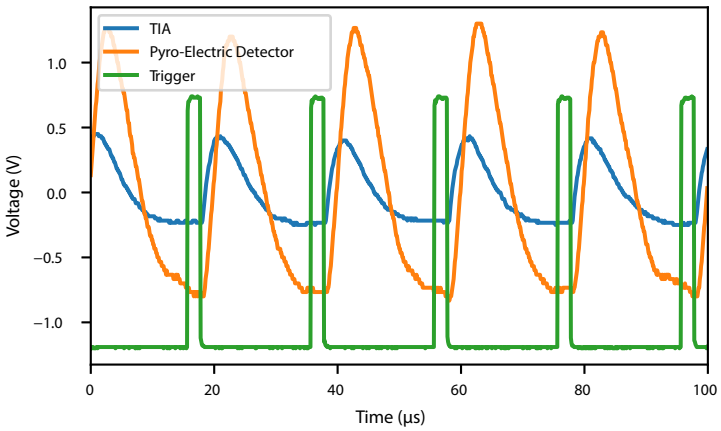

Figure 6.14: **Recorded Oscilloscope Trace:** Exemplary recorded 100 µs voltage time trace showing the trigger signal (green), the TIA output (blue) and the pyroelectric detector output (orange).

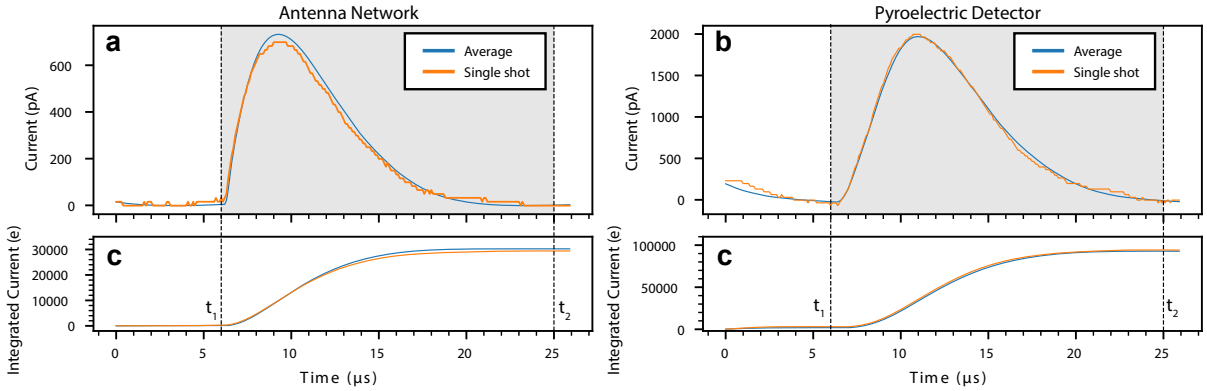

Figure 6.15: **Charge Integration Scheme:** (**a**) Antenna network current pulse, shown for a single pulse and averaged over many pulses to reduce noise and digitization. (**b**) Pyro-electric detector current pulse, showing a single pulse and the averaged pulse form. (**c**) Integrated current of the antenna network as a function of time showing a single shot and for an averaged pulse form. t_1, t_2 denote the sampling points used for the charge calculation. (**d**) Integrated current of the pyroelectric detector pulse, showing a single shot and for the averaged pulse form. t_1, t_2 denote the sampling points used for the charge calculation.

the integrated signal is sampled at points t_1, t_2. The integrated charge is simply the difference of charges measured at the sampling points, $Q_{Shot} = Q(t_2) - Q(t_1)$. This technique is called correlated double sampling (CDS) and is commonly used in charged-coupled device readout circuitry[139]. The time correlated differentiation significantly reduces uncorrelated low frequency noise[140].

6.5.3.3 Device Layout

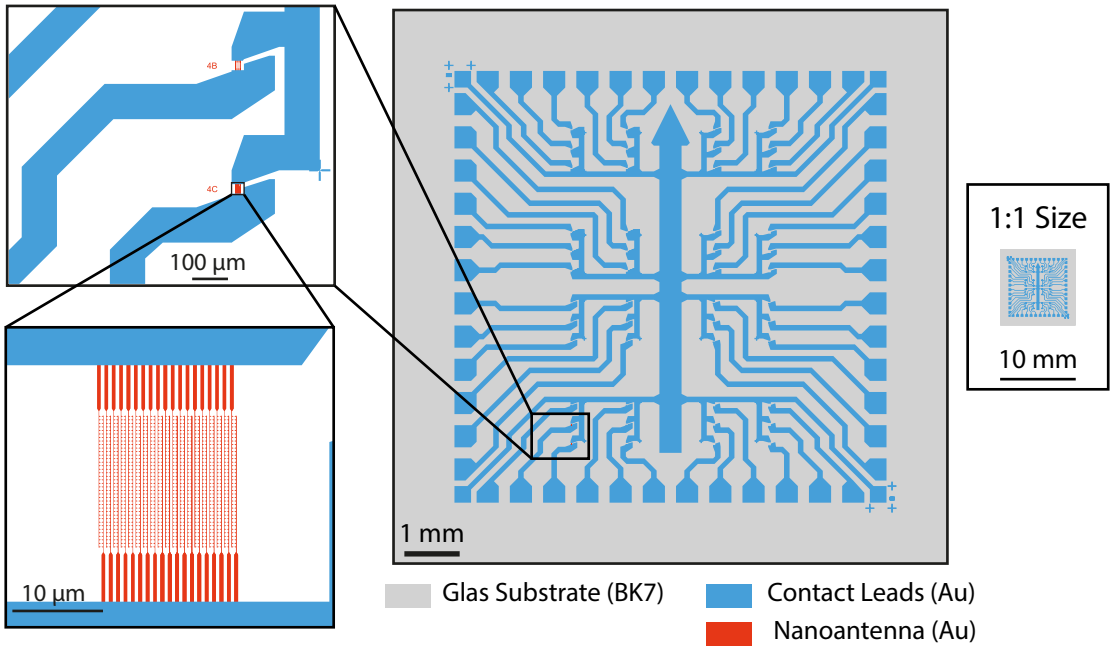

Figure 6.16: **Circuit Layout:** Layout of the microchip carrying the nanoantenna arrays. Progression of sizes from a 1:1 scale down to 1:1000 (Assuming Din-A4 printout of this page). Blue areas mark the contact leads fabricated through photolithography in gold (Au). Red areas mark the nanoantenna arrays fabricated through electron-beam lithography in gold (Au). Grey arrea marks the glas (BK7) substrate.

Fig. 6.16 shows the complete layout of the tested chip that contains the nanoantenna arrays. The chip layout is shown on a 1:1 scale with zoom-in on the relevant array tested in the main text. The device, as stated in the Chap. 6.4, is fabricated through a two-step process. The small-scale nanoantenna arrays are fabricated on a BK7 substrate through electron-beam lithography in gold (Au). The second step is the fabrication of larger-scale contact leads through photolithography in gold (Au). The role of the contact leads is to make robust electrical contact with the nanoantenna arrays and to provide large pads at the outer edge of the chip for wire bonding. By visual analysis in a scanning electron microscope, the best 24 arrays of 48 are selected for wire bonding to a printed circuit board.

The layout of the device presented in the main text is shown in Fig. 6.17 a. The nanoantenna array itself is shown by the red shaded structure and is produced through electron-beam lithography. The pink area is showing contact leads that connects the nanoscale devices with the large wire bond pads at the edges of the chip. The device measures 15 µm by 15 µm for the nanoantenna array. For comparison the spatial dimension of the optical focus (FWHM and $1/e^2$) is shown as dashed circles. An additional device with an area of 30 µm by 30 µm is shown in Fig. 6.17 b. The two devices show the case of an array smaller than the laser focus and larger than the laser focus.

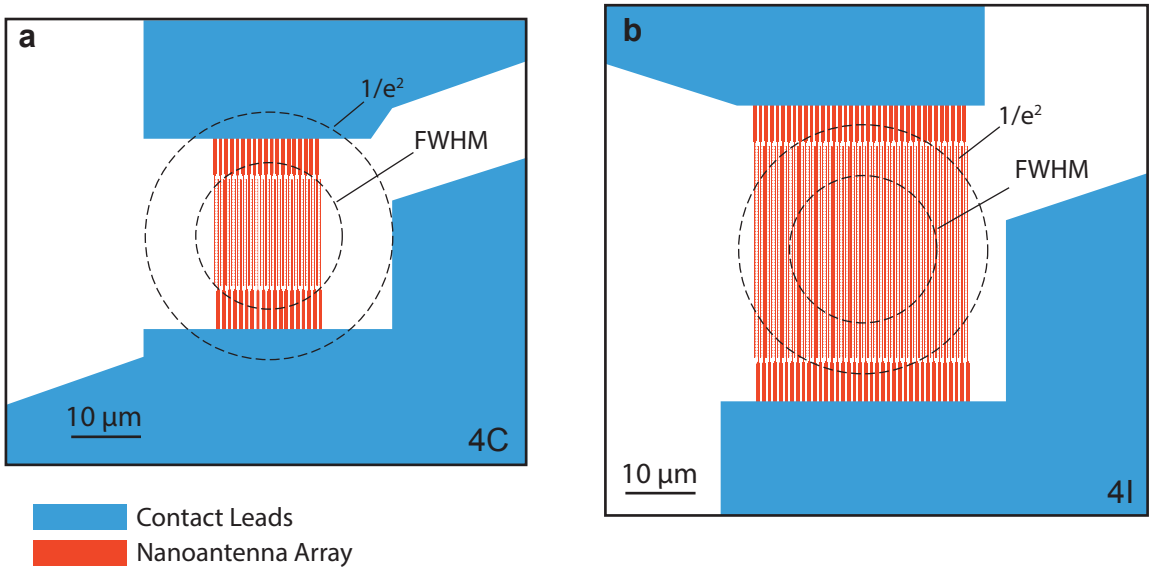

Figure 6.17: **Device Layout:** Layout of the devices used in this work. The blue area shows the contact leads fabricated by photolithography. The read areas show the nanoantennas made by electron-beam lithography. The dashed circles mark the approximate spatial distribution of the laser focus (FWHM: 21 µm, $1/e^2$: 35.5 µm). (**a**) Layout of the device shown in the main text. The nanoantenna array area of the device measures 15 µm by 15 µm. (**b**) Layout of the device shown in the supplementary. The nanoantenna array area of the device measures 30 µm by 30 µm.

6.5.4 Complimentary Measurements

6.5.4.1 Background Charge Signal

During the measurements across all tested devices, we observed an intensity-dependent charge background. To investigate the possible origin of this contribution, we tested two different hypotheses. First, that the charge signal generated by a multiphoton emission process, and second that it is generated by a field emission process based on Fowler-Nordheim tunneling. The results are shown in Fig. 6.18. The multiphoton fit is defined as,

$$Q(E,n,\alpha) = \alpha \cdot (E)^n + c, \tag{6.7}$$

with the polynomial order n and a scaling prefactor α. $n = 7.4$, $\alpha = 1.9 \cdot 10^3$ and the offset $c = 3.9$. This hypothesis implies that a 3-4 photon process is causing electron emission, which is incompatible with the photon energy of the optical pulse spanning 0.3 eV to 0.6 eV and the workfunction of gold with 5.1 eV. This means that either another process is inducing a current other than electron emission from gold or that multiphoton is not the right explanation. The second tested hypothesis is that of a field emitter other than the nanoantenna array. To test this

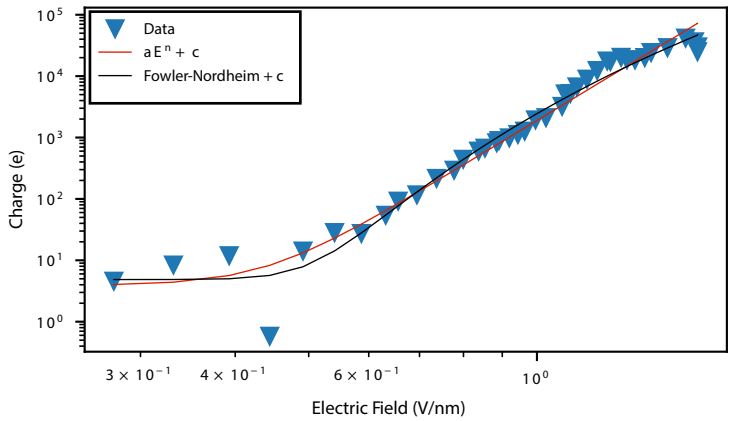

Figure 6.18: **Background Charge Yield:** The average charge yield as a function of peak electric field. A multi-photon absorption and Fowler-Nordheim based model are fitted to the data. For the multi-photon the function $Q(E,n,\alpha) = \alpha \cdot E^n + c$ is used, with fit results $\alpha = 1.9 \cdot 10^3$, $n = 7.4$ and $c = 3.9$. For the Fowler-Nordheim fit the function $\Gamma(E,g,\alpha) = \alpha(gE)^2 \exp\left\{\left(-\frac{78.7}{|gE|}\right)\right\} + c$, with the results $\alpha = 1705$, $g = 15.4$ and $c = 4.9$.

we used the Fowler-Nordheim fit function $\Gamma(E)$,

$$\Gamma(E,g,\alpha) = \alpha(gE)^2 \exp\left\{\left(-\frac{78.7}{|gE|}\right)\right\}, \tag{6.8}$$

with the prefactor α, the field enhancement g and critical field strength of $78.7\,\mathrm{V\,nm^{-1}}$. The Fit results show a prefactor of $\alpha = 1705$, a field enhancement of 15.4 and the offset $c = 4.9$. This result implies that there is different field emitter causing this charge yield, as the designed field enhancement of the nanoantenna is on the order of ~ 8. However, as this is merely a quantitative speculation, further research is warranted to uncover the cause of this charge contribution. One test experiment could be to use an identical device but excluding the nanoantenna arrays. With that, all contributions from the large gold leads, if also contributing, can be measured independently. Second the change of polarization could be tested, as these nanoantennas are highly polarization sensitive [9]. However, continuous changing of polarization in the MIR is difficult due to a lack of suitable achromatic waveplates and cannot easily be implemented.

6.5.4.2 Larger Area Network

To verify the results measured in the main text we repeated the same measurements with an antenna network that measures 30 µm by 30 µm, which is substantially larger than the FWHM beam width of $\sim$ 21 µm. The other difference between these measurements is the use of a different detector for the single-shot pulse energy, which is, in this case, a commercial mercury cadmium telluride detector. This amounts to roughly 1000 antennas within the spatial FWHM contributing to the measured charge yield. A single-shot measurement is shown in Fig. 6.19.

Identical to the main text, a clear CEP modulation is present in the measured data. Furthermore, also the same signatures of the piezo slip-stick motion are present in the data. In addition, we see a 3x larger background charge signal compared to the other measurement.

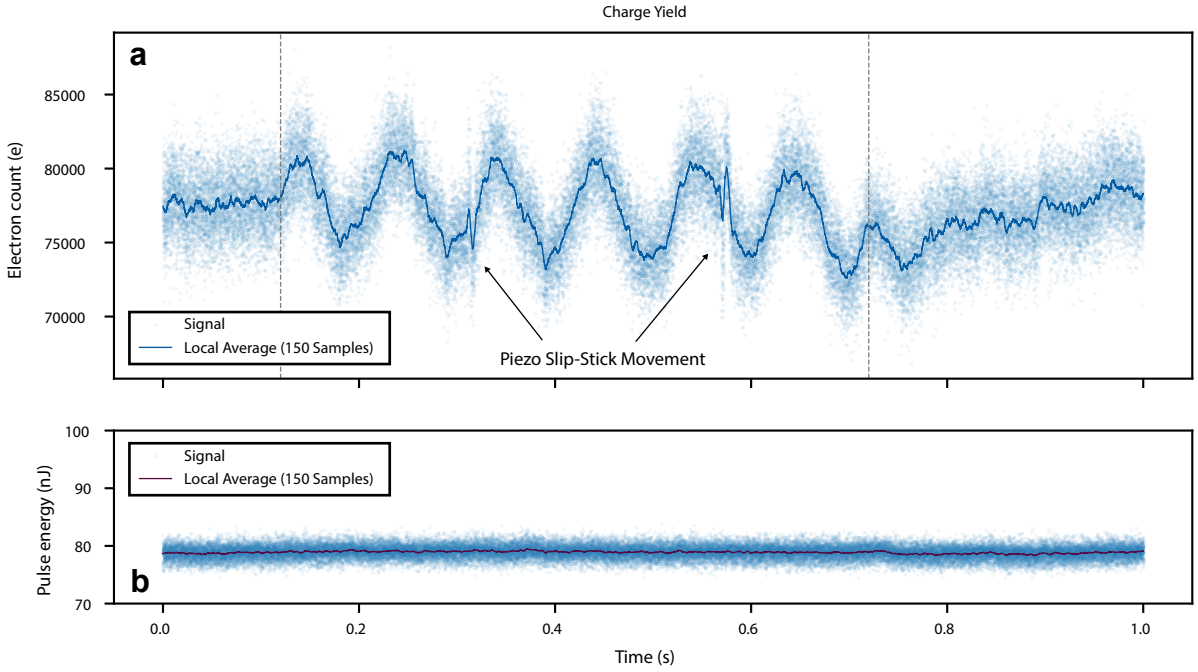

Figure 6.19: **Single-shot charge readout:** A single dataset recording of 50 000 laser shots for the charge yield of the nanoantenna detector (**a**) and the laser energy recorded by the pyroelectric detector (**b**). The peak field of the incident laser pulse on the array is 1.6 V nm. From 120 ms to 720 ms the CE phase is linearly ramped over 6 cycles.

As in the main text, the same frequency analysis of the single-shot measurement is shown, which presents reproducible behavior. Aside from the clear CEP peak, we see in addition the same $1/f^{3/4}$ noise characteristic is present in the data. The narrow band noise peaks at ~ 17 kHz in the electron amplitude are clearly discernible from noise. In conjunction with the higher background charge signal, we can strengthen the argument that the noise peaks are driven by high frequency laser intensity changes predominantly modulating the background charge signal.

Analysing the scaling of the CEP peak as a function of incident peak field, we find in general similar behavior in Fig. 6.21. The Fowler-Nordheim fit results in a field-enhancement $g = 8$, very close to the simulated field-enhancement of 8.2. Furthermore the prefactor $a = 1647$ is almost identical to the one in the main text with $a' = 1517$, indicating that this array, despite the larger size, has a comparable amount of antennas contributing to the charge signal, as a is proportional to the amount of antennas. Further measurements with different array sizes could map more precisely on how many antennas are involved in the charge signal. The heuristic power law fit, $Q(E) = aE^n + c$, shows as well comparable behavior to the array discussed in

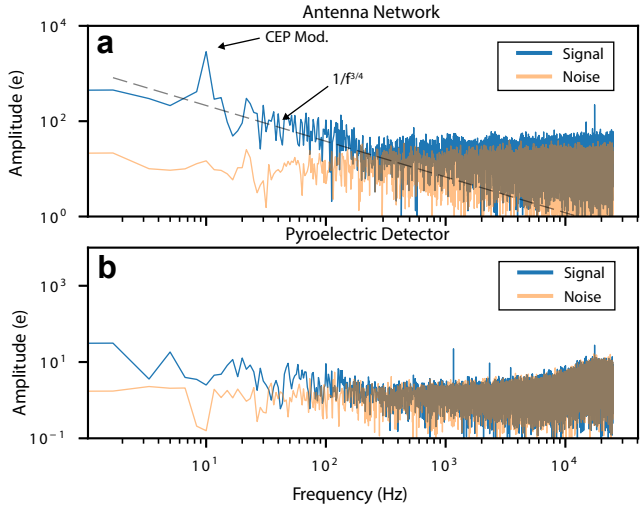

Figure 6.20: **Frequency Domain of the single-shot data:** The respective data from Fig. 6.19 $t = 370\,\text{ms}$ to $t = 620\,\text{ms}$ is Fourier transformed and shown in charge amplitude as a function of frequency. For comparison, the electronic noise floor is shown in orange for both spectra. (**a**) the frequency-resolved signal of the nanoantenna network. (**b**) the frequency-resolved energy signal, as a function of pyroelectric charge yield.

the main text. The fit results are $a = 147$, $n = 7.65$ and $c = 13$, which in particular with the power law order n agrees very well with the main text where $n' = 7.85$ is measured. This shows that the measurements are in general of predictable behavior. Although the scaling law for low field-strengths is not fully understood in this context, models like the Yudin-Ivanov [69], could help to illucidate these scaling behaviors.

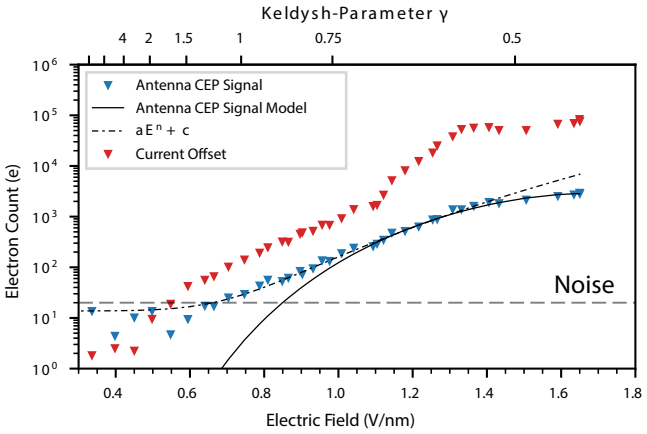

Figure 6.21: **Charge yield scaling:** The CE phase modulation amplitude and the average charge yield are plotted as a function of the average peak field for the respective dataset. The CE phase signal is taken from the amplitude of the 10 Hz frequency component of the measurement data. The antenna CE phase signal model uses the model described by Eq. 3. Furthermore, a power law fit, $aE^n + c$ to the first 30 values is shown.

7 Conclusion and Outlook

This thesis presents key results in the emerging field of optical frequency electronics. In Chapter 3, a technique for on-chip measurements of optical fields with attosecond resolution in the time domain is presented. This allows for the measurement of optical waveforms with an unprecedented sensitivity down to femtojoules of energy, exceeding the energy sensitivity of comparable techniques by six orders of magnitude [52]. Furthermore, the technique is sensitive to the extremely localized fields of the plasmonic nanoantennas and allows to track the plasmon dynamics *in-situ*. In the development of integrated optical frequency electronics, this techniques will therefore allow to provide a local probe to the high frequency fields, constituting essentially an attosecond sample-and-hold circuit. In addition to the implications for optical frequency electronics, this technique also has great application in optical time domain spectroscopy, which was shown to provide improved sensitivity compared to conventional approaches [48], and moreover, to provide phase-matching-free detection across the full infrared spectral range.

In Chapter 4 the sampling response of the nanoantenna-based technique was investigated theoretically and found to be highly dependent on the geometric properties of the device. By changing the geometry the frequency response can be changed to even, odd, and all harmonics of the driving laser, allowing for application specific selectivity. Adding to the flexibility of the platform, voltage-scale biases could be applied to modify the frequency response, without changing the physical device.

As nanoantenna-based devices only produced on average less than one electron per shot [8, 9, 23], arrays with up to a thousand nanoantennas were designed to proportionally increase charge yield. Additionally, it was found that more than an order of magnitude increase can be expected from sub-2-cycle pulses in the mid-infrared.

To that end, Chapter 5 presents the design and construction of a custom laser source that generates passively phase-stable sub-2-cycle pulses in the mid-infrared via adabatic difference frequency generation. The produced pulses are 16 fs in duration at a center wavelength of 2.7 µm and with a pulse energy of >84 nJ at a repetition rate of 50 kHz. The constructed source, re-

duces significantly the complexity of previous implementations by relying solely on material based compression. The spectral phase of the generated pulses was characterized with a novel implementation of two-dimensional spectral shearing interferometry for the mid-infrared. For the first time, the CEP stability of adiabatic difference frequency generation was characterized with f-2f interferometry and showed exceptional stability with < 190 mrad rms.

Enabled by the custom laser source, Chapter 6 presents single-shot detection of CEP dependent sub-cycle currents in nanoantenna networks was demonstrated. The measured currents reached up to $\sim$3000 electrons per shot, emitted by 1000 antennas, occupying only an area of 15 µm by 15 µm. This not only demonstrates an improvement of 30-fold for the electron emission of a single bow-tie antenna [8, 10, 23], but also improves the total extracted charge per shot from an array by three orders of magnitude compared to previous results [23].With these key achievements, many interesting applications and science experiments become feasible.

The demonstration of electron emission from thousands of antennas not only allows the accumulation of large signals but also gives for the first time statistically significant data on the nanoantennas and their performance. Previously, only up to 10 antennas were used, sensitive to local imperfections in the fabrication process, which hindered precise statements on the general performance of the specific antenna design. By averaging over a thousand individual antennas, studies that require precise knowledge on the shape of the antenna are accessible. For example, the study of quiver-motion of electrons in the local electric near field of the antenna, allowing one to gauge the tunneling process of the electron from the metal surface into the vacuum under precise assumptions of the spatial field distribution [6, 10]. In addition, the tunneling rates in the low field limit, scaling from pure tunneling to multiphoton with Keldysh parameters much larger than 1, are accessible due to the improved signal levels and allow testing of the theoretical models predicted by Yudin and Ivanov [69].

To increase the noise performance of such measurements, the laser system can also be improved by implementing electro-optical control on the CEP of the 2-cycle pulse. Using an electro-optical phase modulator, one can achieve CEP modulation frequencies up to half the repetition rate, moving the CEP-dependent antenna signal to higher frequencies, ultimately enabling shot-noise limited detection. Building on the improved detection sensitivity of large-area nanoantenna devices, on-chip field sampling should be revisited to demonstrate broadband detection in the mid-infrared, covering octaves of spectrum ranging from the terahertz to the near-infrared. For that purpose, the generation and sampling of high-harmonics generated in solids will not only demonstrate the accessible bandwidth, but will also give rise to new insights into the underlying dynamics [49, 50]. With bandwidths exceeding one petahertz for field-sampling devices driven by near-infrared lasers, new materials will need to be investigated, as gold becomes highly lossy for frequencies in the visible [46]. Specifically, achieving sensitive field sampling in the visible will be highly attractive for many electronic processes [141]. The investigation of new materials such as silver, platinum, and aluminum with a broadband response will allow

the scaling to ever higher frequencies. Furthermore, the CMOS compatibility of aluminum provides the benefit that device manufacturing can be implemented with EUV photolithography foundries making these devices accessible for mass manufacturing [142].

Without a doubt, the results of this thesis will enable many interesting experiments, but there are still a few key steps for the development of true optical frequency electronics that need to be addressed in the future. Tracing the historical development of electronics as laid out in the Introduction, a way to measure electronic signals at unprecedented speeds and also a working optical rectifier are demonstrated. However, to achieve true universal optical frequency electronics, the transistor needs to be demonstrated. Optical electronic transistors will be able to amplify signals, make functioning oscillators, and realize Turing-complete logic circuits. Speculating on a possible pathway, the approach of planar structures presented in this thesis might become limiting and will require new fabrication processes that allow one to make complex 3D circuit systems. However, despite the uncertain road ahead, the goal is clear, and the next generation of optical frequency electronics might usher in exciting new technological progress.

8 List of Publications

First author

Bionta*, M. R., Ritzkowsky*, F., Turchetti*, M., Yang, Y., Cattozzo Mor, D., Putnam, W. P., Kärtner, F. X., Berggren, K. K. & Keathley, P. D. On-chip sampling of optical fields with attosecond resolution. *Nature Photonics* **15**, 456–460 (June 2021)
*These authors contributed equally.

Ritzkowsky, F., Bebeti, E., Rossi, G. M., Mainz, R. E., Suchowski, H., Cankaya, H. & Kaertner, F. Passively CEP stable sub-2-cycle source in the mid-infrared by adiabatic difference frequency generation. EN. *Optics Letters* (Feb. 2023)

Ritzkowsky*, F., Yeung*, M., Bebeti, E., Gebert, T., Matsuyama, T., Mainz, R. E., Cankaya, H., Berggren, K. K., Rossi, G. M., Keathley, P. D. & Kärtner, F. X. Large Scale Optical Frequency Electronics. - currently in submission process - (2023)
*These authors contributed equally.

Co-Author

Liehl, A., Sulzer, P., Fehrenbacher, D., Eggert, S., Ludwig, M., Ritzkowsky, F., Seletskiy, D. V. & Leitenstorfer, A. Broadband analysis and self-control of spectral fluctuations in a passively phase-stable Er-doped fiber frequency comb. *Physical Review A* **101,** 023801 (Feb. 2020)

Ludwig, M., Aguirregabiria, G., Ritzkowsky, F., Rybka, T., Marinica, D. C., Aizpurua, J., Borisov, A. G., Leitenstorfer, A. & Brida, D. Sub-femtosecond electron transport in a nanoscale gap. en. *Nature Physics* **16,** 341–345 (Mar. 2020)

Zhang, D., Kroh, T., Ritzkowsky, F., Rohwer, T., Fakhari, M., Cankaya, H., Calendron, A.-L., Matlis, N. H. & Kärtner, F. X. THz-Enhanced DC Ultrafast Electron Diffractometer. *Ultrafast Science* **2021** (Aug. 2021)

Turchetti, M., Bionta, M. R., Yang, Y., Ritzkowsky, F., Candido, D. R., Flatté, M., Berggren, K. K. & Keathley, P. D. Impact of DC bias on Weak Optical-Field-Driven Electron Emission in Nano-Vacuum-Gap Detectors. *J. Opt. Soc. Am. B* **38,** 1009 (2021)

Mor, D. C., Yang, Y., Ritzkowsky, F., Kärtner, F. X., Berggren, K. K., Singh, N. K. & Keathley, P. D. PHz Electronic Device Design and Simulation for Waveguide-Integrated Carrier-Envelope Phase Detection. *Journal of Lightwave Technology* **40,** 3823–3831 (June 2022)

List of Figures

List of Tables

Bibliography

1. Corkum, P. B., Burnett, N. H. & Ivanov, M. Y. Subfemtosecond pulses. EN. *Optics Letters* **19,** 1870–1872 (Nov. 1994).
2. Hentschel, M. *et al.* Attosecond metrology. en. *Nature* **414,** 509–513 (Nov. 2001).
3. Sansone, G. *et al.* Isolated Single-Cycle Attosecond Pulses. *Science* **314,** 443–446 (Oct. 2006).
4. Krausz, F. & Stockman, M. I. Attosecond metrology: from electron capture to future signal processing. en. *Nature Photonics* **8,** 205–213 (Mar. 2014).
5. Urteaga, M., Griffith, Z., Seo, M., Hacker, J. & Rodwell, M. J. W. InP HBT Technologies for THz Integrated Circuits. *Proceedings of the IEEE* **105,** 1051–1067 (June 2017).
6. Herink, G., Solli, D. R., Gulde, M. & Ropers, C. Field-driven photoemission from nanostructures quenches the quiver motion. en. *Nature* **483,** 190–193 (Mar. 2012).
7. Krüger, M., Schenk, M. & Hommelhoff, P. Attosecond control of electrons emitted from a nanoscale metal tip. en. *Nature* **475,** 78–81 (July 2011).
8. Rybka, T. *et al.* Sub-cycle optical phase control of nanotunnelling in the single-electron regime. *Nature Photonics* **10,** 667–670 (Oct. 2016).
9. Putnam, W. P., Hobbs, R. G., Keathley, P. D., Berggren, K. K. & Kärtner, F. X. Optical-field-controlled photoemission from plasmonic nanoparticles. en. *Nature Physics* **13,** 335–339 (Apr. 2017).
10. Ludwig, M. *et al.* Sub-femtosecond electron transport in a nanoscale gap. en. *Nature Physics* **16,** 341–345 (Mar. 2020).
11. Kim, H. Y. *et al.* Attosecond field emission. en. *Nature* **613,** 662–666 (Jan. 2023).
12. Schultze, M. *et al.* Controlling dielectrics with the electric field of light. en. *Nature* **493,** 75–78 (Jan. 2013).
13. Schiffrin, A. *et al.* Optical-field-induced current in dielectrics. en. *Nature* **493,** 70–74 (Jan. 2013).
14. Paasch-Colberg, T. *et al.* Solid-state light-phase detector. en. *Nature Photonics* **8,** 214–218 (Mar. 2014).
15. Sederberg, S. *et al.* Attosecond optoelectronic field measurement in solids. *Nat. Commun.* **11,** 430 (Dec. 2020).

16. Park, S. B. *et al.* Direct sampling of a light wave in air. EN. *Optica* **5,** 402–408 (Apr. 2018).
17. Cho, W. *et al.* Temporal characterization of femtosecond laser pulses using tunneling ionization in the UV, visible, and mid-IR ranges. en. *Scientific Reports* **9,** 1–11 (Nov. 2019).
18. Kubullek, M. *et al.* Single-shot carrier–envelope-phase measurement in ambient air. EN. *Optica* **7,** 35–39 (Jan. 2020).
19. Zimin, D. *et al.* Petahertz-scale nonlinear photoconductive sampling in air. EN. *Optica* **8,** 586–590 (May 2021).
20. Bionta, M. R. *et al.* On-chip sampling of optical fields with attosecond resolution. *Nature Photonics* **15,** 456–460 (June 2021).
21. Ritzkowsky, F. *et al. Tailoring the Impulse Response of Petahertz Optical Field-Sampling Devices* EN. in *The International Conference on Ultrafast Phenomena (UP) 2022 (2022), paper Th1A.4* (Optica Publishing Group, July 2022), Th1A.4.
22. Suchowski, H., Porat, G. & Arie, A. Adiabatic processes in frequency conversion. *Laser & Photonics Reviews* **8,** 333–367 (2014).
23. Yang, Y. *et al.* Light phase detection with on-chip petahertz electronic networks. *Nature Communications* **11,** 3407 (July 2020).
24. Boolakee, T. *et al.* Light-field control of real and virtual charge carriers. en. *Nature* **605,** 251–255 (May 2022).
25. Lee, J. D., Kim, Y. & Kim, C.-M. Model for petahertz optical memory based on a manipulation of the optical-field-induced current in dielectrics. en. *New Journal of Physics* **20,** 093029 (Sept. 2018).
26. Schwierz, F. & Liou, J. J. *Modern microwave transistors: theory, design, and performance* (Wiley-Interscience, New York, 2003).
27. Schwierz, F., Wong, H. & Liou, J. J. *Nanometer CMOS* eng (Pan Stanford publishing, Singapore, 2010).
28. *1874: Semiconductor Point-Contact Rectifier Effect is Discovered — The Silicon Engine — Computer History Museum*
29. Braun, F. Ueber die Stromleitung durch Schwefelmetalle. en. *Annalen der Physik* **229,** 556–563 (1875).
30. Preece, W. H. II. On a peculiar behaviour of glow-lamps when raised to high incandescence. *Proceedings of the Royal Society of London* **38,** 219–230 (1885).
31. Fleming, J. A. On the conversion of electric oscillations into continuous currents by means of a vacuum valve. *Proceedings of the Royal Society of London* **74,** 476–487 (1905).
32. *IEEE Milestones:Fleming Valve, 1904* en. Dec. 2015.
33. Shockley, W. The Theory of p-n Junctions in Semiconductors and p-n Junction Transistors. en. *Bell System Technical Journal* **28,** 435–489 (1949).

34. Van Roosbroeck, W. Theory of the Flow of Electrons and Holes in Germanium and Other Semiconductors. en. *Bell System Technical Journal* **29,** 560–607 (1950).
35. Kularatna, N. *Digital and Analogue Instrumentation: Testing and Measurement* en (IET, 2003).
36. Maiman, T. H. Stimulated Optical Radiation in Ruby. en. *Nature* **187,** 493–494 (Aug. 1960).
37. Franken, P. A., Hill, A. E., Peters, C. W. & Weinreich, G. Generation of Optical Harmonics. *Physical Review Letters* **7,** 118–119 (Aug. 1961).
38. Bose, J. C. US755840A (1904).
39. Hocker, L. O., Javan, A., Rao, D. R., Frenkel, L. & Sullivan, T. Absolute frequency measurement and spectroscopy of gas laser transitions in the far infrared. *Applied Physics Letters* **10,** 147–149 (Mar. 1967).
40. Evenson, K. M., Day, G. W., Wells, J. S. & Mullen, L. O. Extension of Absolute Frequency Measurements to the CW He-Ne Laser at 88 THz (3.39 m). en. *NIST* **20,** 133–134 (Feb. 1971).
41. Chebotayev, V. P. OPTICAL TIME SCALE. en. *Le Journal de Physique Colloques* **42,** C8–512 (Dec. 1981).
42. Weiss, C., Kramer, G., Lipphardt, B. & Garcia, E. Frequency measurement of a CH/sub 4/ hyperfine line at 88 THz/'optical clock'. *IEEE Journal of Quantum Electronics* **24,** 1970–1972 (Oct. 1988).
43. Schnatz, H., Lipphardt, B., Helmcke, J., Riehle, F. & Zinner, G. First Phase-Coherent Frequency Measurement of Visible Radiation. *Physical Review Letters* **76,** 18–21 (Jan. 1996).
44. Jones, D. J. *et al.* Carrier-Envelope Phase Control of Femtosecond Mode-Locked Lasers and Direct Optical Frequency Synthesis. *Science* **288,** 635–639 (Apr. 2000).
45. Diddams, S. A. *et al.* Direct Link between Microwave and Optical Frequencies with a 300 THz Femtosecond Laser Comb. *Physical Review Letters* **84,** 5102–5105 (May 2000).
46. Hanke, T. *et al.* Efficient Nonlinear Light Emission of Single Gold Optical Antennas Driven by Few-Cycle Near-Infrared Pulses. *Phys. Rev. Lett.* **103,** 257404 (Dec. 2009).
47. Stockman, M. I. Nanoplasmonics: past, present, and glimpse into future. EN. *Optics Express* **19,** 22029–22106 (Oct. 2011).
48. Pupeza, I. *et al.* Field-resolved infrared spectroscopy of biological systems. *Nature* **577,** 52–59 (Jan. 2020).
49. Hohenleutner, M. *et al.* Real-time observation of interfering crystal electrons in high-harmonic generation. *Nature* **523,** 572–575 (2015).
50. Keathley, P. D., Jensen, S. V. B., Yeung, M., Bionta, M. R. & Madsen, L. B. Uncovering extreme nonlinear dynamics in solids through time-domain field analysis. *Physical Review B* **107,** 054302 (Feb. 2023).

51. Wittmann, T. *et al.* Single-shot carrier–envelope phase measurement of few-cycle laser pulses. en. *Nature Physics* **5,** 357–362 (May 2009).
52. Keiber, S. *et al.* Electro-optic sampling of near-infrared waveforms. en. *Nature Photonics* **10,** 159–162 (Mar. 2016).
53. Krogen, P. *et al.* Generation and multi-octave shaping of mid-infrared intense single-cycle pulses. *Nature Photonics* **11,** 222–226 (Apr. 2017).
54. Ritzkowsky, F. *et al.* Passively CEP stable sub-2-cycle source in the mid-infrared by adiabatic difference frequency generation. EN. *Optics Letters* (Feb. 2023).
55. Cavalleri, A. *et al.* Femtosecond Structural Dynamics in ${\mathrm{VO}}_{2}$ during an Ultrafast Solid-Solid Phase Transition. *Physical Review Letters* **87,** 237401 (Nov. 2001).
56. Keller, U. *Ultrafast Lasers: A Comprehensive Introduction to Fundamental Principles with Practical Applications* en (Springer International Publishing, Cham, 2021).
57. Boyd, R. W. *Nonlinear optics* Third edition. eng (Elsevier, Academic Press, Amsterdam Heidelberg, 2008).
58. Riek, C. *et al.* Direct sampling of electric-field vacuum fluctuations. en. *Science* **350,** 420–423 (Oct. 2015).
59. Manzoni, C. & Cerullo, G. Design criteria for ultrafast optical parametric amplifiers. *Journal of Optics* **18,** 103501 (Aug. 2016).
60. Lenard, P. Ueber die lichtelektrische Wirkung. en. *Annalen der Physik* **313,** 149–198 (1902).
61. Einstein, A. Über einen die Erzeugung und Verwandlung des Lichtes betreffenden heuristischen Gesichtspunkt. en. *Annalen der Physik* **322,** 132–148 (1905).
62. Rohwer, T. *et al.* Collapse of long-range charge order tracked by time-resolved photoemission at high momenta. en. *Nature* **471,** 490–493 (Mar. 2011).
63. Fowler, R. H. & Nordheim, L. Electron Emission in Intense Electric Fields. *Royal Society of London Proceedings Series A* **119,** 173–181 (May 1928).
64. Krüger, M. *Attosecond physics in strong-field photoemission from metal nanotips* de. Text.PhDThesis (Ludwig-Maximilians-Universität München, Oct. 2013).
65. Yalunin, S. V., Gulde, M. & Ropers, C. Strong-field photoemission from surfaces: Theoretical approaches. *Physical Review B* **84,** 195426 (Nov. 2011).
66. Keldysh, L. V. Ionization in the Field of a Strong Electromagnetic Wave. *Sov. Phys. JETP* **20,** 1307–1314 (1965).
67. Bunkin, F. V. & Fedorov, M. V. Cold Emission of Electrons from Surface of a Metal in a Strong Radiation Field. *Soviet Physics JETP* **21,** 896–899 (1965).
68. Keathley, P. D. *et al.* Vanishing carrier-envelope-phase-sensitive response in optical-field photoemission from plasmonic nanoantennas. en. *Nature Physics,* 1–6 (Aug. 2019).
69. Yudin, G. L. & Ivanov, M. Y. Nonadiabatic tunnel ionization: Looking inside a laser cycle. *Physical Review A* **64,** 013409 (June 2001).

70. Tonouchi, M. Cutting-edge terahertz technology. *Nat. Photon.,* 97 (2007).
71. Neu, J. & Schmuttenmaer, C. A. Tutorial: An introduction to terahertz time domain spectroscopy (THz-TDS). *Journal of Applied Physics* **124,** 231101 (Dec. 2018).
72. Bonvalet, A. *et al.* Femtosecond Infrared Emission Resulting from Coherent Charge Oscillations in Quantum Wells. *Physical Review Letters* **76,** 4392–4395 (June 1996).
73. Schubert, O. *et al.* Sub-cycle control of terahertz high-harmonic generation by dynamical Bloch oscillations. en. *Nature Photonics* **8,** 119–123 (Feb. 2014).
74. Lépine, F., Ivanov, M. Y. & Vrakking, M. J. J. Attosecond molecular dynamics: fact or fiction? *Nat. Photon.* **8,** 195–204 (Mar. 2014).
75. Itatani, J. *et al.* Attosecond Streak Camera. *Phys. Rev. Lett.* **88,** 173903 (Apr. 2002).
76. Kienberger, R. *et al.* Atomic transient recorder. *Nature* **427,** 817–821 (Feb. 2004).
77. Dombi, P. *et al.* Strong-field nano-optics. en. *Reviews of Modern Physics* **92,** 025003 (June 2020).
78. Krüger, M., Lemell, C., Wachter, G., Burgdörfer, J. & Hommelhoff, P. Attosecond physics phenomena at nanometric tips. en. *Journal of Physics B: Atomic, Molecular and Optical Physics* **51,** 172001 (Aug. 2018).
79. Schoetz, J. *et al.* Perspective on Petahertz Electronics and Attosecond Nanoscopy. *ACS Photonics* **6,** 3057–3069 (Dec. 2019).
80. Ciappina, M. F. *et al.* Attosecond physics at the nanoscale. en. *Reports on Progress in Physics* **80,** 054401 (2017).
81. Stockman, M. I. *et al.* Roadmap on plasmonics. *J. Opt.* **20,** 043001 (Apr. 2018).
82. Gomer, R. *Field emission and field ionization* (Harvard University Press Cambridge, MA, 1961).
83. Keathley, P. *et al. Carrier-Envelope Phase Detection with Arrays of Electrically Connected Bowtie Nanoantennas* in (OSA, San Jose, CA, USA, 2019).
84. Anderson, A., Deryckx, K. S., Xu, X. G., Steinmeyer, G. & Raschke, M. B. Few-Femtosecond Plasmon Dephasing of a Single Metallic Nanostructure from Optical Response Function Reconstruction by Interferometric Frequency Resolved Optical Gating. *Nano Letters* **10,** 2519–2524 (July 2010).
85. Picqué, N. & Hänsch, T. W. Frequency comb spectroscopy. en. *Nature Photonics* **13,** 146–157 (Mar. 2019).
86. Coddington, I., Swann, W. C. & Newbury, N. R. Coherent Multiheterodyne Spectroscopy Using Stabilized Optical Frequency Combs. *Physical Review Letters* **100,** 013902 (Jan. 2008).
87. Bjork, B. J. *et al.* Direct frequency comb measurement of OD + CO $\rightarrow$ DOCO kinetics. *Science* **354,** 444–448 (Oct. 2016).
88. Kowligy, A. S. *et al.* Infrared electric-field sampled frequency comb spectroscopy. *arXiv:1808.10275 [physics]* (Aug. 2018).

89. Sell, A., Krauss, G., Scheu, R., Huber, R. & Leitenstorfer, A. 8-fs pulses from a compact Er:fiber system: quantitative modeling and experimental implementation. *Opt. Express* **17,** 1070–1077 (Jan. 2009).
90. Putnam, W. P. *et al.* Few-cycle, carrier–envelope-phase-stable laser pulses from a compact supercontinuum source. *J. Opt. Soc. Am. B* **36,** A93 (2019).
91. Birge, J. R., Ell, R. & Kärtner, F. X. Two-dimensional spectral shearing interferometry for few-cycle pulse characterization. EN. *Optics Letters* **31,** 2063–2065 (July 2006).
92. Turchetti, M. *et al.* Impact of DC bias on Weak Optical-Field-Driven Electron Emission in Nano-Vacuum-Gap Detectors. *J. Opt. Soc. Am. B* **38,** 1009 (2021).
93. Johnson, P. B. & Christy, R. W. Optical Constants of the Noble Metals. *Phys. Rev. B* **6,** 4370–4379 (Dec. 1972).
94. Cho, W., Shin, J.-u. & Kim, K. T. Reconstruction algorithm for tunneling ionization with a perturbation for the time-domain observation of an electric-field. en. *Scientific Reports* **11,** 13014 (June 2021).
95. Hobbs, R. G. *et al.* Mapping Photoemission and Hot-Electron Emission from Plasmonic Nanoantennas. *Nano Letters* **17,** 6069–6076 (Oct. 2017).
96. Sell, A., Scheu, R., Leitenstorfer, A. & Huber, R. Field-resolved detection of phase-locked infrared transients from a compact Er:fiber system tunable between 55 and 107 THz. *Applied Physics Letters* **93,** 251107 (Dec. 2008).
97. Sulzer, P. *et al.* Determination of the electric field and its Hilbert transform in femtosecond electro-optic sampling. *Physical Review A* **101,** 033821 (Mar. 2020).
98. Leitenstorfer, A., Hunsche, S., Shah, J., Nuss, M. C. & Knox, W. H. Detectors and sources for ultrabroadband electro-optic sampling: Experiment and theory. *Applied Physics Letters* **74,** 1516–1518 (Mar. 1999).
99. McIver, J. W. *et al.* Light-induced anomalous Hall effect in graphene. en. *Nature Physics* **16,** 38–41 (Jan. 2020).
100. Karnetzky, C. *et al.* Towards femtosecond on-chip electronics based on plasmonic hot electron nano-emitters. en. *Nature Communications* **9,** 2471 (June 2018).
101. Ludwig, M. *et al.* Active control of ultrafast electron dynamics in plasmonic gaps using an applied bias. *Physical Review B* **101,** 241412 (June 2020).
102. Rossi, G. M. *et al.* CEP dependence of signal and idler upon pump-seed synchronization in optical parametric amplifiers. en. *Optics Letters* **43,** 178 (Jan. 2018).
103. Telle, H. *et al.* Carrier-envelope offset phase control: A novel concept for absolute optical frequency measurement and ultrashort pulse generation. *Applied Physics B* **69,** 327–332 (Oct. 1999).
104. Baltuška, A. *et al.* Attosecond control of electronic processes by intense light fields. en. *Nature* **421,** 611–615 (Feb. 2003).
105. Rossi, G. M. *et al.* Sub-cycle millijoule-level parametric waveform synthesizer for attosecond science. *Nature Photonics* **14,** 629–635 (Oct. 2020).

106. Chen, M.-C. *et al.* Generation of bright isolated attosecond soft X-ray pulses driven by multicycle midinfrared lasers. *Proceedings of the National Academy of Sciences of the United States of America* **111,** E2361–2367 (June 2014).
107. Tian, K., He, L., Yang, X. & Liang, H. Mid-Infrared Few-Cycle Pulse Generation and Amplification. *Photonics* **8,** 290 (Aug. 2021).
108. Gayer, O., Sacks, Z., Galun, E. & Arie, A. Temperature and wavelength dependent refractive index equations for MgO-doped congruent and stoichiometric LiNbO3. *Applied Physics B* **91,** 343–348 (May 2008).
109. Grigutis, R., Tamošauskas, G., Jukna, V., Risos, A. & Dubietis, A. Supercontinuum generation and optical damage of sapphire and YAG at high repetition rates. EN. *Optics Letters* **45,** 4507–4510 (Aug. 2020).
110. Birge, J. R., Crespo, H. M. & Kärtner, F. X. Theory and design of two-dimensional spectral shearing interferometry for few-cycle pulse measurement. *JOSA B* **27,** 1165–1173 (June 2010).
111. Gordon, I. E. *et al.* The HITRAN2020 molecular spectroscopic database. *Journal of Quantitative Spectroscopy and Radiative Transfer* **277,** 107949 (Jan. 2022).
112. Lee, H., Oh, C. & Hahn, J. W. Calibration of a mid-IR optical emission spectrometer with a 256-array PbSe detector and an absolute spectral analysis of IR signatures. en. *Infrared Physics & Technology* **57,** 50–55 (Mar. 2013).
113. Holzwarth, R. *et al.* Optical Frequency Synthesizer for Precision Spectroscopy. *Physical Review Letters* **85,** 2264–2267 (Sept. 2000).
114. Dubietis, A., Tamošauskas, G., Šuminas, R., Jukna, V. & Couairon, A. Ultrafast supercontinuum generation in bulk condensed media. en. *Lithuanian Journal of Physics* **57** (Oct. 2017).
115. Rossi, G. M. *Parametric Waveform Synthesis: Parametric Wellenformsynthese* PhD Thesis (Deutsches Elektronen Synchroton DESY, 2019).
116. Baltuska, A. *et al.* Phase-controlled amplification of few-cycle laser pulses. *IEEE Journal of Selected Topics in Quantum Electronics* **9,** 972–989 (July 2003).
117. Trebino, R. *et al.* Measuring ultrashort laser pulses in the time-frequency domain using frequency-resolved optical gating. *Review of Scientific Instruments* **68,** 3277–3295 (Sept. 1997).
118. Sidorenko, P., Lahav, O., Avnat, Z. & Cohen, O. Ptychographic reconstruction algorithm for frequency-resolved optical gating: super-resolution and supreme robustness. EN. *Optica* **3,** 1320–1330 (Dec. 2016).
119. Linden, S., Kuhl, J. & Giessen, H. en. in *Frequency-Resolved Optical Gating: The Measurement of Ultrashort Laser Pulses* (ed Trebino, R.) 313–322 (Springer US, Boston, MA, 2000).
120. Coddington, I., Swann, W. C. & Newbury, N. R. Time-domain spectroscopy of molecular free-induction decay in the infrared. EN. *Optics Letters* **35,** 1395–1397 (May 2010).

121. Birge, J. R. *Methods for Engineering Sub-Two-Cycle Mode-Locked Lasers* en. PhD thesis (Massachusetts Institute of Technology, Cambridge, MA, June 2009).
122. Salzberg, C. D. & Villa, J. J. Infrared Refractive Indexes of Silicon Germanium and Modified Selenium Glass*. EN. *JOSA* **47,** 244–246 (Mar. 1957).
123. Margules, P., Moses, J., Suchowski, H. & Porat, G. Ultrafast adiabatic frequency conversion. en. *Journal of Physics: Photonics* **3,** 022011 (Apr. 2021).
124. Storn, R. & Price, K. Differential Evolution – A Simple and Efficient Heuristic for global Optimization over Continuous Spaces. en. *Journal of Global Optimization* **11,** 341–359 (Dec. 1997).
125. *scipy.optimize.differential_evolution — SciPy v1.10.0 Manual*
126. Steinleitner, P. *et al.* Single-cycle infrared waveform control. en. *Nature Photonics* **16,** 512–518 (July 2022).
127. Small, J. G. *et al.* ac electron tunneling at infrared frequencies: Thin-film M-O-M diode structure with broad-band characteristics. *Applied Physics Letters* **24,** 275–279 (Mar. 1974).
128. Sola, I. J. *et al.* Controlling attosecond electron dynamics by phase-stabilized polarization gating. en. *Nature Physics* **2,** 319–322 (May 2006).
129. Sederberg, S. *et al.* Vectorized optoelectronic control and metrology in a semiconductor. en. *Nature Photonics* **14,** 680–685 (Nov. 2020).
130. Higuchi, T., Heide, C., Ullmann, K., Weber, H. B. & Hommelhoff, P. Light-field-driven currents in graphene. en. *Nature* **550,** 224–228 (Oct. 2017).
131. Hui, D. *et al.* Attosecond electron motion control in dielectric. en. *Nature Photonics* **16,** 33–37 (Jan. 2022).
132. Buckley, D., Yang, Y., Yang-Keathley, Y., Berggren, K. K. & Keathley, P. D. Nanoantenna design for enhanced carrier–envelope-phase sensitivity. EN. *JOSA B* **38,** C11–C21 (Sept. 2021).
133. Timm, G. W. & Van der Ziel, A. Noise in field emission diodes. *Physica* **32,** 1333–1344 (July 1966).
134. Shi, L. *et al.* Femtosecond Field-Driven On-Chip Unidirectional Electronic Currents in Nonadiabatic Tunneling Regime. en. *Laser & Photonics Reviews* **15,** 2000475 (2021).
135. Hoff, D. *et al.* Continuous every-single-shot carrier-envelope phase measurement and control at 100 kHz. EN. *Optics Letters* **43,** 3850–3853 (Aug. 2018).
136. Schötz, J. *et al.* Onset of charge interaction in strong-field photoemission from nanometric needle tips. en. *Nanophotonics* **10,** 3769–3775 (Oct. 2021).
137. Liu, Y., Beetar, J. E., Nesper, J., Gholam-Mirzaei, S. & Chini, M. Single-shot measurement of few-cycle optical waveforms on a chip. en. *Nature Photonics* **16,** 109–112 (Feb. 2022).
138. Rakić, A. D. Algorithm for the determination of intrinsic optical constants of metal films: application to aluminum. EN. *Applied Optics* **34,** 4755–4767 (Aug. 1995).

139. Oliaei, O. Noise analysis of correlated double sampling SC integrators with a hold capacitor. *IEEE Transactions on Circuits and Systems I: Fundamental Theory and Applications* **50,** 1198–1202 (Sept. 2003).
140. Wey, H. & Guggenbuhl, W. Noise transfer characteristics of a correlated double sampling circuit. *IEEE Transactions on Circuits and Systems* **33,** 1028–1030 (Oct. 1986).
141. Brida, D. *et al.* Ultrafast collinear scattering and carrier multiplication in graphene. en. *Nature Communications* **4,** 1987 (June 2013).
142. Mojarad, N., Gobrecht, J. & Ekinci, Y. Beyond EUV lithography: a comparative study of efficient photoresists' performance. en. *Scientific Reports* **5,** 9235 (Mar. 2015).
143. Liehl, A. *et al.* Broadband analysis and self-control of spectral fluctuations in a passively phase-stable Er-doped fiber frequency comb. *Physical Review A* **101,** 023801 (Feb. 2020).
144. Zhang, D. *et al.* THz-Enhanced DC Ultrafast Electron Diffractometer. *Ultrafast Science* **2021** (Aug. 2021).
145. Mor, D. C. *et al.* PHz Electronic Device Design and Simulation for Waveguide-Integrated Carrier-Envelope Phase Detection. *Journal of Lightwave Technology* **40,** 3823–3831 (June 2022).

Eidesstattliche Versicherung
Declaration on oath

Hiermit erkläre ich an Eides statt, dass ich die vorliegende Dissertationsschrift selbst verfasst und keine anderen als die angegebenen Quellen und Hilfsmittel benutzt habe.
I hereby declare, on oath, that I have written the present dissertation by my own and have not used other than the acknowledged resources and aids.

Hamburg, den 3.4.2023 **Unterschrift**